

UNIVERSITE LOUIS PASTEUR - STRASBOURG, France
École Nationale Supérieure de Physique de Strasbourg
LSIIT, UPRES-A 7005

TECHNISCHE UNIVERSITÄT BERLIN, Deutschland
Fachbereich Verkehrswesen und Angewandte Mechanik
Institut für Luft- und Raumfahrt

DISSERTATION

zur Erlangung des akademischen Grades
doctor rerum naturalium (Dr. rer. nat.)

THESE

pour obtenir le grade de
docteur de l'Université de Strasbourg I
Spécialité: Télédétection

Temperature Retrieval Approaches for Upcoming BIRD Data

von

présentée par

Dipl.-Met. Kerstin Lippert

eingereicht im Juni 2000

wissenschaftliche Aussprache am 27. Oktober 2000

soutenue le 27 octobre 2000

Promotionsausschuß

Vorsitzender	Prof. Dr. Wolfgang Nitsche
Berichter	Prof. Dr. François Becker Prof. Dr. Herbert Jahn Prof. Dr. Hans Peter Röser Prof. Dr. Marc-Philippe Stoll

Jury

Président
Rapporteur interne
Rapporteur externe
Directeur de thèse (TUB)
Directeur de thèse (ULP)

D 83
Berlin 2001

N° d'ordre:

Abstract

The Earth's surface temperature is a key parameter for understanding of the energetic and hydrological balance of the Earth. Continuous accurate measurements of the regional and global temperature distribution can provide information on its changes and impact on the global climate. Since the late 1960s, satellite measurements have been utilized for Earth's monitoring. Surface temperature space-borne measurements have been used in a variety of applications, such as energy transfer, weather forecasting, mesoscale modeling, agriculture, and forest fire mapping.

At the Institute of Space Sensor Technology and Planetary Exploration at the German Aerospace Center (DLR), a small satellite BIRD (Bi-spectral InfraRed Detection) has been developed. It is slated to be launched in 2001. The BIRD mission shall demonstrate the technological and scientific feasibility of a remote sensing small satellite mission under tight budget constraints. The main scientific objectives of the BIRD mission are the investigation of high-temperature-events (HTE) like fires, volcanos etc. and vegetation exploration. Since BIRD does not have any thermal channels in the 10 and 12 μm atmospheric window, it was necessary to develop temperature retrieval methods for land surfaces which utilized the BIRD channels at 3.4 – 4.2 μm and 8.5 – 9.3 μm .

Two land surface temperature retrieval approaches are presented in this document. One method is based on a linear regression method utilizing the top-of-atmosphere brightness temperatures of both infrared BIRD channels. Since land surfaces are characterized by the emissivity, an emissivity correction was employed. The second approach separates the temperature and emissivity using ground radiances from BIRD's MIR and TIR channels. The at-ground TIR brightness temperature is utilized for the estimation of the thermal contribution to the MIR ground radiance. Thus, an emissivity correction factor called TISIE was introduced to account for the emissivity differences between both IR channels. For the investigation of the approaches, large synthetic data sets consisting of coupled surface and atmospheric models were produced using the radiative transfer model MODTRAN.

The results are to be considered as a first case study of utilizing BIRD's MIR and TIR channel to examine vegetation surfaces. Root mean square temperature retrieval errors for the "TISIE" - Approach and the "Regression" - Approach under nighttime conditions lie around 1 K and within a range of 0.5 to 2.5 K, respectively. The application of the "Regression" - Approach during daytime is not recommended. The advantage of applying the "TISIE"-Approach is that no a priori emissivity information is necessary although an atmospheric correction has to be applied first. A discussion of error sources is given and leads to generally unsatisfying temperature retrieval errors for vegetation applications. The error magnitudes result from a trade-off between the main and secondary objectives of the BIRD mission, which are the HTE detection and vegetation monitoring, respectively. The algorithms might be applicable within the frame of these objectives for particular vegetation studies. Finally, both algorithms still have to be validated on real atmospheric and BIRD data. Further investigations on the presented subject are in progress.

Zusammenfassung

Die Untersuchung der Erdoberflächentemperatur ist eine wesentliche Voraussetzung für das Verständnis des energetischen und hydrologischen Gleichgewichts der Erde. Die Beobachtung der regionalen und globalen Temperaturverteilung sowie die Analyse der Wechselwirkung zwischen Erdoberflächentemperatur und globalem Klima erfordern kontinuierliche, zuverlässige Messungen der Temperatur der Erdoberfläche. Seit den späten 60er Jahren sind satellitengestützte Temperaturmessungen fester Bestandteil der Beobachtung der Erdoberflächentemperatur. Diese werden für eine Vielzahl von Anwendungen eingesetzt. Stellvertretend sei auf die Untersuchung des Energietransfers, die Wettervorhersage, die Entwicklung von mesoskaligen Modellen sowie die Anwendungen in Landwirtschaft und Waldbranddetektion verwiesen.

Am Institut für Weltraumsensorik und Planetenerkundung des Deutschen Zentrums für Luft- und Raumfahrt (DLR) wird derzeit ein Kleinsatellit namens BIRD (Bispectral InfraRed Detection) entwickelt, dessen Start für das Jahr 2001 geplant ist. Die BIRD Mission soll die technologischen und wissenschaftlichen Möglichkeiten einer Fernerkundungs-Kleinsatellitenmission unter engen finanziellen Rahmenbedingungen ausloten. Die wesentlichen wissenschaftlichen Zielstellungen der BIRD Mission bestehen in der Untersuchung von Hochtemperaturereignissen (HTE), beispielsweise von Feuern oder Vulkanen, sowie von Vegetation. Da BIRD nicht über einen thermalen Kanal innerhalb des atmosphärischen Fensters zwischen 10 und 12 μm verfügt, ist die Entwicklung von Algorithmen zur Bestimmung von Landoberflächentemperaturen unter Berücksichtigung der Spektralkanäle von BIRD (3.4 – 4.2 μm , 8.5 – 9.3 μm) notwendig.

Zu diesem Zweck wurden zwei Methoden entwickelt. Die erste Variante basiert auf einer linearen Regression unter Verwendung der Helligkeitstemperaturen am Atmosphärenoberrand. Da verschiedene Landoberflächen durch sehr unterschiedliche Emissivitäten gekennzeichnet sein können, wird eine Emissivitätskorrektur durchgeführt. Die zweite Methode separiert Temperatur- und Emissivitätsinformation unter Nutzung der Bodenstrahlung in den MIR und TIR Kanälen von BIRD. Die Bodenstrahlung im TIR Kanal wird zur Bestimmung des thermalen Anteiles an der MIR Bodenstrahlung verwendet. Dazu ist aufgrund der Emissivitätsunterschiede zwischen beiden Kanälen die Einführung eines Emissivitätsfaktors TISIE notwendig. Für die Entwicklung beider Methoden wurden große synthetische Datensätze erzeugt, welche sich aus der Kombination verschiedener Oberflächen- und Atmosphärenmodelle ergeben. Die Berechnung des atmosphärischen Strahlungstransportes erfolgt mit dem Modell MODTRAN.

Diese Arbeit untersucht die Qualität der Temperaturbestimmung von Landoberflächen unter den Rahmenbedingungen der spektralen Konstellation der BIRD-Kanäle. Die mittleren quadratischen Fehler liegen unter Nachtbedingungen bei 1 K bzw. zwischen 0.5 und 2.5 K für die TISIE- bzw. die Regressionsmethode. Die Regressionsmethode erweist sich für Tagbedingungen, d.h. unter Berücksichtigung eines solaren Anteils am Strahlungstransport, als ungeeignet. Der Vorteil der TISIE-Methode besteht in der gleichzeitigen Bestimmung von Emissivität und Temperatur. Die notwendige Atmosphärenkorrektur erfordert jedoch Informationen über die atmosphärischen Bedingungen zum Zeitpunkt der Messung. Die potentiellen Fehlerquellen der Temperaturbestimmung werden diskutiert. Eine Abschätzung ergibt unbefriedigende Fehler für die Bestimmung der Temperatur von Landoberflächen. Die Größenordnung der Fehler resultiert aus dem primären Fokus der BIRD Mission auf HTE-Anwendungen. Für bestimmte Anwendungen im "Normal"-Temperaturbereich sind die Algorithmen jedoch anwendbar. Beide Methoden sind an realistischen BIRD-Daten zu validieren. Weitere Untersuchungen zu den Methoden werden durchgeführt.

Resume

La température de surface est un des paramètres clés de l'interprétation à l'échelle régionale et globale des équilibres énergétique et hydrologique de la Terre. Des mesures précises systématiques des champs de température régionale ou globale renseignent sur leur variabilité et permettent d'en évaluer l'impact sur le climat global. Les mesures de température des surfaces continentales interviennent dans une variété d'applications, comme par exemple la quantification des transferts d'énergie, la prévision du temps et les modèles méso-échelle de circulation atmosphérique, de même qu'en agriculture ainsi que pour la cartographie des feux de forêts.

La mission BIRD (Bi-spectral Infrared Detection), de la catégorie petit satellite, est en cours de réalisation au "Institute of Space Sensor Technology and Planetary Exploration" du "German Aerospace Center (DLR)". Le lancement est prévu pour 2001. BIRD doit faire la démonstration de la faisabilité technologique et scientifique d'une mission de télédétection à petit satellite réalisée sous un petit budget. Les objectifs scientifiques principaux de la mission BIRD portent sur les "événements-haute-température" (HTE), comme les feux, les volcans, les feux de forêts ainsi que le suivi de la végétation. L'objectif prioritaire HTE a conduit à doter BIRD de deux canaux spécifiques MIR: ($3.4 - 4.2 \mu m$), et TIR: ($8.5 - 9.3 \mu m$). Ainsi, BIRD ne disposant d'aucun canal infrarouge dans la fenêtre atmosphérique entre 10 et $12 \mu m$, il a fallu développer des méthodes de restitution des températures des surfaces continentales adaptées à cette configuration inhabituelle.

Deux approches pour la restitution des températures de surfaces continentales sont présentées dans ce document. La première est une méthode de régression linéaire utilisant les températures de brillance mesurées dans les canaux BIRD au niveau du capteur. La prise en compte de l'émissivité, caractéristique de la surface, est effectuée via une correction en deux étapes. La deuxième approche se propose de séparer l'information température et l'information émissivité apportée par les radiances au niveau du sol dans les canaux MIR et TIR de BIRD. Un facteur de correction d'émissivité, noté TISIE, prend en compte le fait que les émissivités ne sont pas les mêmes dans les deux canaux IR. Pour développer ces deux approches, une importante base de données synthétiques couplant surface et modèles atmosphériques a été réalisées avec le code MODTRAN.

Les résultats obtenus doivent être vus comme une première étude pour évaluer la possibilité d'utiliser les canaux MIR et TIR de BIRD pour examiner des surfaces couvertes de végétation. Les erreurs moyennes sur la température restituée soit par la méthode "TISIE", soit par la méthode dite "Régression", pour des observations de nuit, se situent, respectivement, autour de $1 K$, et dans l'intervalle $0.5 - 2.5 K$. L'application de la méthode "Régression" à des données de jour est déconseillée. L'approche TISIE a l'avantage qu'aucune information a priori sur l'émissivité n'est nécessaire; en revanche, elle demande d'appliquer d'abord une correction atmosphérique aux données. Une discussion des sources d'erreurs et une évaluation de l'erreur totale est faite: il apparaît que l'ordre de grandeur de l'erreur commise sur la température ne correspond en général pas à ce qui est nécessaire pour une problématique végétation. Néanmoins, ces erreurs restent acceptables dans le contexte de thématique HTE. Finalement, les deux algorithmes doivent encore être validés sur des données réelles, tant atmosphériques que satellitales. Des investigations complémentaires aux travaux présentés dans ce document sont en cours.

Contents

1	Introduction	1
2	The BIRD Mission	5
2.1	Objectives	5
2.2	Technical Data Overview	6
3	Atmospheric Radiative Transfer	11
3.1	Sensitivity Analysis	17
4	“Regression” - Approach	31
4.1	Simulated BIRD Data Set	31
4.2	Method	34
4.2.1	Bi-spectral Linear Regression	34
4.2.2	Emissivity Correction	38
4.3	Results	41
5	“TISIE” - Approach	47
5.1	Surface and Atmospheric Models	47
5.2	Method Description	49
5.3	TISIE Determination	55
5.3.1	Temperature Independent Spectral Indices	55
5.3.2	Estimation of TISIE Using Linear Regression	57
5.4	Results	66
5.4.1	Method Retrieval Errors	66
5.4.2	Overall Simulation Error	76

6 Outlook on Both Approaches	79
6.1 Final Retrieval Error Estimation	79
6.2 Algorithm for Upcoming BIRD Data	85
7 Conclusions	89
A Further Results of “Regression” - Approach	91
B TISIE Regression Coefficients	99
C Further Results of “TISIE”-Approach	109
References	122
Symbols	129
Abbreviation	133
Curriculum Vitae	135
Acknowledgements	137

List of Tables

2.1	BIRD mission objectives	5
2.2	Technical parameters of the BIRD instruments assuming a payload at 450 km altitude	7
3.1	Nomenclature for standard atmospheres used in the sensitivity analysis	17
3.2	Amount of atmospheric parameters for standard atmospheres	18
3.3	Summary of reference and perturbed models for the sensitivity analysis	19
4.1	Used temperature profiles and water vapor content according to the three standard atmospheres	32
4.2	Included boundary layer aerosol types	32
4.3	Considered cirrus models	32
4.4	Included surface types and its spectral emissivity.	34
4.5	Characterization of the subset number j	36
4.6	Subset intervals according to the water vapor amount W and surface temperature T_S	36
4.7	Mean (rms) temperature retrieval errors for a <i>blackbody</i> data set	37
4.8	Temperature retrieval errors after applying the entire algorithm considering the mid latitude data set and using simulated nighttime data	41
4.9	Included “extreme” atmospheric conditions	43
4.10	Temperature retrieval errors after applying the entire algorithm with or without emissivity correction utilizing <i>water/vegetation</i> or <i>bare soil</i> data sets as well as simulated daytime data	45
5.1	Emissivity database	48
5.2	Method retrieval errors for MIR and TIR emissivity and surface temperature for different solar zenith angles	67

5.3	Same as Table 5.2, but the entire data set is split into four standard atmospheres	69
5.4	Overall simulation errors for MIR and TIR emissivity and surface temperature for a MLS atmosphere	78
6.1	Exemplary values for an error estimation (part1)	81
6.2	Exemplary values for an error estimation (part2)	83
6.3	Uncertainties of a priori information on atmospheric parameters	84
A.1	Temperature retrieval regression coefficients $a_i, i = 0, \dots, 3$ and the regression correlation coefficient R between true and estimated surface temperatures utilizing a <i>blackbody</i> data set $\varepsilon_i = 1.0$ and simulated nighttime data	92
A.2	Same as Table A.1 but using simulated daytime data	92
B.1	Regression coefficients and correlation coefficient R for the relation between $TISIE_a$ and at-ground radiance ratio L_1^{grd}/L_2^{grd} for the mid latitude summer standard atmosphere	100
B.2	Regression coefficients and correlation coefficient R for the relation between $TISIE_a$ and at-ground radiance ratio L_1^{grd}/L_2^{grd} for the tropical standard atmosphere	101
B.3	Regression coefficients and correlation coefficient R for the relation between $TISIE_a$ and at-ground radiance ratio L_1^{grd}/L_2^{grd} for the mid latitude winter standard atmosphere	102
B.4	Regression coefficients and correlation coefficient R for the relation between $TISIE_a$ and at-ground radiance ratio L_1^{grd}/L_2^{grd} for the US-standard atmosphere	103
B.5	Regression coefficients and correlation coefficient R for the relation between $TISIE_b$ and at-ground radiance ratio L_1^{grd}/L_2^{grd} for the mid latitude summer standard atmosphere	104
B.6	Regression coefficients and correlation coefficient R for the relation between $TISIE_b$ and at-ground radiance ratio L_1^{grd}/L_2^{grd} for the tropical standard atmosphere	105
B.7	Regression coefficients and correlation coefficient R for the relation between $TISIE_b$ and at-ground radiance ratio L_1^{grd}/L_2^{grd} for the mid latitude winter standard atmosphere	106
B.8	Regression coefficients and correlation coefficient R for the relation between $TISIE_b$ and at-ground radiance ratio L_1^{grd}/L_2^{grd} for the US-standard atmosphere	107

List of Figures

2.1	Flight configuration of BIRD, (LWIR=TIR, MWIR=MIR)	6
2.2	MIR and TIR images from the airborne experiment in Oberpfaffenhofen on the 10/22/1998, crossing time: 3:30 pm (local time), altitude: 1200 m	7
2.3	Response functions of the BIRD sensors	9
3.1	Transmission τ of atmospheric gases for an US standard atmosphere, rural aerosol, cirrus cloud	11
3.2	Spherical coordinate system defining position of observer relative to the principal plane and indicating the solar hot-spot direction and the backward and forward scattering regions	12
3.3	Simplified description of the atmospheric radiative transfer within the infrared	13
3.4	Spectral blackbody radiance for several temperatures compared to typical reflectance spectra of natural surfaces	16
3.5	Flow chart for the sensitivity analysis procedure; $L_i^{toa,ATM}$: top-of-atmosphere radiance for the standard atmosphere <i>ATM</i>	20
3.6	Ground temperature error as a function of water vapor for different standard atmospheres, TIR	23
3.7	Ground temperature error as a function of water vapor for different standard atmospheres, MIR	24
3.8	Ground temperature error as a function of temperature profile for different standard atmospheres, TIR	25
3.9	Ground temperature error as a function of temperature profile for different standard atmospheres, MIR	26
3.10	Ground temperature error as a function of aerosols for different standard atmospheres, TIR	27
3.11	Ground temperature error as a function of aerosols for different standard atmospheres, MIR	28

3.12	Ground temperature error as a function of aerosol plus volcanic aerosol for different standard atmospheres, TIR	29
3.13	Ground temperature error as a function of aerosol plus volcanic aerosol for different standard atmospheres, MIR	30
4.1	Aerosol amount and visibility	33
4.2	Temperature retrieval errors ($T_S^* - T_S$) versus true surface temperatures (T_S) utilizing the <i>blackbody</i> data set and simulated nighttime data . . .	38
4.3	Temperature retrieval errors ($T_S^* - T_S$) versus true surface temperatures (T_S) after applying the first emissivity correction ($T_S^* = T_S^{**} + dT_S^{**}$) utilizing the <i>water/vegetation</i> data set and simulated nighttime data . .	40
4.4	Temperature retrieval errors ($T_S^* - T_S$) versus true surface temperatures (T_S) after applying the entire algorithm utilizing the <i>water/vegetation</i> data set and simulated nighttime data	42
4.5	Frequency distribution of occurred temperature retrieval errors ($T_S^* - T_S$) versus true surface temperatures (T_S) after applying the entire algorithm utilizing the <i>water/vegetation</i> data set and simulated nighttime data . .	43
4.6	Temperature retrieval errors ($T_S^* - T_S$) versus TIR transmission after applying the entire algorithm utilizing the <i>water/vegetation</i> data set (subset warm/dry) and simulated nighttime data	44
5.1	Ground radiances in the MIR and TIR channels and the corresponding surface temperatures for four standard atmospheres coupled to a soil surface	50
5.2	Brightness temperatures according to ground radiances in the MIR and TIR channels and the corresponding surface temperatures for four standard atmospheres coupled to a soil surface	51
5.3	Non-linear least square fit for the Planck function integrated over wavenumbers and normalized by the MIR channel width	52
5.4	Non-linear least square fit for the Planck function integrated over wavenumbers and normalized by the TIR channel width	53
5.5	Several radiance ratios in relation to the surface temperature for a soil surface, different atmospheres and the angles, $\theta_s = 45^\circ$, $\theta_v = 0^\circ$	58
5.6	Relation between emissivity ratio ($TISIE_a$) and the ratio of ground radiances for several surface temperatures, mid latitude summer standard atmosphere and the angles, $\theta_s = 45^\circ$, $\theta_v = 0^\circ$	60
5.7	Same as Figure 5.6 but the emissivity ratio is $TISIE_b$	61

5.8	Variation of the regression parameters for $TISIE_a$ with the surface temperature T_S and the brightness temperatures at ground $T_{B,1}^{grd}$, $T_{B,2}^{grd}$ for a mid latitude summer standard atmosphere	62
5.9	Relation between emissivity ratio ($TISIE_a$) and the ratio of ground radiances for the entire data set	64
5.10	Same as Figure 5.9 but data set points are marked according to their sun zenith angles.	65
5.11	MIR emissivity retrieval errors in relation to surface temperatures considering the entire data set	70
5.12	TIR emissivity retrieval errors in relation to surface temperatures considering the entire data set	71
5.13	Temperature retrieval errors in relation to surface temperatures considering the entire data set	72
5.14	MIR emissivity retrieval errors in relation to surface temperatures and solar zenith angles for a mid latitude summer standard atmosphere	73
5.15	TIR emissivity retrieval errors in relation to surface temperatures and solar zenith angles for a mid latitude summer standard atmosphere	74
5.16	Temperature retrieval errors in relation to surface temperatures and solar zenith angles for a mid latitude summer standard atmosphere	75
5.17	Flow chart for the estimation of the overall simulation error	76
6.1	Flow chart for the application of the “Regression” - Approach	86
6.2	Flow chart for the application of the “TISIE” - Approach	87
A.1	Temperature retrieval errors ($T_S^* - T_S$) versus surface temperatures (T_S) utilizing the <i>blackbody</i> data set and simulated daytime data	93
A.2	Temperature retrieval errors ($T_S^* - T_S$) versus surface temperatures (T_S) utilizing the <i>water/vegetation</i> data set and simulated daytime data	94
A.3	Temperature retrieval errors ($T_S^* - T_S$) versus surface temperatures (T_S) utilizing the <i>bare soil</i> data set and simulated nighttime data	95
A.4	Temperature retrieval errors ($T_S^* - T_S$) versus surface temperatures (T_S) utilizing the data set for <i>urban areas</i> and simulated nighttime data	96
A.5	Temperature retrieval errors ($T_S^* - T_S$) versus surface temperatures (T_S) utilizing the <i>forest</i> data set and simulated nighttime data	97
C.1	MIR emissivity retrieval errors in relation to surface temperatures and solar zenith angles for the tropical standard atmosphere	110

C.2	TIR emissivity retrieval errors in relation to surface temperatures and solar zenith angles for the tropical standard atmosphere	111
C.3	Temperature retrieval errors in relation to surface temperatures and solar zenith angles for the tropical standard atmosphere	112
C.4	MIR emissivity retrieval errors in relation to surface temperatures and solar zenith angles for the mid latitude winter standard atmosphere . .	113
C.5	TIR emissivity retrieval errors in relation to surface temperatures and solar zenith angles for the mid latitude winter standard atmosphere . .	114
C.6	Temperature retrieval errors in relation to surface temperatures and solar zenith angles for the mid latitude winter standard atmosphere . . .	115
C.7	MIR emissivity retrieval errors in relation to surface temperatures and solar zenith angles for the US-standard atmosphere	116
C.8	TIR emissivity retrieval errors in relation to surface temperatures and solar zenith angles for the US-standard atmosphere	117
C.9	Temperature retrieval errors in relation to surface temperatures and solar zenith angles for the US-standard atmosphere	118
C.10	Frequency distribution of errors on the retrieved MIR emissivity using sub-data sets according to standard atmospheres	119
C.11	Frequency distribution of errors on the retrieved TIR emissivity using sub-data sets according to standard atmospheres	120
C.12	Frequency distribution of errors on the retrieved surface temperature using sub-data sets according to standard atmospheres	121

Chapter 1

Introduction

The Earth's surface temperature is a key parameter for understanding of the energetic and hydrological balance of the Earth on a regional and global scale. It is driven by the energetic interactions between solar radiance, atmosphere and surface. Thus, it is a basic input variable for parameterization models of the energy transfer between the atmosphere and the surface as well as for weather forecasting models. Continuous accurate measurements of the regional and global temperature distribution could provide information on its changes and impact on the global climate. Surface temperature measurements have also been used in a variety of applications, such as investigations in agriculture (e.g. soil moisture estimation, monitoring water-stress in crops, frost detection), as initialization data in mesoscale models (e.g. sea breeze circulation and convective cloud formation) and in forest fire mapping.

Since the late 1960s, satellite thermal infrared measurements have been utilized to estimate sea surface temperature (SST) (see review paper by Price (Price, 1984)). The derivation of land surface temperature from space can be traced back to the early 60s when the TIROS-II satellite was launched. Almost forty years later the remote sensing community is in a position to quantify atmospheric and surface effects using theoretical models and field experiments in order to derive sea and land surface temperatures. However, there are still plenty of difficulties connected with the accuracy of validation data, the spectral and spatial resolution of the instruments as well as the in-flight calibration of the thermal sensors. Other problems include the heterogeneity of land surfaces and the averaging of temperatures over large pixel area (e.g. $1 \times 1 \text{ km}$). Land surface temperatures may strongly vary in time (diurnal variation) and space, up to 10 K in just a few centimeters due to e.g. shadowing or topographic effects.

Nevertheless, sea surface temperatures are currently derived operationally using measurements of the Advanced Very High Resolution Radiometer (AVHRR) and of the Along Track Scanning Radiometer (ATSR). The AVHRR is on board of the NOAA series of polar-orbiting satellites. The payload of the ATSR is the ERS (European Remote sensing Satellite) platform. SST algorithms have been fine-tuned over the years by adequate theoretical models providing SST accuracies of better than 1 K (Prata, 1993; Vass & Battrick, 1992). For a review of the theory see McMillin et al., Barton

et al. or Deschamps et al. (McMillin & Crosby, 1984; Barton et al., 1989; Deschamps & Phulpin, 1980). The accuracy (root mean square error) currently attainable lies between 1 and 3 K depending on atmospheric and surface properties.

It seems reasonable to apply proven SST methods to land surfaces. When initial application of SST algorithms to land surface temperature retrieval was unsuccessful, it was recognized that the surface emissivity had additionally to be taken into account. During the past decade significant progress has been made in the estimation of land surface emissivity and temperature from thermal remote sensing data (Prata, 1994b; Prata et al., 1995; Wan & Dozier, 1989).

In general, three basic methods have been developed to estimate surface temperatures and are briefly recalled here:

- The first category is called “single-channel method”, which uses the radiance measured by the satellite in one infrared channel. The chosen channel should lie in a so-called “atmospheric window” where the atmospheric extinction is small. The best atmospheric window appropriate for temperature retrieval lies between 10 and 12 μm . The method requires a good radiative transfer model and atmospheric input parameters (profiles) given by atmospheric radiosondes at best or climatological data in order to correct the at-sensor radiance for residual atmospheric absorption (Price, 1983).
- The commonly used “split-window technique” is the second type. There exist both multi-spectral and multi-angular version of the split window technique. The multi-spectral technique, first proposed by McMillin (McMillin, 1975), is based on differential atmospheric absorption in two or more adjacent infrared window channels. The surface temperature is determined by a linear combination of radiometric (brightness) temperatures in those channels (Becker & Li, 1990b; Ottlé & Vidal-Madjar, 1992; Ulivieri et al., 1994; Sobrino et al., 1994; Coll et al., 1994). The multi-angular methods utilize the differential absorption due to different atmospheric path length when the same surface area (pixel) is observed from two or more different view angles (Chedin et al., 1982; Prata, 1994a; Labeled et al., 1993). Combinations of both split-window types have been investigated as well (Wan & Snyder, 1999; Lippert, 1995; Prata, 1993).
- The “separation method” developed by Li and Becker (Becker & Li, 1990a) estimates both land surface emissivity and temperature using pairs of day/night co-registered AVHRR images. A similar approach was derived and adapted for MODIS data by Wan and Li (Wan & Li, 1997). Goita and Royer (Goita & Royer, 1997) proposed a separation approach combining TIR and MIR AVHRR data.

In recent years the validation of developed emissivity and temperature retrieval approaches has focused on measurements of AVHRR because of its widespread use and global applicability (Francois & Ottlé, 1996; Li & Becker, 1993; Kerr et al., 1992; Sobrino et al., 1991). Naturally, most investigated methods are validated on a local or regional scale. New aspects were brought into the discussion with the opportunity

to consider view angle measurements of the ATSR since the beginning of the nineties (Prata et al., 1990; Sobrino et al., 1996). However, reliable land surface temperatures derived from spaceborne thermal sensors are not yet feasible for operational usage.

At the Institute of Space Sensor Technology and Planetary Exploration at the German Aerospace Center (Deutsches Zentrum für Luft- und Raumfahrt - DLR), a small satellite called BIRD (Bi-spectral InfraRed Detection) has been developed. It is slated to be launched in 2001. The BIRD mission shall demonstrate the technological and scientific feasibility of a remote sensing small satellite mission under tight budget constraints (Brieß et al., 1997). The main scientific objectives of the BIRD mission are the investigation of high-temperature-events (HTE) like fires, volcanos etc. and vegetation exploration (Brieß et al., 1999). According to the technological and scientific objectives a sensor system consisting of two IR cameras ($3.4 - 4.2 \mu m$ (MIR - Mid InfraRed) and $8.5 - 9.3 \mu m$ (TIR - Thermal InfraRed)) as well as a stereo camera WAOSS (Wide-Angle Optoelectronic Stereo Scanner) which spectral ranges lie within the visible (VIS) and the near infrared (NIR) was chosen.

The scientific tasks include the development of temperature retrieval methods for HTE (Zhukov et al., 1997) as well as for “normal” Earth’s surface temperature like the temperature of vegetation, etc.

With the given IR channel selection, it follows that none of the existing temperature retrieval methods (utilizing the window channels between 10 and $12 \mu m$ summarized above) can be applied to upcoming BIRD data with the purpose of retrieving “normal” surface temperatures. Thus, it was necessary to investigate temperature retrieval algorithms for land surfaces which utilized the specified channel configuration of BIRD ($3.4 - 4.2 \mu m$ and $8.5 - 9.3 \mu m$).

Two temperature retrieval methods customized for the BIRD channel configuration were investigated. One method is based on a bi-spectral technique (referred to as “Regression” - Approach) using the at-sensor information in the MIR and TIR channels of BIRD (Chapter 4). The second approach (Chapter 5) recovers land surface emissivity and temperature from ground radiances (separation method) utilizing a “Temperature Independent Spectral Index for Emissivity” (referred to as “TISIE” - Approach) (Becker & Li, 1990a). Both methods were developed under the assumption of a Lambertian surface and homogeneous ground pixels. Since the orbit of BIRD is still not fixed, night- as well as daytime conditions were considered in the investigation of methods.

These two main chapters are framed by two general (Chapters 2 and 3) and one out-looking chapter (Chapter 6). In Chapter 2 the BIRD mission is further discussed. Chapter 3 contains the main atmospheric radiative transfer equations in the infrared which are necessary to be solved in order to derive temperature and emissivity. The results of a sensitivity study employed to BIRDs infrared channels are also given in this chapter. A summary of both approaches concerning the error estimation and propagation are included in Chapter 6. In this chapter, an outlook on the algorithms which will be applied on upcoming BIRD data is given as well. Finally, a conclusion, a list of used abbreviations and symbols as well as appendices are provided at the end of the document.

Chapter 2

The BIRD Mission

The BIRD (**Bi-spectral InfraRed Detection**) mission of the German Aerospace Center (DLR) shall demonstrate the technological and scientific feasibility of a remote sensing small satellite mission under low budget constrains (Brieß et al., 1997). In this chapter the mission objectives and the technical data of BIRD are briefly summarized.

2.1 Objectives

The main scientific objectives of the BIRD mission are the investigation of hot spots and vegetation exploration (Brieß et al., 1999). The hot spots can be caused by vegetation fires, industrial hazards and burning oil wells or coal seams as well as volcanic activities. The vegetation exploration includes the study of aridness and re-cultivation. Within these objectives the development of temperature retrieval methods for High-Temperature-Events (HTE) and “normal” Earth’s surface ($\approx 290 \pm 30 K$) are a main focus. The temperature determination of HTE like fires and volcanos are needed for the estimation of pollutant emission into the atmosphere. Retrieved “normal” Earth’s temperatures are required as HTE surrounding temperatures for the interpretation of thermal images. Primary and secondary mission objectives are outlined in the following table (Table 2.1).

BIRD mission objectives	
primary objectives	1. testing a new generation of cooled infrared detectors 2. detection and investigation of hot spots (fires, volcanic activities, burning oil wells or coal seams)
secondary objectives	3. thematic on-board data processing: test of neural network classification 4. exploration of vegetation conditions and changes: determination of “normal” surface temperature, leaf area and vegetation indices 5. real time discrimination between smoke and clouds

Table 2.1: BIRD mission objectives

2.2 Technical Data Overview

With BIRD a new generation of space-borne imaging infrared detectors will be tested. The payload is a three-axis stabilized spacecraft with dimensions of $62 \times 160 \times 62 \text{ cm}^3$ and a mass of 88 kg (Walter et al., 1999). The flight configuration with one fixed and two deployed solar panels as illustrated in Figure 2.1 provides 200 W peak power.

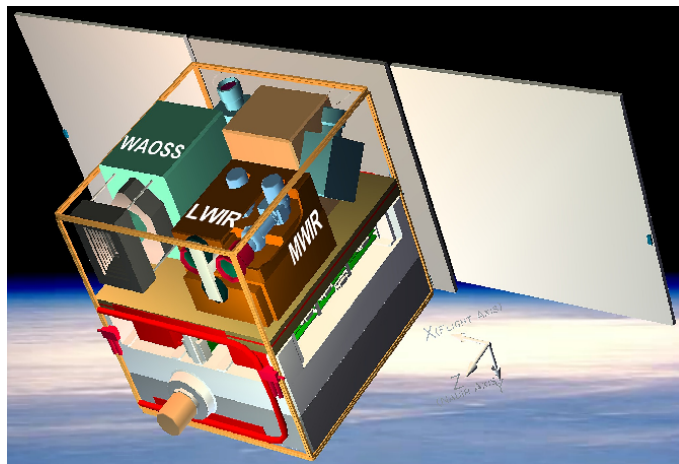


Figure 2.1: Flight configuration of BIRD, (LWIR=TIR, MWIR=MIR)

This multi-spectral sensor system is slated to be launched in 2001 as a piggy-back payload. It consists of two IR cameras, sensitive at wavelength between $3.4 - 4.2 \mu\text{m}$ (MIR - Mid InfraRed) and $8.5 - 9.3 \mu\text{m}$ (TIR - Thermal InfraRed), as well as the stereo camera WAOSS-B (Wide-Angle Optoelectronic Stereo Scanner) with the spectral channels in the visible (VIS, mainly within the red range) and the near infrared (NIR). WAOSS-B was originally developed for the MARS-96 mission and has been slightly modified for the BIRD mission. The IR detectors are made of HgCdTe (Mercury Cadmium Tellurite) and cooled down to 80 K operating temperature by a separate Stirling cooler. The entire system was thoroughly tested under laboratory conditions. Several airborne campaigns demonstrated the feasibility of the BIRD imaging concept.

As an example, the MIR and the TIR images as shown in Fig. 2.2 were taken over the industrial plant in Oberpfaffenhofen on October, 22 in 1998. An arrangement of several fires and hot plates was detected from an altitude of 1200 m (ground resolution $\approx 1.5 \text{ m}$). The large fire in the center (5 m^2) had a temperature of about 550°C . The small fires around covered an area of 1 m^2 and had a temperature of 300°C . The bright stripes were caused by the blooming effect which is related to the saturation of the detector element (Skrbek, 1999). The colors do not correspond to a radiometric quantity. They are used to emphasize the hot areas. The quality of the calibrated data does not yet allow any algorithm validation, although the images prove the scientific applicability of upcoming BIRD data. In Table 2.2 the main technical parameters of BIRD's sensors are summarized assuming a payload at a planned altitude¹ of 450 km .

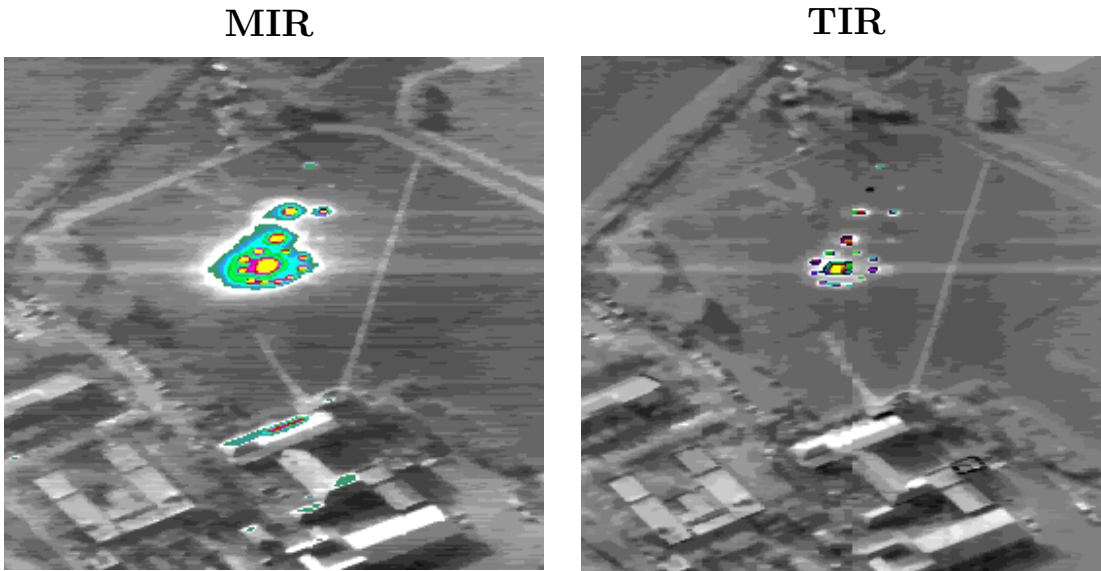


Figure 2.2: MIR and TIR images from the airborne experiment in Oberpfaffenhofen on the 10/22/1998, crossing time: 3:30 pm (local time), altitude: 1200 m

	WAOSS-B	IR-sensors
Spectral bands	600 – 700 nm 840 – 890 nm	3.4 – 4.2 μm 8.5 – 9.3 μm
Focal length	21.65 mm	46.39 mm
F-number	2.8	2.0
FOV	50°	19°
Pixel size	7 × 7 μm^2	30 × 30 μm^2
Number of pixels per line	2884	2 × 512 staggered
Ground pixel size	145 m	290 m
Swath width	418 km	148 km
Quantization	11bit	16bit
Data rate (average/peak)	597/600 kbps	693/4790 kbps
Power consumption	18 W	42 W incl. electr. unit
Mass	8.4 kg	7.3 kg camera head 6.5 kg electronic unit

Table 2.2: Technical parameters of the BIRD instruments assuming a payload at 450 km altitude¹

¹Only since 04/07/00 the final parameters are known, altitude: 572 km, sun-synchronous orbit, local equatorial crossing time: 10:30 am

Spectral Response Functions of the BIRD Sensors

Each sensor is characterized by its response functions $f_{r,i}(\lambda)$ for each of its channels i where λ is the wavelength. The spectral characteristic of the BIRD channels are plotted in Figure 2.3. The channel-integrated value $Q_i(\cdot)$ of any spectral function $Q(\lambda, \cdot)$, e.g. atmospheric radiances, atmospheric transmission, is defined as:

$$Q_i(\cdot) = \frac{\int_{\lambda_i} f_{r,i}(\lambda') Q(\lambda', \cdot) d\lambda'}{\int_{\lambda_i} f_{r,i}(\lambda') d\lambda'} \quad (2.1)$$

Since the upper limit of the MIR channel is very close to the strong $4.3 \mu m$ CO_2 absorption band, the channel integrated quantities, essentially the band integrated MIR transmission, might be rather sensitive to the details of the filter shape beyond the nominal limit of $4.2 \mu m$. In this work the MIR channel limits have been set at the nominal values to avoid extra unnecessary complications at this stage of BIRD algorithm developments. Once the actual MIR channel filter function is precisely known, some additional test might be necessary to assess the impact of residual marginal atmospheric effects.

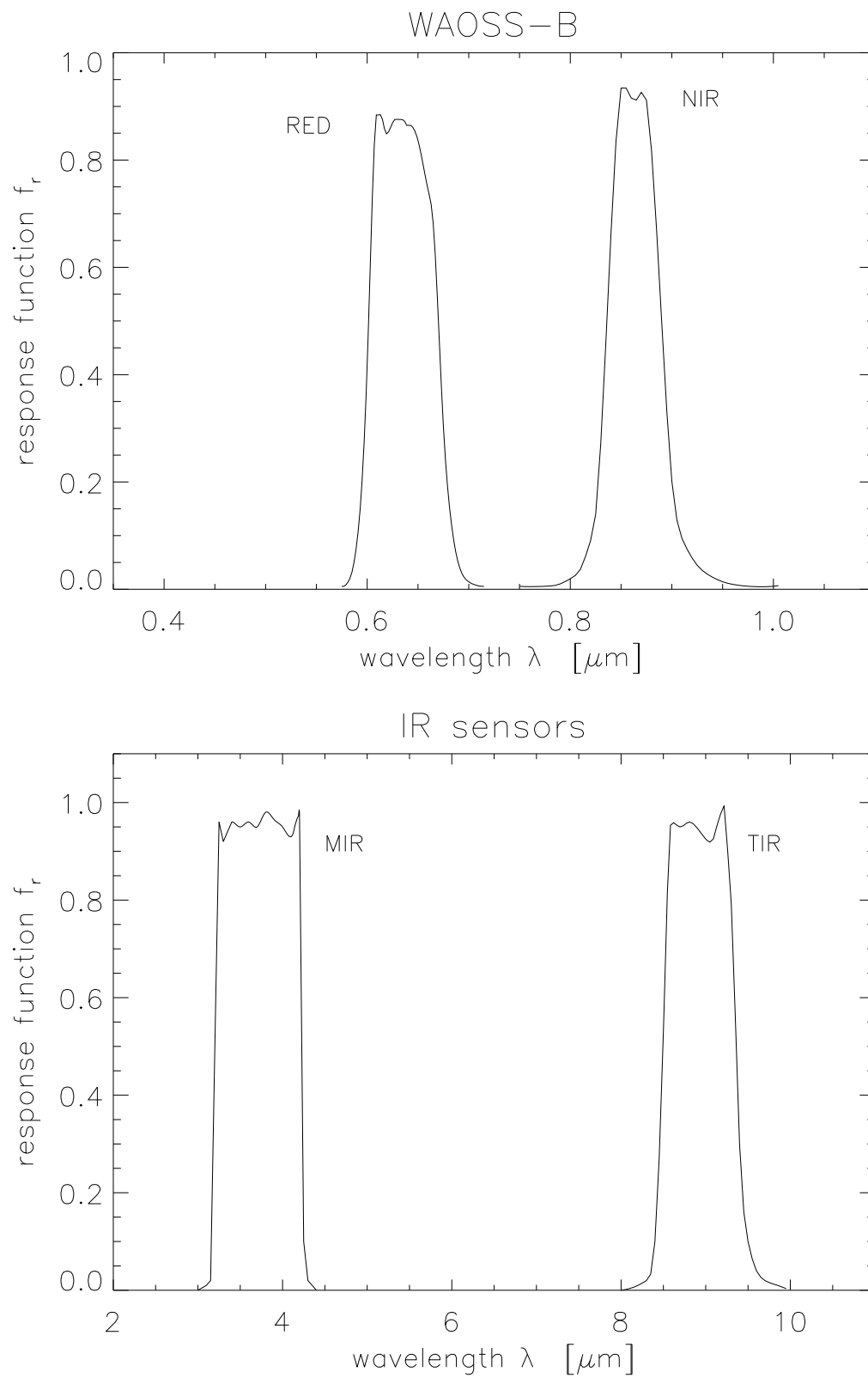


Figure 2.3: Response functions of the BIRD sensors

Chapter 3

Atmospheric Radiative Transfer

The main problem in surface temperature retrieval from space is the modification of the surface radiation on its way through the atmosphere and the contribution of the atmosphere itself to the final signal measured by the sensor. This modification strongly depends on the content of atmospheric constituents as water vapor, ozone, UNIFormly mixed gases (UNIF: CO₂, CO, CH₄, N₂O, O₂) as well as on the temperature profile and aerosol amount.

Figure 3.1 displays the **absorption properties** of several atmospheric gases for an US standard atmosphere (Berk et al., 1989) including rural aerosol and a cirrus cloud of a geometrical thickness of 0.9 km in an altitude of 10 km. The water vapor content W of this atmosphere is 2.2 g/cm².

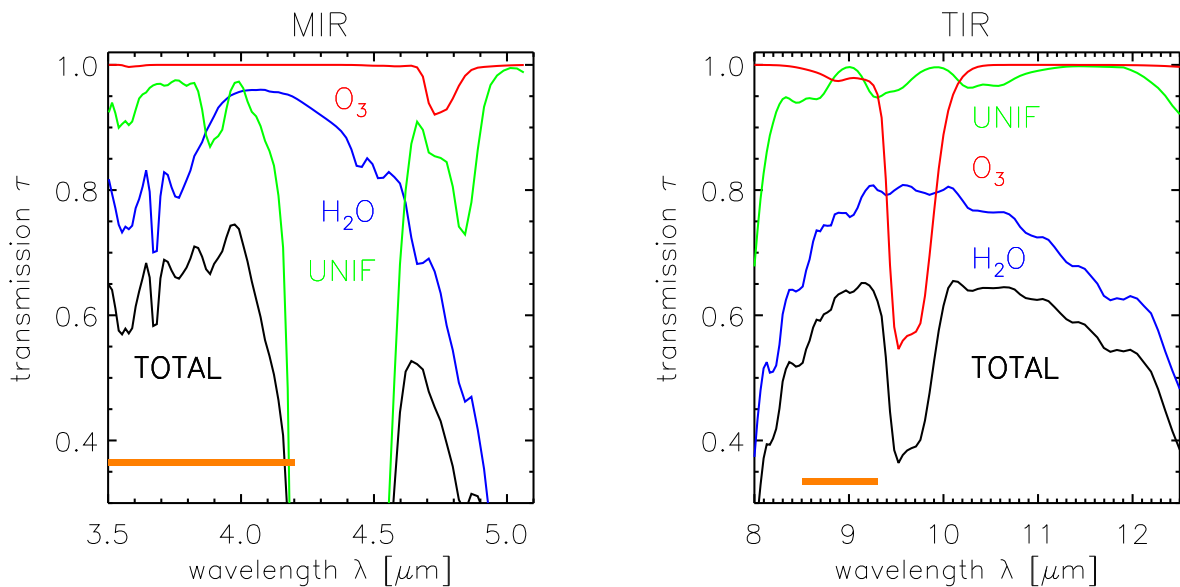


Figure 3.1: Transmission τ of atmospheric gases for an US standard atmosphere ($W = 2.2 \text{ g/cm}^2$), rural aerosol, cirrus cloud of a geometrical thickness of 0.9 km in an altitude of 10 km, orange bars = BIRD channels

The MIR range is divided by the UNIF absorption mainly induced by N_2O and CO_2 . The ozone absorption splits the thermal infrared region into two parts such that one is more transparent than the other (see shape of ozone and total transmission in Figure 3.1). In both IR ranges water vapor is the primary absorber and therefore substantially responsible for the shape of the total transmission. The plotted water vapor absorption considers the absorbing properties of water vapor caused by the continuum (H_2O_C) as well as the molecular (H_2O_M).

The total transmission is calculated according to MODTRAN as follows. The given transmission values are for the wavelength λ equal to $\approx 11 \mu m$.

$$\tau_{total} = \underbrace{\tau_{H_2O_M} * \tau_{H_2O_C}}_{\tau_{H_2O}} * \tau_{O_3} * \tau_{unif} * \tau_{trace} * \tau_{aerosol} * \tau_{cirrus}$$

$$\tau_{total}^{11 \mu m} \approx 0.94 * 0.77 * 0.99 * 0.99 * 0.99 * 0.98 * 0.89 \approx 0.61$$

with

$$\tau_{unif} = \tau_{CO_2} * \tau_{CO} * \tau_{CH_4} * \tau_{N_2O} * \tau_{O_2}$$

$$\tau_{trace} = \tau_{NH_3} * \tau_{NO} * \tau_{NO_2} * \tau_{SO_2} * \tau_{HNO_3}$$

As seen from Figure 3.1 three spectral bands, the so-called atmospheric windows, allow remote sensing of surface properties like the surface temperature and emissivity. Due to the primary BIRD mission's objective and some technological constraints the orange marked channels were chosen for BIRD. Hence, a normally used split window technique for temperature retrieval utilizing two channels between $10 \mu m$ and $12 \mu m$ cannot be applied here (see Chapter 1).

The spherical coordinate system defining the sun and observer position and their corresponding angles is illustrated in the following figure (Fig. 3.2) (Villeneuve, 1996; Lippert et al., 1996).

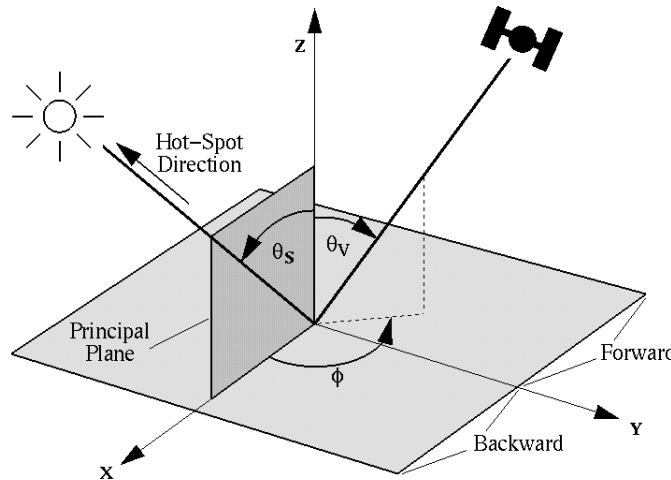


Figure 3.2: Spherical coordinate system defining position of observer relative to the principal plane and indicating the solar hot-spot direction and the backward and forward scattering regions

$\phi = \phi_v - \phi_s$ is the azimuth angle relative to the solar azimuth, with ϕ_v as the view azimuth and ϕ_s as the solar azimuth. Because BIRD will only measure at nadir ($\theta_v = 0$) in the MIR and TIR the relative azimuth ϕ is not relevant. The view angle effects on the edge of remote sensing images as well as slope effects were not subject of these investigations.

The top-of-atmosphere (TOA) radiance (at-sensor radiance) consists of several radiative components. A simplified model of that **complex radiative transfer** process is illustrated in Figures 3.3. “Black” denotes the radiative contributions within TIR during day- and nighttime and within MIR during nighttime only. “Orange” indicates additional solar radiative contribution during daytime within the MIR.

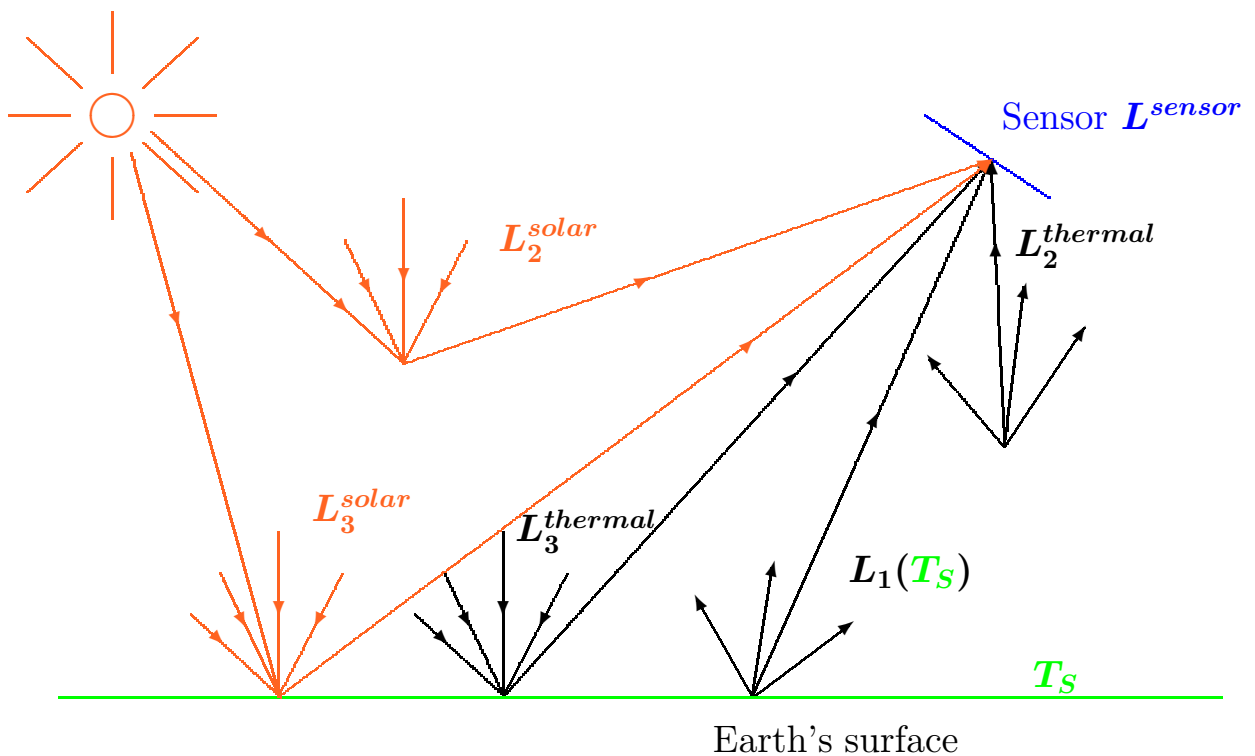


Figure 3.3: Simplified (Multiple scattering and diffuse contributions are not completely displayed.) description of the atmospheric radiative transfer within the infrared (L =radiance, T_S =temperature of the Earth's surface) (Note, that each radiation part is pixel related.)

In the TIR the channel-integrated radiance at the top-of-atmosphere L^{sensor} , the signal measured by the BIRD sensors, consists of the radiance emitted from the ground surface and attenuated by the atmosphere $L_1(T_S)$, the upwelling pathradiance emitted by the atmospheric constituents $L_2^{thermal}$, and the downwelling atmospheric radiation reflected by the surface $L_3^{thermal}$. In the MIR the signal is additionally contaminated by the surface reflected solar radiance L_3^{solar} and by the solar atmospheric pathradiance L_2^{solar} .

Thus, the final signal L_i^{toa} for a Lambertian surface can be expressed by the sum of the following channel-integrated (see Section 2.2) radiative transfer terms:²

$$\underbrace{L_i^{toa}}_{L_{sensor}} = \underbrace{\varepsilon_i B_i(T_S)}_{L_1(T_S)} \tau_i + \underbrace{L_i^{atm\uparrow}}_{L_2^{solar} + L_2^{thermal}} + \underbrace{(1 - \varepsilon_i) L_i^{atm\downarrow}}_{L_3^{thermal} + L_{sdif}} \tau_i + \underbrace{(1 - \varepsilon_i) \tau_i^{sun} \frac{E_i^{sun}}{\pi}}_{L_3^{solar}} \cos \theta_S \tau_i \quad (3.1)$$

with

index i	indicates channel-integrated values for BIRD's MIR ($i = 1$) and TIR ($i = 2$) channels
ε_i	emissivity
τ_i	atmospheric transmittance (nadir direction $\theta_v = 0^\circ$)
τ_i^{sun}	transmittance in solar incidence direction θ_s
$B_i(T_S)$	blackbody radiance of the surface temperature T_S
$L_i^{toa} = B_i(T_i)$	at-sensor radiance for the brightness temperature T_i according to the Planck function B_i integrated over channel i (see explanation on the next page)
$L_i^{atm\downarrow}$	hemispheric average downwelling atmospheric radiance ³ (solar diffuse and thermal)
$L_i^{atm\uparrow}$	directional upwelling atmospheric solar and thermal radiance
E_i^{sun}	extraterrestrial solar irradiance already corrected for the variation of the Earth-Sun distance

The solar contribution is negligible in the TIR channel. Considering a Lambertian surface the directional hemispheric reflectivity ρ_{h_i} can be replaced by $(1 - \varepsilon_i)$. Since the bidirectional reflectivity ρ_{b_i} becomes equal to ρ_{h_i}/π for Lambertian surfaces, ρ_{b_i} is given by $(1 - \varepsilon_i)/\pi$. A more detailed mathematical description of the radiative transfer quantities is to be found in (Lenoble, 1993; Lion, 1980; Feigelson, 1984).

By reason of the discussed subject in this document - temperature retrieval - the definition of the **spectral emissivity** and the **spectral Planck function** shall briefly be recalled.

The spectral emissivity ε_λ is defined as the ratio of the spectral radiance $L_\lambda(T)$ emitted by any body at the temperature T and the spectral radiance $B_\lambda(T)$ emitted by a blackbody at the same temperature T :

$$\varepsilon_\lambda = \frac{L_\lambda(T)}{B_\lambda(T)} \quad (3.2)$$

²Here, the notations $L_1(T_S)$, $L_2^{thermal}$, $L_3^{thermal}$, L_2^{solar} , L_3^{solar} used in Fig. 3.3 are assigned to their mathematical expressions. Their numbering must not be mixed up with the index $i = 1, 2$ which indicates the infrared BIRD channels. The solar diffuse radiance L^{sdif} is not included in Fig. 3.3.

³reflected hemispheric average downwelling atmospheric radiance $(1 - \varepsilon_i) L_i^{atm\downarrow}$:

$$\int_{\Omega} \rho_{b_i} L_i^{atm\downarrow'}(\Omega) \cos \theta d\Omega = \rho_{b_i} \int_{\Omega} L_i^{atm\downarrow'}(\Omega) \cos \theta d\Omega = (1 - \varepsilon_i) \underbrace{\frac{1}{\pi} \int_{\Omega} L_i^{atm\downarrow'}(\Omega) \cos \theta d\Omega}_{L_i^{atm\downarrow}}$$

The Planck's function $B_\lambda(T)$ describes the spectral radiance at wavelength λ of a blackbody at temperature T assuming a thermodynamic equilibrium. $B_\lambda(T)$ is defined as the radiant energy emitted from a blackbody unit surface in a unit solid angle within a unit of wavelength width and time unit (Lenoble, 1993).

$$\begin{aligned}
 B_\lambda(T) &= \frac{c_1 \lambda^{-5}}{\exp\left(\frac{c_2}{\lambda T}\right) - 1} & B_\nu(T) &= \frac{c'_1 \nu^3}{\exp\left(\frac{c'_2 \nu}{T}\right) - 1} \\
 \lambda [\mu m] && \nu [cm^{-1}] & \\
 B_\lambda [Wm^{-2}sr^{-1}\mu m^{-1}] && B_\nu [Wm^{-2}sr^{-1}(cm^{-1})^{-1}] & \\
 c_1 = 2hc^2 = 1.1911 \cdot 10^8 Wm^{-2}sr^{-1}\mu m^4 && c'_1 = 1.1911 \cdot 10^{-8} Wm^{-2}sr^{-1}(cm^{-1})^{-4} & \\
 c_2 = \frac{hc}{k} = 1.439 \cdot 10^4 K\mu m && c'_2 = 1.439 K(cm^{-1})^{-1} &
 \end{aligned}$$

Several definitions of surface temperature exist in relation to radiometry, e.g. see (Becker & Li, 1995; Norman & Becker, 1995). Here, it shall be restricted to the introduction of the radiometric temperature T_{SR} . According to Equation 3.1, the channel-integrated at-ground radiance L_i^{grd} is given by $(L_i^{toa} - L_i^{atm\uparrow})$ divided by the atmospheric transmission τ_i .

$$\underbrace{\frac{L_i^{toa} - L_i^{atm\uparrow}}{\tau_i}}_{L_i^{grd}} = \varepsilon_i B_i(T_S) + (1 - \varepsilon_i) \left(L_i^{atm\downarrow} + \tau_i^{sun} \frac{E_i^{sun}}{\pi} \cos \theta_S \right) \quad (3.3)$$

Equivalent thereto, the spectral at-ground radiance L_λ^{grd} measured by a radiometer or sensor in the thermal infrared can be described by the spectral radiance $L_\lambda^B = \varepsilon_\lambda B_\lambda(T_S)$ emitted by a surface and the reflected downwelling atmospheric spectral radiance $(1 - \varepsilon_\lambda)L_\lambda^{atm\downarrow}$.

$$L_\lambda^{grd} = L_\lambda^B + (1 - \varepsilon_\lambda) \left(L_\lambda^{atm\downarrow} + \tau_\lambda^{sun} \frac{E_\lambda^{sun}}{\pi} \cos \theta_S \right) \quad (3.4)$$

where

$$L_\lambda^B = \varepsilon_\lambda B_\lambda(T_{SR}) \quad (3.5)$$

From the last equation, the radiometric temperature T_{SR} is the temperature of a blackbody with the radiance $L_\lambda^B/\varepsilon_\lambda$ and can be expressed by

$$\begin{aligned}
 T_{SR} &= B^{-1} \left[\frac{L_\lambda^B}{\varepsilon_\lambda} \right] = \frac{c_2}{\lambda \ln \left(\frac{c_1 \varepsilon_\lambda}{\lambda^5 L_\lambda^B} + 1 \right)} \\
 &= B^{-1} \left[\frac{L_\lambda^{grd} - (1 - \varepsilon_\lambda) \left(L_\lambda^{atm\downarrow} + \tau_\lambda^{sun} \frac{E_\lambda^{sun}}{\pi} \cos \theta_S \right)}{\varepsilon_\lambda} \right] \quad (3.6)
 \end{aligned}$$

T_{SR} is further named as surface temperature. This consideration can be adapted to any introduced radiance, e.g. the TOA radiance. Its radiometric temperature is actually the so-called brightness temperature.

For the development of the temperature retrieval algorithm presented throughout this document look-up tables for each BIRD channel containing numerically integrated blackbody radiances and their corresponding radiometric or so-called brightness temperature were established.

In the following figure (Fig. 3.4) the different orders of magnitude of spectral blackbody radiances (emitted) and reflected radiances for grass, clouds and sun glitter effect over a water surface are displayed. Only the direct solar radiative contribution and the emitted surface radiance were considered in the plot. The utilized parameters are:

parameter	grass	cloud	sun glitter
ρ_{h_1}	0.02	0.8	0.02
ρ_{h_2}	0.03	0.8	0.02
$\varepsilon_i, i = 1, 2$		$(1. - \rho_{h_i})$	
T_S [K]	300	220	300

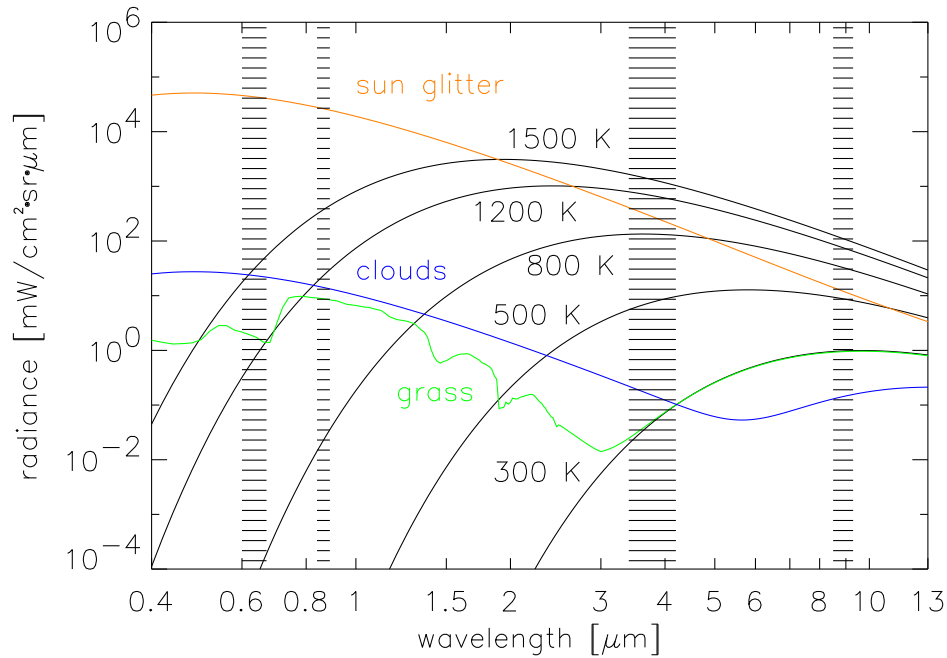


Figure 3.4: Spectral blackbody radiance for several temperatures compared to typical reflectance spectra of natural surfaces (The black bars denote the BIRD channels.)

The MIR range is characterized by the same order of magnitude of the reflected solar radiance and the emitted thermal radiance of a blackbody. The mid infrared spectral

region is suited for the detection of high-temperature-events ($T \gtrsim 500 K$) because their emission is several orders of magnitude higher than the solar reflection and the Earth's emission. Therefore, HTEs and their backgrounds (surrounding areas of HTE), except sun glitter and high albedo surfaces, are well contrasted in remote sensing images. The maximum of the blackbody emission for the mean Earth's surface temperature of $300 K$ corresponds to the atmospheric window between $8 \mu m$ and $12 \mu m$ which makes this window appropriate for the monitoring of natural surfaces.

3.1 Sensitivity Analysis

Since BIRD will not provide common temperature retrieval channels a sensitivity analysis of the atmospheric influence on the sensor signal was called for before starting the algorithm development. The impact of the estimation error for atmospheric parameters on the surface temperature to be retrieved from the top-of-atmosphere radiance was the main point of interest.

Impact of the Estimation Error for Atmospheric Parameters on the Surface Temperature

Within the spectral region of BIRD atmospheric parameters like humidity, atmospheric temperature profile and aerosols mainly influence the radiative transfer (Fig. 3.1). The effect on their uncertainties was studied independent of each other while the surface temperature was varied.

BIRD's relevant synthetic TOA radiances are based on four standard atmospheric profiles (Tab. 3.1) included in MODTRAN3.5 (Berk et al., 1989), (Abreu et al., 1995). The following nomenclature is used throughout this document:

standard atmosphere		atmospheric parameter	
name	abbreviation	temperature profile	water vapor content
tropical	TROP	T^{trop}	W^{trop}
mid latitude summer	MLS	T^{mls}	W^{mls}
mid latitude winter	MLW	T^{mlw}	W^{mlw}
US standard	US-ST	T^{us}	W^{us}

Table 3.1: Nomenclature for standard atmospheres used in the sensitivity analysis

The amount of atmospheric parameters for each standard atmosphere is summarized in Table 3.2. All sensitivity experiments were performed for nadir observations and a blackbody ($\varepsilon = 1$) therefore the reflected radiation parts ($L_3^{thermal} + L^{sdif}, L_3^{solar}$) are not to be considered for that case (see Eq. 3.1). The sun azimuth is assumed as zero. The dependence of the sun zenith angle was investigated for several sun zenith

angles $\theta_s = 0^\circ, 15^\circ, 30^\circ, 45^\circ, 60^\circ$. The variation of the solar radiative contribution to the at-sensor signal due to different sun angles is negligible in relation to the emitted radiance of a blackbody within the considered IR-channels (Lippert, 2000). Thus, all results of the sensitivity study are discussed for a sun zenith angle of 30° . Note, that the assumptions made here are only valid for the sensitivity analysis.

ATM	TROP	MLS	MLW	US-ST
$W_{ref}^{ATM} [g/cm^2]$	4.1	2.9	0.8	1.4
$T_S = T_{bound}^{ATM} [K]$	299.7	294.2	272.2	288.2
aerosol ($A [MU]$)	clear: 0.16 rural: 0.32 urban: 1.17			
aerosol+vc ($AV [MU]$)	clear+vc: 0.25 rural+vc: 0.41 urban+vc: 1.26			

Table 3.2: Amount of atmospheric parameters for standard atmospheres. MU is the MODTRAN unit for aerosol amount A , AV (plus volcanic aerosols) which corresponds to the total vertical aerosol optical depth at 550 nm (nadir view) (Shettle, 2000). (vc - volcanic aerosols)

The influence of uncertainties for each considered parameter was analyzed by comparing the retrieved temperature using a perturbed (further referred to “pert”) atmosphere with the reference (further referred to “ref”) temperature. MODTRAN was used for the calculation of the atmospheric parameters. Figure 3.5 gives an overview on the simulation procedure which leads to the temperature estimation error ΔT_S due to assumed uncertainties in the determination of certain atmospheric parameters, e.g. W^{ATM} . The simulation procedure starts with the calculation of the at-sensor signal using the surface and atmospheric parameters of the reference model. That means, the standard values for the water vapor content W_{ref}^{ATM} and the aerosol amount A_{ref}, AV_{ref} as well as the standard temperature profile T_{ref}^{ATM} were used as input parameters while the surface temperature T_S^{ref} was varied (see below). The subsequent atmospheric correction (solving the radiative transfer equation for the surface temperature T_S^{pert}) is performed with the corresponding parameters of the perturbed model, $W_{pert}^{ATM}, T_{pert}^{ATM}, A_{pert}$ or AV_{pert} . Note, that one of these parameters varies only for determining its influence on the retrieved surface temperature. Finally, the temperature estimation error $\Delta T_S = T_S^{pert} - T_S^{ref}$ due to assumed uncertainties in the determination of certain atmospheric parameters, e.g. ΔW , can be evaluated. A summary of used reference and perturbed models is given in Table 3.3. Atmospheric and surface parameters are not explicitly mentioned here, as atmospheric pressure and gases profiles, remained fixed according to the standard atmosphere used in MODTRAN.

	parameter	reference model	perturbed model
general		$\varepsilon_i = 1, \theta_s = 30^\circ, \phi_s = 0^\circ, \theta_v = 0^\circ$	
	parameters	$T_S^{ref} = T_{bound}^{ATM} + \Delta T_{bound}^{ATM}$	
$\Delta T_{bound}^{trop} = -5 \dots + 20$			
$\Delta T_{bound}^{mils} = -5 \dots + 20$			
$\Delta T_{bound}^{mlw} = -10 \dots + 5$			
$\Delta T_{bound}^{us} = -10 \dots + 10$			
changed	W_{ref}^{ATM} -profile	W_{ref}^{ATM}	$W_{pert}^{ATM} = W_{ref}^{ATM} \pm \Delta W$ $\Delta W = 0, 25, 50, 75$ % of W_{ref}^{ATM}
parameters	T_{ref}^{ATM} -profile	T_{ref}^{ATM}	$T_{pert}^{ATM} = T_{ref}^{ATM} + \Delta T$ -profile ΔT -profile = $-3, 0, 2, 4, 6, 8, 10$ K
	aerosol	$A_{ref} = \text{rural}$	$A_{pert} = \text{clear, rural, urban}$
of perturbed	aerosol+vc	$AV_{ref} = \text{rural}$	$AV_{pert} = \text{aerosol+vc}$

Table 3.3: Summary of reference and perturbed models for the sensitivity analysis, vc - volcanic aerosols, (W^{ATM} and T_S^{ATM} are the actual used values in the simulation for the water vapor content and the surface temperature, respectively. *ATM* is the index for *trop*, *mils*, *mlw*, *us*)

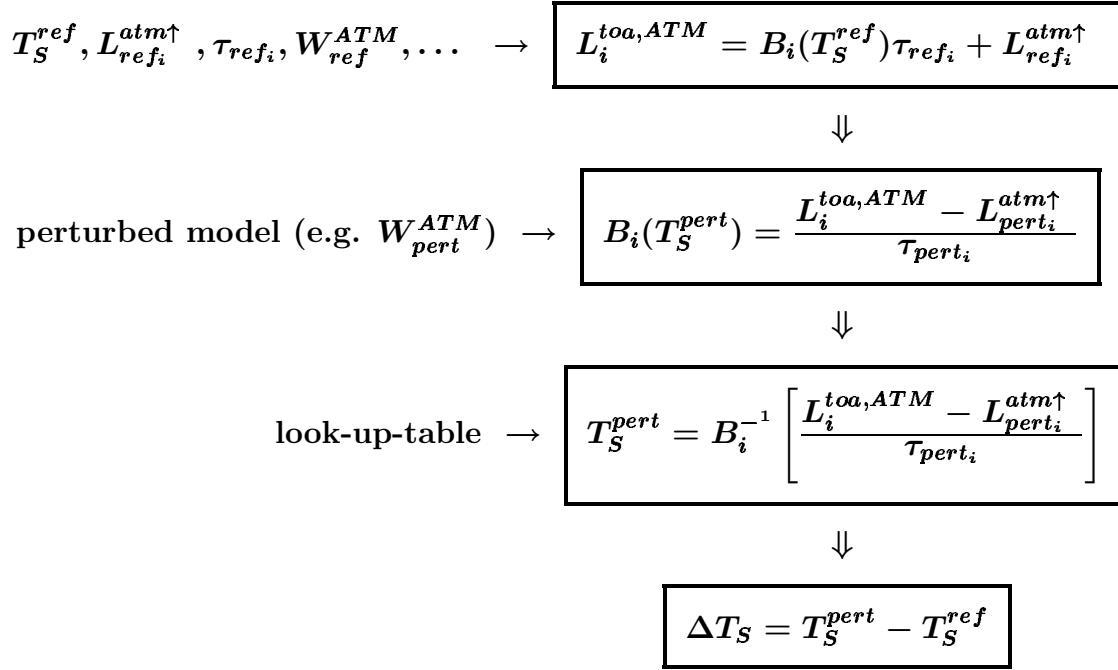


Figure 3.5: Flow chart for the sensitivity analysis procedure; $L_i^{toa,ATM}$: top-of-atmosphere radiance for the standard atmosphere ATM

The variation of the **surface temperature**, T_S^{ATM} , was done in connection with the atmospheric boundary temperature T_{bound}^{ATM} , which is the temperature in the lowest atmospheric layer calculated by MODTRAN. The parameters W_{ref}^{ATM} , T_{ref}^{ATM} , A_{ref} , AV_{ref} are set to the standard values according to the considered atmosphere ATM . The used surface temperature was established by adding to the boundary temperature a certain amount ΔT_{bound}^{ATM} from -10 K up to $+20\text{ K}$ in steps of 5 K depending on the standard atmospheric profile, $T_S^{ATM} = T_{bound}^{ATM} + \Delta T_{bound}^{ATM}$ (see Table 3.3).

For the **humidity analysis** the entire water vapor profile (W^{ATM} -profile) was changed up to $\pm 75\%$ in steps of $\pm 25\%$ (Table 3.3). For keeping the shape of the standard water vapor profile, a certain amount of water vapor, e.g. 50% of the standard value, was added to the actual amount within each atmospheric layer. Figures 3.6 and 3.7 show the surface temperature retrieval error ΔT_S due to assumed uncertainties in the humidity determination ΔW depending on the surface temperature value itself. These figures emphasize that both BIRD channels are highly sensitive to the water vapor estimation error ΔW , although the impact is stronger in the TIR compared to the MIR channel, as easily understood from Figure 3.1. For dry atmospheres (MLW, US-ST) the uncertainties in humidity are almost negligible. On the other hand and in general, for humid atmospheres (TROP, MLS) a positive error in measurement of the water vapor content ($\Delta W > 0$) induces a strong overestimation of the surface temperature

($\Delta T_S > 0$). That might be different in cases as inversion periods during nighttime and if a balance between atmospheric absorption and emission exists. The relation between the water vapor and the surface temperature errors gets more asymmetric with a raising surface temperature itself, which means that a positive uncertainty in humidity ($\Delta W > 0$) has a stronger effect on the temperature error as a negative humidity estimation error ($\Delta W < 0$) of the same absolute value. Several parameterization schemes for the exponential relation between water vapor content and surface temperature can be found in the literature e.g. (Gaffen et al., 1992). As an example, a water vapor estimation error of 25 % in the TIR, follows a temperature retrieval error up to 4 K for a tropical standard atmosphere ($\Delta W = 0.25 \times W_{ref}^{trop}$), whereas an error of -25 % brings up around -3 K. In contrast thereto, an uncertainty in humidity of 25 % within the MIR causes a temperature error smaller than 1 K. Typical precision of humidity measurements by radiosondes lie between ± 2 and 5 % (Elliott & Gaffen, 1991).

The study of the influence of a perturbed **atmospheric temperature profile** was done in the same way as described for the humidity (Table 3.3). A shift of the entire atmospheric temperature profile from -3 K to 10 K adjusted to the concerning standard atmospheres was applied. The impact of uncertainties of the temperature profile is smaller than observed for humidity deviations. As seen in Figures 3.8 and 3.9 the effect of the temperature profile estimation error has only to be considered in the TIR for humid atmospheres. As for the humidity an asymmetric behavior for positive and negative variations is displayed. This can be explained by the physical relation between ΔT_S and ΔT^{ATM} (ΔT -profile). Considering the total differential of Equation 3.1 for the discussed conditions (atmospheric parameters except for T-profile are kept constant, blackbody, etc.) and its setting to zero leads to the following expression:

$$\Delta T_S = -\frac{1 - \tau_i}{\tau_i} \Delta T^{ATM} \quad (3.7)$$

A high water vapor content evokes a low transmittance. Therefore and according to Equation 3.7 a strong variation of the temperature profile induces an even stronger underestimation of the surface temperature ($\Delta T_S < 0$). Equation 3.7 also verifies the results shown in Figure 3.6 and 3.7: In general, the more water vapor the atmosphere contains the higher the absolute value of the temperature retrieval error will be. The conclusions of the temperature profile analysis are in accordance with the outcome of the humidity studies.

Within the **aerosol sensitivity** investigation it is distinguished between three standard aerosol types, clear, rural and urban. Since one of the BIRD mission objectives are volcanic studies (Chapter 2) volcanic aerosol was additionally considered. Note, that the amount of each aerosol type, as found in Table 3.2, is the same for all included atmospheres. The aerosol amount in a certain atmosphere is connected with the humidity of that atmosphere since water vapor is involved within the genesis of aerosol. In case that the aerosol amount is the same for the considered standard atmospheres (MLS, MLW, US, TROP), the differences in the aerosol sensitivity between the atmospheres (see Figures 3.10 and 3.11) are ascribed to the humidity and temperature profiles differences of the atmospheres and thus to different absorption properties of the

standard atmospheres (MLS, MLW, US, TROP). Figures 3.10 and 3.11 show that the MIR channel is more sensitive than the TIR for dry atmospheres due to the wavelength dependence of the aerosol scattering. If one assumes urban instead of rural aerosols the surface temperature will be overestimated by up to 2 K in the MIR and by around 1 K in the TIR. Both channels are almost insensitive to aerosol perturbations if T_{bound}^{ATM} is equal to T_S . It has to be pointed out that the curves $\Delta T_S = f(\Delta A)$ for the different surface temperatures do not exactly merge at $[0, 0]$. This effect is caused by the multiple scattering of the ground radiance. MODTRAN calculates the total atmospheric pathradiance as a sum of the upwelling atmospheric radiance and the scattered ground radiance.

Finally, the inclusion of **volcanic aerosol** amplifies the described sensitivity behavior of aerosol (Fig 3.12 and 3.13). Here, the reference model considers rural but not volcanic aerosols. Thus, ΔT_S is different from zero if ΔAV is equal to zero.

The presented results of the sensitivity analysis emphasize the relation of the atmospheric and surface contribution to the top-of-atmosphere radiance. For humid atmospheres the predominant part comes from the low and mid troposphere, so that the retrieval of the surface temperature will be less accurate. Most reliable surface temperatures can be determined for high surface temperatures and less extinctive atmospheres because of the enhanced contribution of the surface radiation to the final signal.

The results of this section are recalled again in Chapter 6.

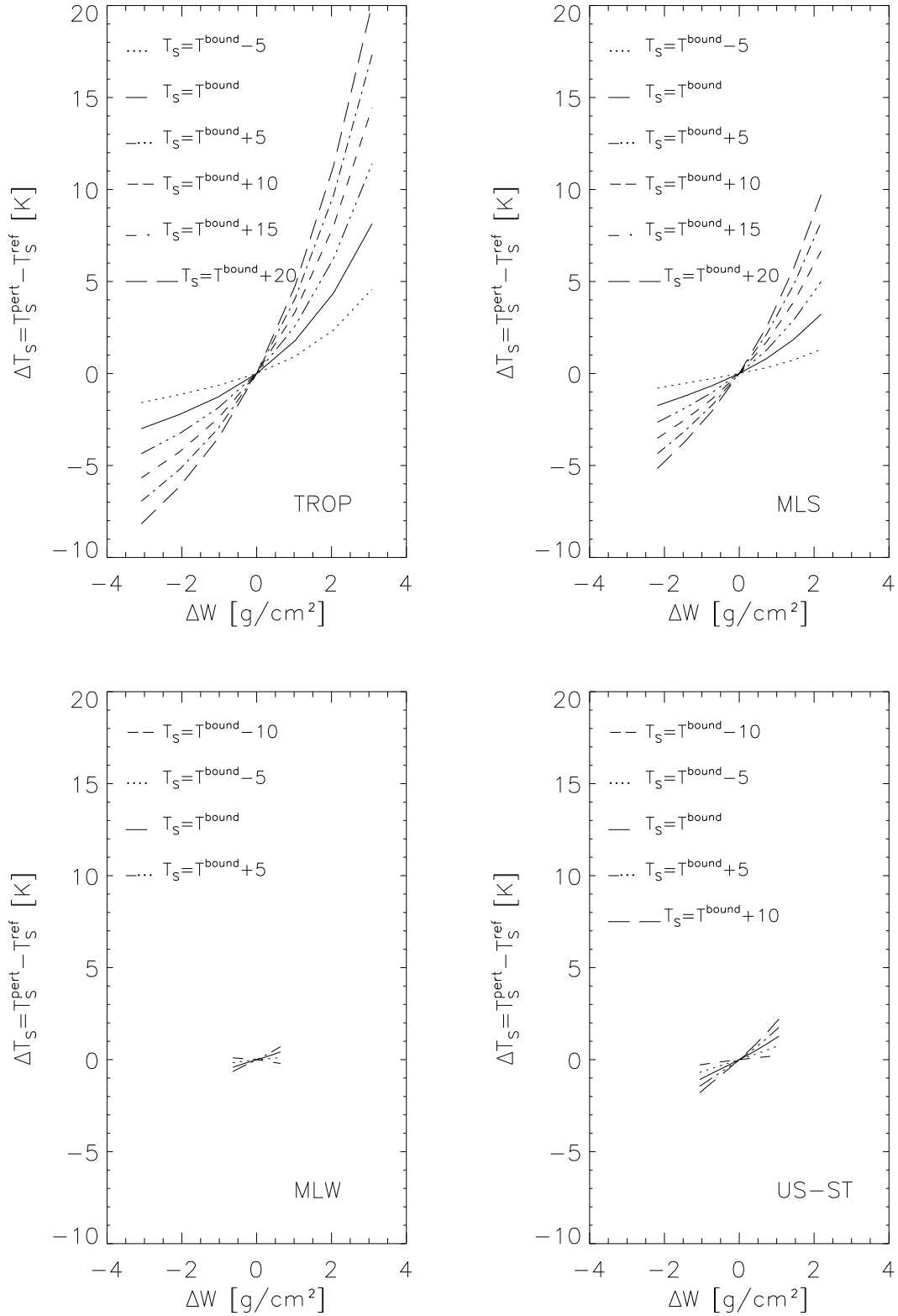


Figure 3.6: Ground temperature error as a function of water vapor for different standard atmospheres, TIR; T^{bound} within the figure corresponds to $T_{\text{bound}}^{\text{ATM}}$ within the text.

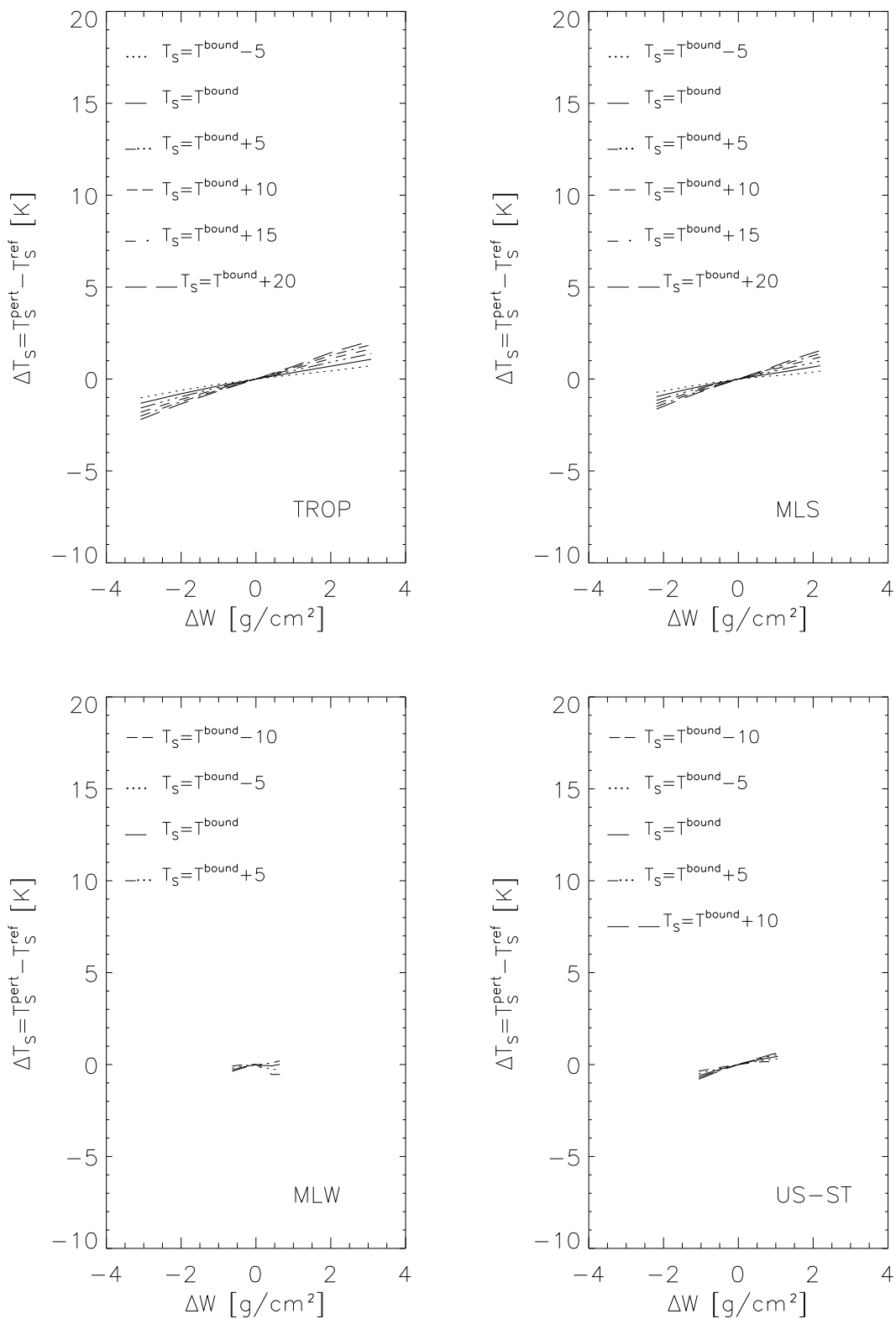


Figure 3.7: Ground temperature error as a function of water vapor for different standard atmospheres, MIR; T^{bound} within the figure corresponds to $T_{\text{bound}}^{\text{ATM}}$ within the text.

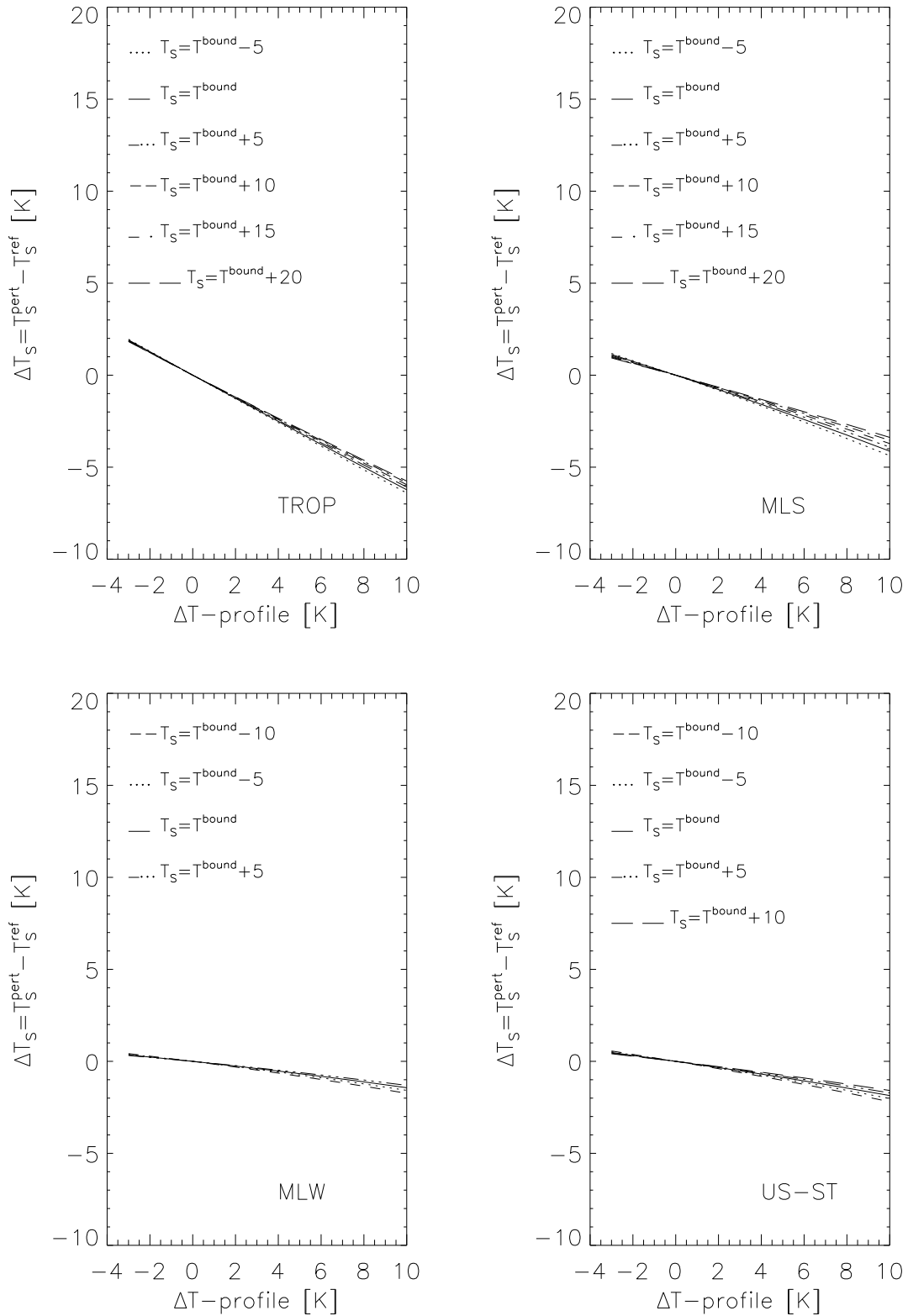


Figure 3.8: Ground temperature error as a function of temperature profile for different standard atmospheres, TIR; T^{bound} within the figure corresponds to $T_{\text{bound}}^{\text{ATM}}$ within the text.

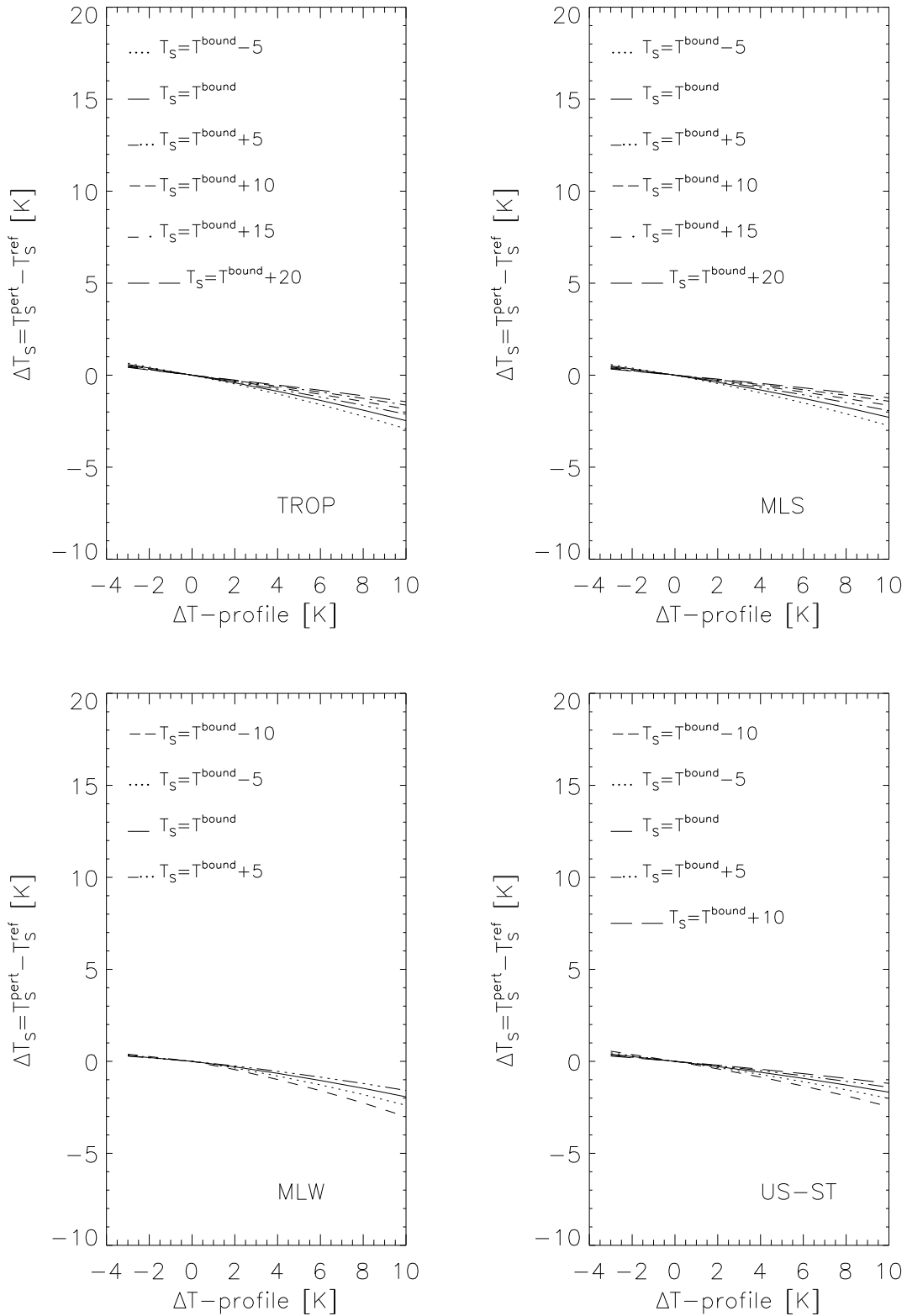


Figure 3.9: Ground temperature error as a function of temperature profile for different standard atmospheres, MIR; T^{bound} within the figure corresponds to $T_{\text{bound}}^{\text{ATM}}$ within the text.

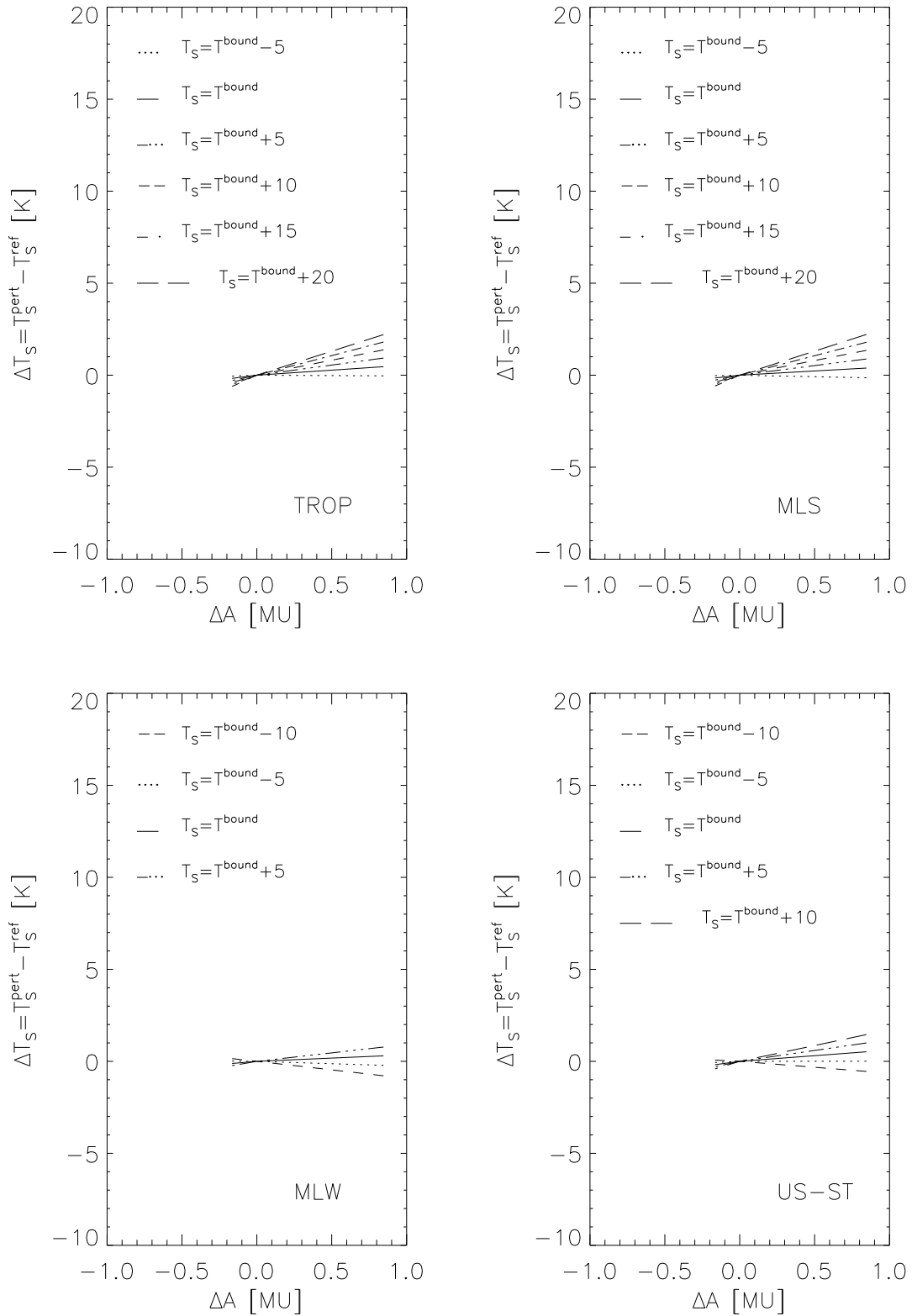


Figure 3.10: Ground temperature error as a function of aerosols for different standard atmospheres, TIR; T^{bound} within the figure corresponds to $T_{\text{bound}}^{\text{ATM}}$ within the text.

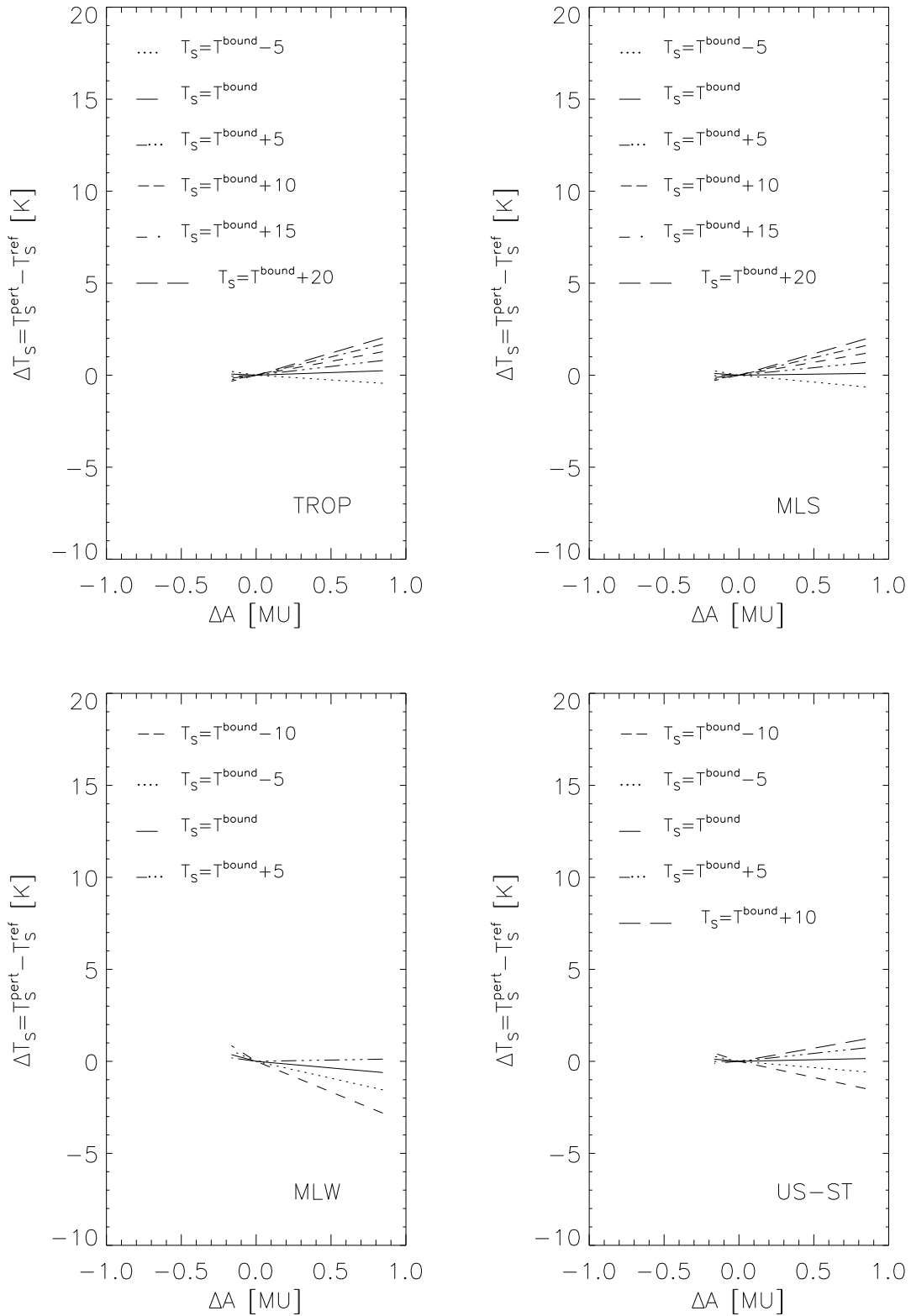


Figure 3.11: Ground temperature error as a function of aerosols for different standard atmospheres, MIR; T^{bound} within the figure corresponds to $T_{\text{bound}}^{\text{ATM}}$ within the text.

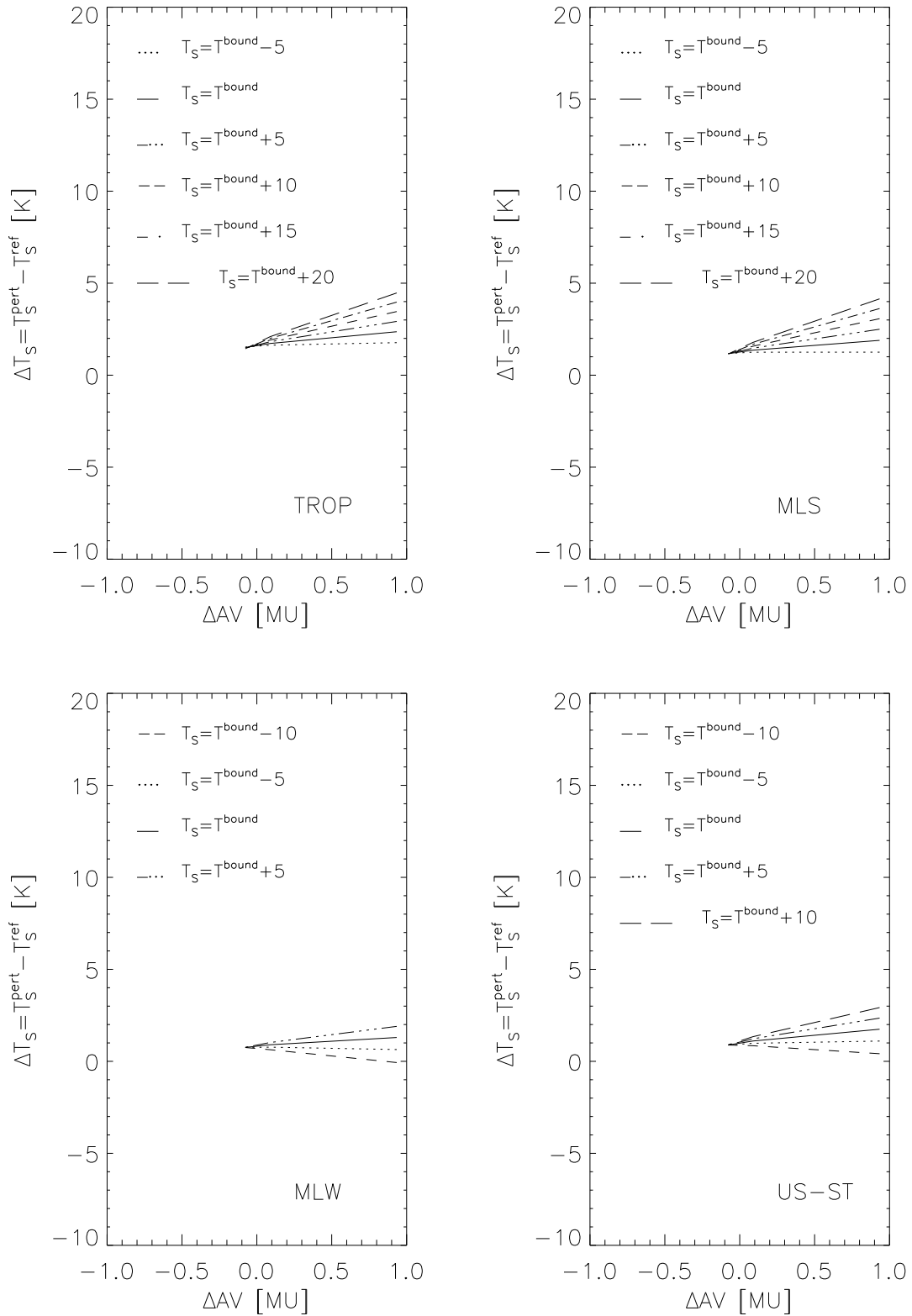


Figure 3.12: Ground temperature error as a function of aerosol plus volcanic aerosol for different standard atmospheres, TIR; T^{bound} within the figure corresponds to $T_{\text{bound}}^{\text{ATM}}$ within the text.

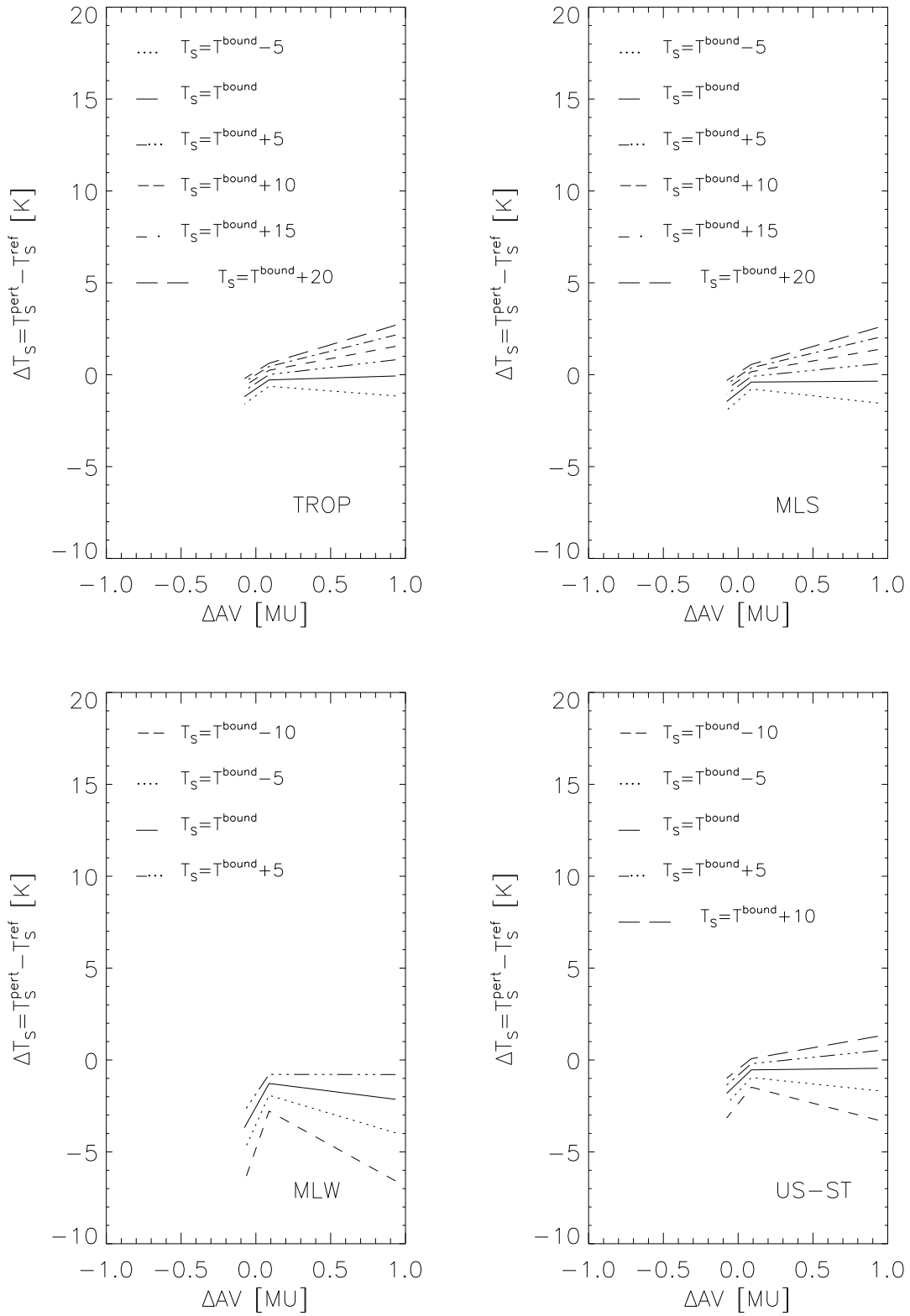


Figure 3.13: Ground temperature error as a function of aerosol plus volcanic aerosols for different standard atmospheres, MIR; T_s^{bound} within the figure corresponds to T_s^{ATM} within the text.

Chapter 4

“Regression” - Approach

Although BIRD will not have any channel within the atmospheric window from 10 μm to 12 μm it seemed to be appropriate to investigate a bi-spectral method utilizing the MIR and TIR channel of BIRD. Both channels correspond to the atmospheric windows around 3.7 μm and 9 μm , respectively (Fig. 3.1).

BIRD mission objectives are focused on land surfaces. The composition of land surfaces is expressed in the parameter emissivity. Thus, an emissivity correction has to be employed additionally to the bi-spectral method. MODTRAN (Berk et al., 1989) was used for the simulation of the atmospheric radiative transfer.

In the following the established “Regression” - Approach for day- and nighttime conditions is described and the results in terms of temperature retrieval errors are discussed.

4.1 Simulated BIRD Data Set

Since the goal is to estimate the surface temperature within a reasonable accuracy, while considering the BIRD mission objectives and the channel configuration, without knowing certain atmospheric parameters in detail, a widely atmosphere-independent algorithm is necessary. A large number of coupled atmospheric and surface models is necessary for establishing a statistical method like a bi-spectral regression. For these purpose an extensive synthetic data set was generated using the radiative transfer model MODTRAN3.5 .

At this stage of BIRD algorithm development the investigations on the approach were concentrated on mid latitudinal atmospheres. Data sets for tropical/summer and sub-arctic/winter conditions are partly generated and further explorations on them will be the subject of future work.

Simulations for the **mid latitude data set** are based on three types of standard atmospheres, mid latitude summer and winter as well as US-standard atmospheres. The used atmospheric temperature profiles correspond to the standard atmospheres called above, respectively (Table 4.1). **Atmospheric water vapor** is the main absorber in the infrared spectral range (see Fig. 3.1). 90 % of the entire atmospheric water vapor

is accumulated in the lower troposphere. Several atmospheric water vapor contents (Table 4.1) were achieved by varying the the amount of water vapor in the first six layers (0 – 6 *km*) of a MODTRAN standard atmosphere only.

temperature profile	water vapor content [g/cm^2]	number
mid latitude summer	1.65 - 4.79, $\Delta = 0.130$	$N_W = 50$
US-standard	0.77 - 2.71, $\Delta = 0.114$	
mid latitude winter	0.47 - 1.23, $\Delta = 0.084$	

Table 4.1: Used temperature profiles and water vapor content according to the three standard atmospheres. N_W indicates the number of considered atmospheric models according to changed water vapor content. Δ is the step width.

For each of these then obtained different atmospheric states, urban, rural, and tropospheric **boundary layer types of aerosols** for several visibilities are considered (Table 4.2 and Fig. 4.1).

BL-aerosol type	visibility	number
rural	15 – 35 <i>km</i> , $\Delta = 5$ <i>km</i>	$N_A = 11$
urban	5 – 25 <i>km</i> , $\Delta = 5$ <i>km</i>	
tropospheric	50 <i>km</i>	

Table 4.2: Included boundary layer aerosol types. N_A indicates the number of considered atmospheric models according to aerosols. Δ is the step width.

According to the BIRD mission objectives containing the detection of HTE, e.g. volcanic activities, **volcanic aerosols** as well as the possible existence of **cirrus clouds** are included (Table 4.3). Due to the consideration of cloud free conditions with or without volcanic aerosols the number of atmospheric models according to volcanic aerosols is $N_{VA} = 2$.

altitude of cirrus	geometric thickness of cirrus	number
6 <i>km</i>	0.2, 0.5, 0.9 <i>km</i>	$N_C = 6$
10 <i>km</i>		

Table 4.3: Considered cirrus models. N_C indicates the number of considered atmospheric models according to cirrus clouds.

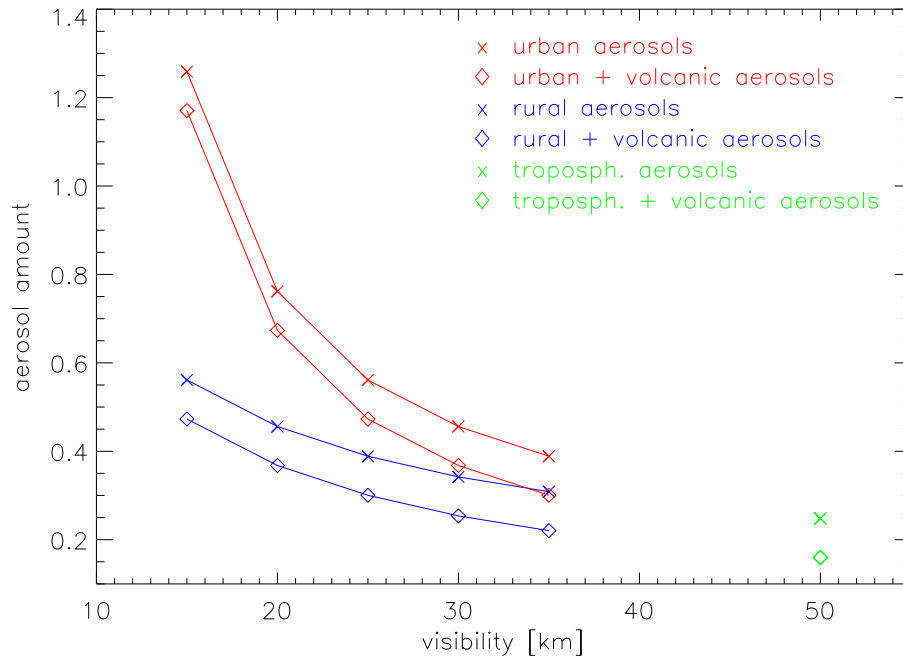


Figure 4.1: Aerosol amount and visibility. Aerosol amount corresponds to the total vertical aerosol optical depth at 550 nm (nadir view) (Shettle, 2000)

The **daytime data set** is generated as a function of the solar zenith angle. The results presented throughout this chapter are related to a sun zenith angle of 30° . This condition is given during the summer months at mid latitudinal regions when remote sensing measurements are most likely performed.

The signal at the TOA is determined by the atmospheric conditions and the ground radiance which is a coupled information of the surface temperature and the emissivity. For the method investigations the ground altitude is assumed to be the sea level.

The **surface temperature** varies within a range from 268 to 313 K in steps of 1 K adapted to the standard atmospheres ($N_T = 46$).

The **emissivity of land surfaces** may vary between 0.85 and 0.99 due to soil structure, soil composition, organic matter, moisture content, vegetation cover characteristics, and season as well as wavelength (de Griend & Owe, 1993; Ottlé & Stoll, 1993; Salisbury & D’Aria, 1992a; Salisbury & D’Aria, 1992b; Sutherland & Bartholic, 1977). According to BIRD’s mission objectives five emissivity classes ($N_\epsilon = 5$), *blackbody* (reference surface), *water/vegetation*, *bare soil*, *forest*, and *urban areas* (concrete, asphalt) have been investigated (Fig. 4.4). Therefore, not the entire emissivity variability and all possible combinations of the MIR and TIR emissivities have been explored. The surface type *vegetation* covers a large range of emissivity values from 0.93 to 0.98 . Areas covered with grass or grain fields are generally chosen for remote sensing validation experiments. These both surface types show high emissivity as well as lake water and were put together into one emissivity class called *water/vegetation*. The surface type *arid (desert) bare soil* is not included according to BIRD’s mission objectives.

surface	ε_1	ε_2
<i>blackbody</i>	1.00	1.00
<i>wat-veg</i>	0.98	0.98
<i>urban</i>	0.94	0.96
<i>bare soil</i>	0.93	0.95
<i>forest</i>	0.84	0.85

Table 4.4: Included surface types (*wat-veg*: water or vegetation) and its spectral emissivity. ε_1 and ε_2 indicates the MIR and TIR channel, respectively (Salisbury & D’Aria, 1992a; Salisbury & D’Aria, 1992b; Berk et al., 1989).

Taking all combinations of called atmospheric ($N_W \times N_A \times (N_C + N_{VA})$) and surface states ($N_T \times N_\varepsilon$) into account the entire mid latitude data set consists of 1.012.000 coupled atmospheric and surface models. The high number of models is an essential condition for the application of a statistical method in terms of a bi-spectral regression for the temperature retrieval.

4.2 Method

Published results have been shown (Coll et al., 1994) that applying the same method used on water surfaces followed by an additional correction to account for the emissivity is an appropriate way for an atmospheric correction of land surface thermal images. A similar emissivity correction was first presented in a master thesis by (Lippert, 1995). The “Regression” - Approach is explained on the case of nighttime conditions. The results are discussed for simulated day- and nighttime data.

4.2.1 Bi-spectral Linear Regression

At-sensor radiances for BIRD’s MIR and TIR channels were simulated for the entire data set described in the section before according to the following radiative transfer equation. All occurred quantities are channel-integrated. In their calculation the response functions of the IR sensors were considered (Chapter 2). Due to a Lambertian surface is assumed, the directional hemispheric ϱ_{h_i} and bidirectional reflectivity ϱ_{b_i} can directly be related to $(1 - \varepsilon_i)$. BIRD will measure in nadir direction thus the view and azimuth angles are equal to zero.

$$L_i^{toa} = B_i(T_i) = \varepsilon_i B_i(T_S) \tilde{\tau}_i + \underbrace{L_i^{atm\uparrow} + (1 - \varepsilon_i) L_i^{atm\downarrow} \tau_i + (1 - \varepsilon_i) \tau_i^{sun} \frac{E_i^{sun}}{\pi} \cos \theta_s \tau_i}_{MODTRAN} \quad (4.1)$$

with i index that indicates integrated values for the channels
 $i = 1, 2$ (MIR, TIR)
 L_i^{toa} TOA radiance
 $B_i(T_i)$ blackbody radiance of the brightness temperature T_i
corresponding to the TOA radiance L_i^{toa}

$B_i(T_S)$	blackbody radiance of the surface temperature T_S
ε_i	surface emissivity
$\tilde{\tau}_i$	effective transmittance (see below)
τ_i	atmospheric transmittance
$L_i^{atm\uparrow}$	upwelling atmospheric radiance (solar diffuse and thermal)
$L_i^{atm\downarrow}$	downwelling atmospheric radiance (solar diffuse and thermal)
E_i^{sun}	extraterrestrial solar irradiance already corrected for the Earth-Sun distance
θ_s	solar zenith angle
τ_i^{sun}	transmittance in solar incidence direction

Note, that the solar reflected and diffuse radiances are negligible within the TIR channel and the definition of $L_i^{atm\downarrow}$ is given in Chapter 3.

The so-called effective atmospheric transmittance $\tilde{\tau}_i$ was derived from

$$L_{B,i}(T_S) \approx \varepsilon_i B_i(T_S) \tau_i \quad (4.2)$$

assuming that the land surface emittance is almost constant across the band width of each channel. The transposition of the latter equation to the transmission τ_i and the setting of the surface temperature T_S to 300 K which is called ‘‘MODTRAN-Run-Temperature’’ (*MRT*) lead to the effective transmittance $\tilde{\tau}_i$.

$$\tilde{\tau}_i = \frac{L_{B,i}(T_S = MRT)}{\varepsilon_i B_i(T_S = MRT)} \quad (4.3)$$

It has been shown that the error for a temperature range from ~ 260 K to ~ 320 K applying the effective transmittance lies in a 0.01 % - range (Lippert, 1995). It turned out that the used effective transmittance has the same properties as the real atmospheric transmission function (independent on surface properties) but is more practical for time consuming model calculations.

In order to consider uncertainties of the radiative transfer simulations using MODTRAN random noise is included in the simulated at-sensor radiance. An appropriate noise according to a Gaussian function of 1 % of the TOA radiance was chosen.

The measured TOA radiance L_i^{toa} can be related to a radiometric temperature T_i according to the Planck function (Chapter 3, Eq. (3.6)). Utilizing these two brightness temperatures T_i a linear regression approach is likely to apply for the estimation of surface temperatures T_S^{**} assuming the land surface emissivity were unity and constant within both channels.

$$\text{method}_A : \quad T_S^{**} = a_0 + a_1 T_1 + a_2 T_2 \quad (4.4)$$

Since the water vapor is a main absorber in the infrared the inclusion of its information could lead to a decrease of the retrieval errors.

$$\text{method}_B : \quad T_S^{**} = a_0 + a_1 T_1 + a_2 T_2 + a_3 W \quad (4.5)$$

The parameter W describes the total atmospheric water vapor amount in g/cm^2 . The parameters a_0, a_1, a_2, a_3 are the regression coefficients.

Assuming that the user of the described regression algorithm has some information on the humidity of the atmosphere and the surface temperature range the entire data set was split up into four subsets according to these quantities, where each of them has N_j , $j=1..4$ different surface and atmospheric states (Table 4.5 and 4.6). The range of the quantities was adapted to common meteorological conditions in mid latitude regions. The *AP-index* (A Priori information index) indicates the type of the a priori information and is employed for the identification of the used subsets. If the AP-index is set to *non* all atmospheric and surface models of the entire mid latitude data set were considered in the simulation (no division into subsets).

subset j			
1	2	3	4
cold		warm	
dry	wet	dry	wet

Table 4.5: Characterization of the subset number j

AP-index	atmospheric a priori information	W [g/cm^2]
AD	dry	0.47 - 2.71
AW	wet	1.61 - 4.79
AP-index	surface a priori information	T_S [K]
SC	cold	268 - 293
SW	warm	283 - 313

Table 4.6: Subset intervals according to the water vapor amount W and surface temperature T_S

As can be seen from error tables, e.g. Table 4.7, the a priori knowledge and an overlap in the transitional ranges of the meteorological quantities decrease the temperature retrieval errors.

The results of applying both regression methods to the *blackbody* data set consisting of 202.400 coupled atmospheric and surface models using nighttime simulated data as an example are summarized in Table 4.7. For comparing reasons the results of `methodB` using daytime simulated data are additionally included in this table. The used simulated BIRD data set covers a large variety of naturally occurring atmospheric and surface conditions featuring a very dense step width of the parameters which have been varied. A monotonic and steady dependence of the temperature retrieval error on the parameters investigated has been observed. Therefore, the creation of an independent atmospheric data set for the estimation of the retrieval error is not expected to change the results significantly and has thus not been done.

Throughout this chapter, the root mean square (rms) $\Delta_j^{1.0}T_S^{**}$ and the maximum $\Delta_j^{1.0}T_S^{**max}$ temperature retrieval errors are defined as

$$\Delta_j^{1.0}T_S^{**} = \sqrt{\frac{\sum_{k=1}^{N_j} (T_{S_k}^{**} - T_{S_k})^2}{N_j}} \quad (4.6)$$

$$\Delta_j^{1.0}T_S^{**max} = \max[|(T_S^{**} - T_S)|] \quad (4.7)$$

The index 1.0 denotes that the retrieval errors were achieved using the regression coefficients for a *blackbody* data set ($\varepsilon_i = 1.0$). N_j indicates the number of considered coupled atmospheric and surface models.

AP-Index	N_j	$\Delta_j^{1.0}T_S^{**} [K]$		
		nighttime		daytime
		method _A	method _B	
SC-AD	55978	1.69	1.33	1.54
SC-AW	57382	1.55	1.50	1.85
SW-AD	66743	1.15	0.67	0.85
SW-AW	68417	1.25	0.83	0.98
non	202400	1.78	1.38	1.59

Table 4.7: Mean (rms) temperature retrieval errors $\Delta_j^{1.0}T_S^{**} [K]$ for a *blackbody* data set ($\varepsilon_i = 1.0$) applying method_A or method_B using night- or daytime simulated data

The mean (rms) temperature retrieval errors applying method_A or method_B using nighttime simulated data are similar. But in general, it can be seen that the inclusion of the atmospheric water vapor amount as a third source of information in the regression decreases the temperature retrieval errors. Thus, further investigations on the regression approach were focused on method_B. In the following the method type corresponding to method_B is not explicitly mentioned.

The used regression coefficient for a *blackbody* data set applying method_B are to be found in Appendix A (Tables A.1 and A.2).

The temperature retrieval distribution for the *blackbody* data set related to the surface temperature is displayed in Figure 4.2 applying method_B and utilizing nighttime simulated data. The figure for daytime simulated data is given in Appendix A. The largest temperature retrieval errors are in the cold surface temperature range. The reason is the difficulty to distinguish between the contributions of the atmosphere and

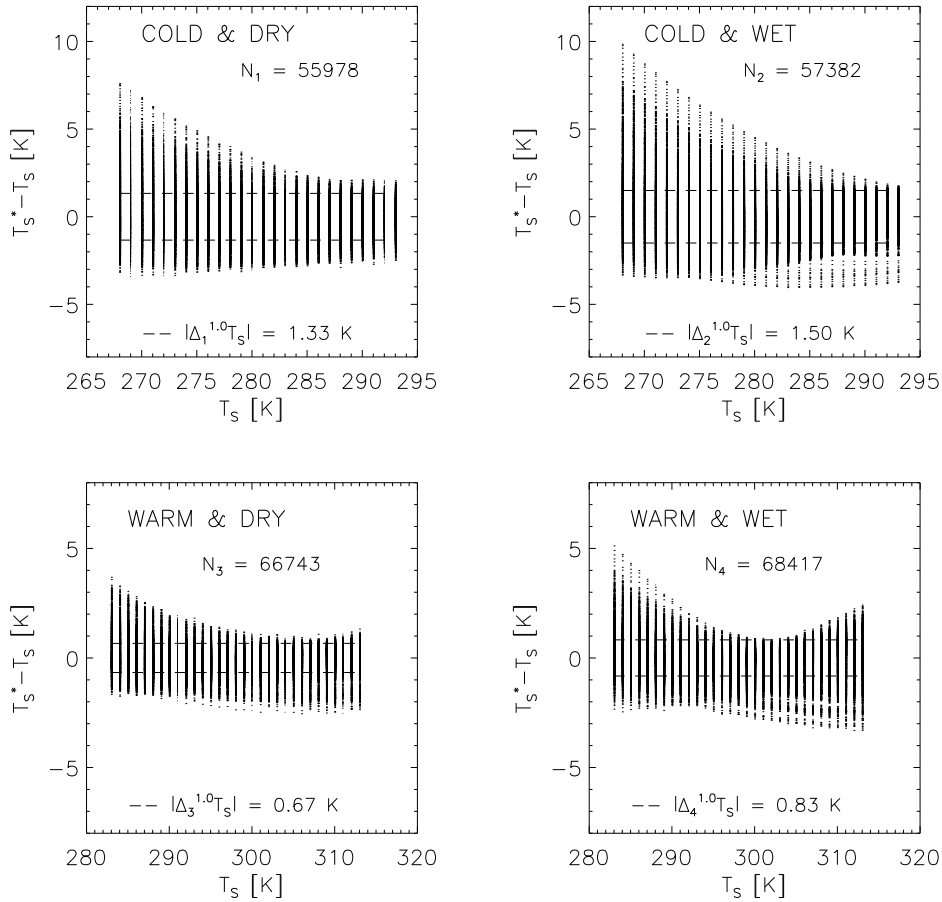


Figure 4.2: Temperature retrieval errors ($T_S^* - T_S$) versus true surface temperatures (T_S) utilizing the *blackbody* data set and simulated nighttime data with $|\Delta_j T_S| = \pm \Delta_j^{1.0} T_S$ (method_B). Note, that $T_S^{**} = T_S^*$ for the *blackbody* data set since no emissivity correction is needed.

the surface since their temperatures are similar. The information on surface temperatures included in the emitted ground radiance on its way through the atmosphere to the satellite sensor is almost completely covered by the atmospheric radiative contribution. Therefore, the quality of a correlation between the at-sensor brightness temperatures and the original surface temperature found by a regression method is less than for higher surface temperatures.

4.2.2 Emissivity Correction

In the last subsection the results of the bi-spectral regression method applied on the *blackbody* data set were presented. Land surfaces cannot be regarded as blackbodies due to their surface composition expressed in an emissivity value of less than 1.0. The investigation of a regression coefficient database for all possible combinations of MIR

and TIR emissivity values characterizing a naturally occurred surface type would be very time consuming and ineffective. Thus, a way of exploring an emissivity correction consisting of two steps was chosen. For a certain land surface character as e.g. *bare soil* the emissivity correction has to be employed after applying the bi-spectral regression utilizing the coefficients for a *blackbody* data set. The “blackbody regression” underestimates the surface temperature for land surfaces with an emissivity below one. This fact results in the following main question for an emissivity correction:

*How does the derived surface temperature T_S^{**} change if the emissivity varies, but the signal at the sensor (the integrated radiance at TOA) should be constant?*

In the **first step of the emissivity correction** a temperature correction dT_S^{**} has been computed. It is based on the linear dependence between the integrated radiance in the spectral region from $8.5 \mu\text{m}$ to $9.3 \mu\text{m}$ (TIR range) and the emissivity for an arbitrary grey body.

Considering the three radiative transfer terms within the TIR channel, the radiance emitted from the ground surface and attenuated by the atmosphere ($\varepsilon_2 B_2(T_S) \tilde{\tau}_2$), the downwelling atmospheric radiance reflected by the surface ($(1 - \varepsilon_2) L_2^{atm\downarrow}$) and the upwelling pathradiance emitted by the atmospheric constituents ($L_2^{atm\uparrow}$), in regard to the dependence on the emissivity, only the emitted ground radiance is important. $L_2^{atm\uparrow}$ is not a function of the emissivity and the reflected downwelling radiance is only dependent on $(1 - \varepsilon_2)$, thus its impact is negligible against the impact of the emitted ground radiance.

In the spectral region from $8.5 \mu\text{m}$ to $9.3 \mu\text{m}$ the emitted integrated radiance for a *blackbody* can be described by the following weakly nonlinear equation (Eq. 4.8).

$$B_2^*(T_S^{**}) = b_0 + b_1 T_S^{**} + b_2 T_S^{**2} \quad (4.8)$$

where the coefficients have the value $b_0 = 43.8$, $b_1 = 0.4$ and $b_2 = 0.0009$. Therefore, the TOA radiance emitted from the ground surface and attenuated by the atmosphere can be written as

$$L_{B_2} = \varepsilon_2 \underbrace{(b_0 + b_1 T_S^{**} + b_2 T_S^{**2})}_{B_2^*(T_S^{**})} \tilde{\tau}_2 \quad (4.9)$$

The formation of the total differential of L_{B_2} , its zero-setting and an inversion to T_S^{**} leads to the necessary first surface temperature correction.

$$dT_S^{**} = - \frac{(b_0 + b_1 T_S^{**} + b_2 T_S^{**2}) d\varepsilon^*}{(b_1 + 2b_2 T_S^{**}) \varepsilon^*} \quad (4.10)$$

$$\text{with } d\varepsilon^* = \varepsilon_2 - \varepsilon^*, \quad \varepsilon_2 < 1, \quad \varepsilon^* = 1.0$$

After this approach an error distribution near zero will not be achieved. An offset T_0^{**} exists for every true temperature in each subset. The reason is the coarse first emissivity correction and the neglect of the downwelling atmospheric radiance reflected by the surface $(1 - \varepsilon_2) L_2^{atm\downarrow}$. In Figure 4.3, the temperature retrieval errors after applying the first emissivity correction are plotted using the data set for the emissivity class *water/vegetation* as an example.

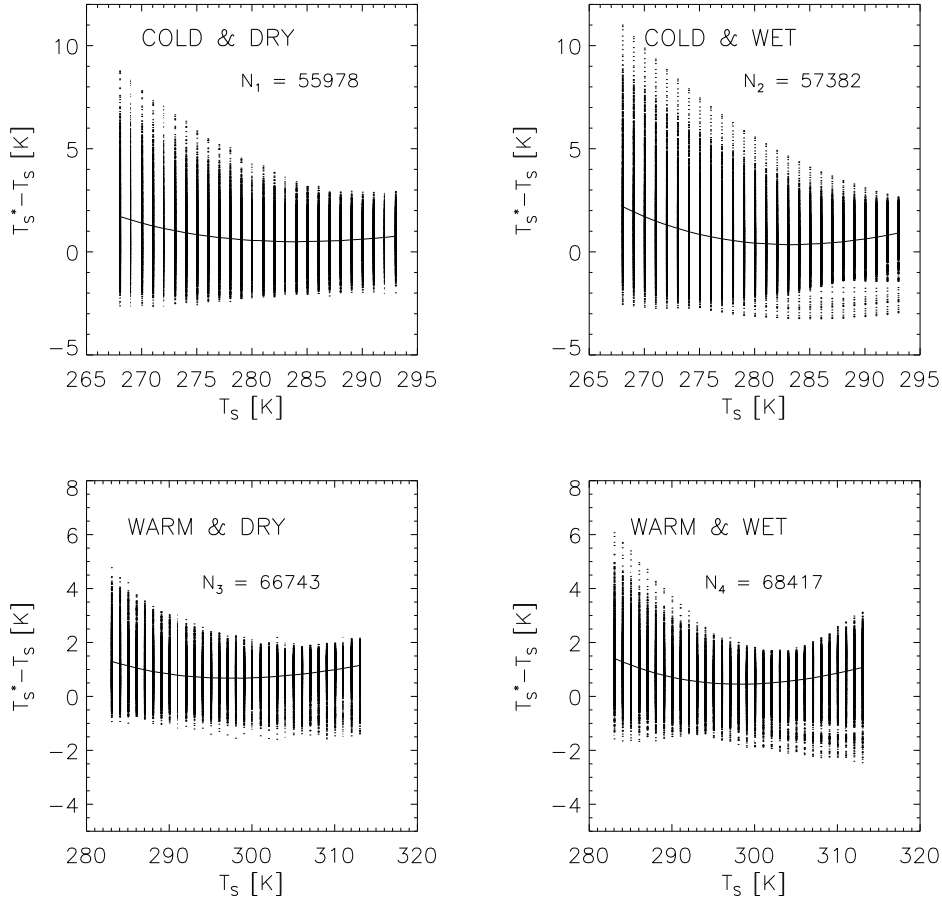


Figure 4.3: Temperature retrieval errors ($T_s^* - T_s$) versus true surface temperatures (T_s) after applying the first emissivity correction ($T_s^* = T_s^{**} + dT_s^{**}$) utilizing the *water/vegetation* data set and simulated nighttime data

Thus, the **second step of the emissivity correction** is the adjustment of the offset-function for every subset by a *3rd* order polynomial. Figure 4.3 shows the “offset-problem” where a solid curve denotes T_0^{**} . The parameter j indicates the subset number.

$$T_0^{**} = c_{0,j} + c_{1,j}(T_S^{**} - 280) + c_{2,j}(T_S^{**} - 280)^2 + c_{3,j}(T_S^{**} - 280)^3 \quad \text{for } j = 1, 2 \quad (4.11)$$

$$T_0^{**} = c_{0,j} + c_{1,j}(T_S^{**} - 300) + c_{2,j}(T_S^{**} - 300)^2 + c_{3,j}(T_S^{**} - 300)^3 \quad \text{for } j = 3, 4 \quad (4.12)$$

$c_{l,j}$ with $l = 0, \dots, 3$ denotes the fitting coefficients.

Now, the estimated land surface temperature T_s^* will be retrieved by applying the following equation:

$$T_s^* = T_s^{**} + dT_s^{**} - T_0^{**} \quad (4.13)$$

An extensive verification on the emissivity correction was presented in (Lippert, 1995).

4.3 Results

In Table 4.8 the results for the mean (rms) and maximum temperature retrieval errors for nighttime conditions after applying the entire temperature retrieval algorithm on the data set “mid latitude” containing the subsets according to land surface types *water/vegetation*, *bare soil*, *urban* and *forest* are shown. The given range of the errors is attributed to the different emissivity classes. For most cases the maximum errors correspond to the surface type *forest* and the minimum to *wat-veg*. That means, surfaces with high emissivity will have smaller temperature retrieval errors as surfaces with lower emissivity.

Assuming that the user of the described regression algorithm has some information on the humidity of the atmosphere and the surface temperature range the whole data set was split up into four coarse subsets according to these quantities. The a priori knowledge and the overlap in the transitional ranges of the meteorological quantities avoid a decrease in the temperature retrieval error. The elimination of extreme atmospheric states like “thick cirrus” results in smaller errors too. Including these states is definitely necessary for the estimation of realistic temperature retrieval errors.

The mean (rms) $\Delta_j^{1.0}T_S$ and maximum $\Delta_j^{1.0}T_{S_{max}}$ temperature retrieval errors are defined in the same way as in Equation (4.6) and (4.7) only $T_{S_k}^{**}$ and T_S^{**} are replaced by $T_{S_k}^*$ and T_S^* , respectively.

AP-Index	retrieval errors [K]			
	mid latitude data set		without thick cirrus and urban aerosols	
	$\Delta_j^{1.0}T_S$	$\Delta_j^{1.0}T_{S_{max}}$	$\Delta_j^{1.0}T_S$	$\Delta_j^{1.0}T_{S_{max}}$
SC-AD	1.43 - 1.87	8.06 - 10.76	1.18 - 1.72	5.49 - 8.50
SC-AW	1.62 - 2.21	10.52 - 14.10	1.09 - 1.55	5.79 - 7.96
SW-AD	0.67 - 1.21	3.83 - 4.70	0.58 - 0.98	3.43 - 4.50
SW-AW	0.81 - 1.35	5.29 - 8.21	0.49 - 0.86	3.03 - 5.20

Table 4.8: Temperature retrieval errors after applying the entire algorithm considering the mid latitude data set and using simulated nighttime data

The distribution of the temperature retrieval error utilizing simulated nighttime data and the *water/vegetation* data set is expressed in Figure 4.4. The figures for the other emissivity classes are provided in Appendix A.

In Figure 4.4, T_S is the true surface temperature and N_j with $j = 1..4$ is the total number of different atmospheric and surface related states included into the statistical data subset. The largest temperature retrieval errors again appear in the cold surface

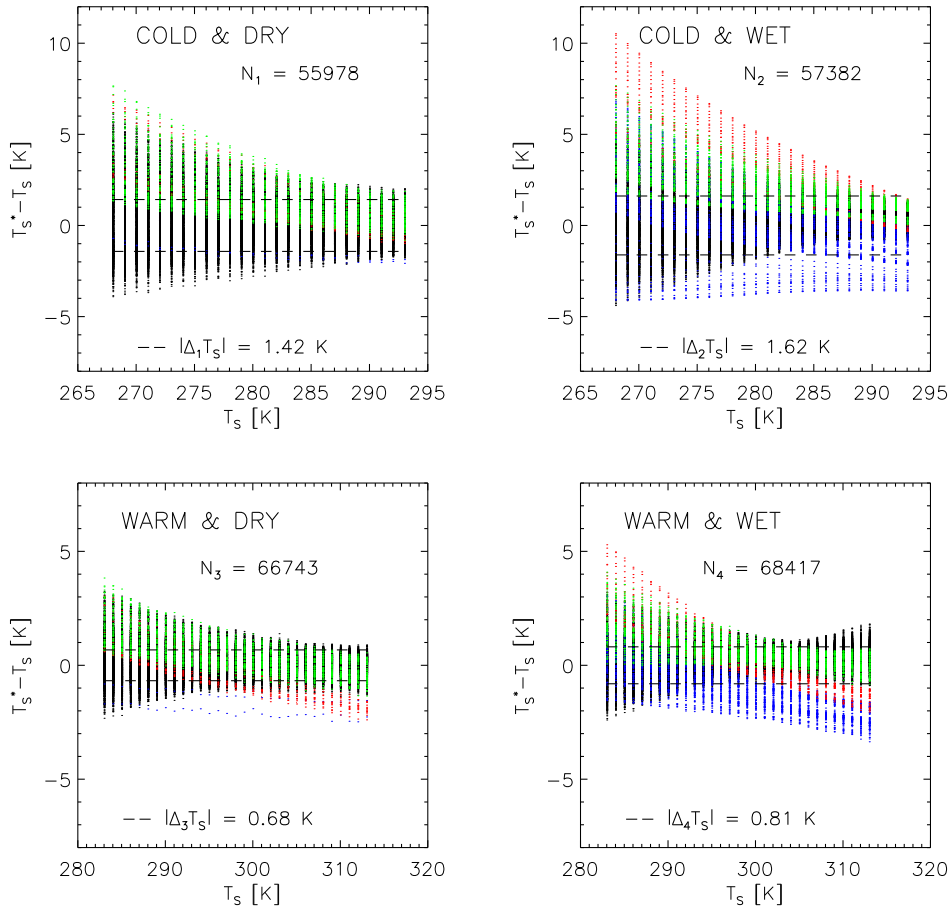


Figure 4.4: Temperature retrieval errors ($T_S^* - T_S$) versus true surface temperatures (T_S) after applying the entire algorithm utilizing the *water/vegetation* data set and simulated nighttime data with $|\Delta_j T_S| = \pm \Delta_j^{1.0} T_S$

temperature range due to the predominant atmospheric influence in case of cold surface temperatures (see previous Subsection 4.2.1). The subset ranges according to the surface temperature and the humidity were carefully chosen to get realistic combinations of surface and atmospheric models. Nevertheless, some quite unnatural coupling are included especially in the subset *SC – AW*, e.g. $T_S = 260 K$ and $W = 4.19 g/cm^2$. The highest maximum errors are to be explained by such models. As to be expected the smallest errors occur within the region around the MODTRAN run temperature of $300 K$ (see Eq. 4.3). The colors point out the different contribution of extreme atmospheric condition to the error distribution.

“Thick” cirrus and volcanic aerosols are mainly responsible for the large (maximum) temperature retrieval errors. Their extinctive properties induce a low atmospheric transmittance as seen in Figure 4.6 and strongly influence the ground radiation containing the information on the surface temperature. In that case it is more difficult to find a qualified correlation between the true and estimated surface temperature apply-

color	atmospheric condition	aerosol content aer
blue	“thick” cirrus, urban aerosol	$aer > 1.0$
red	no cirrus, volcanic aerosol	$0.5 < aer < 1.0$
green	no cirrus, volcanic & urban aerosol	$aer < 0.5$

Table 4.9: Included “extreme” atmospheric conditions. aer is given in MU which is the MODTRAN unit for the aerosol content and corresponds to the total vertical aerosol optical depth at 550 nm (nadir view) (Shettle, 2000).

ing a linear regression method. The temperature retrieval error distribution reflects the interference of the discussed errors and their sources. The distribution of the frequency of all occurred temperature retrieval errors show a Gaussian behavior (e.g. Fig. 4.5). Thus, the application of the proposed bi-spectral linear regression on the chosen mid latitude data set is justified.

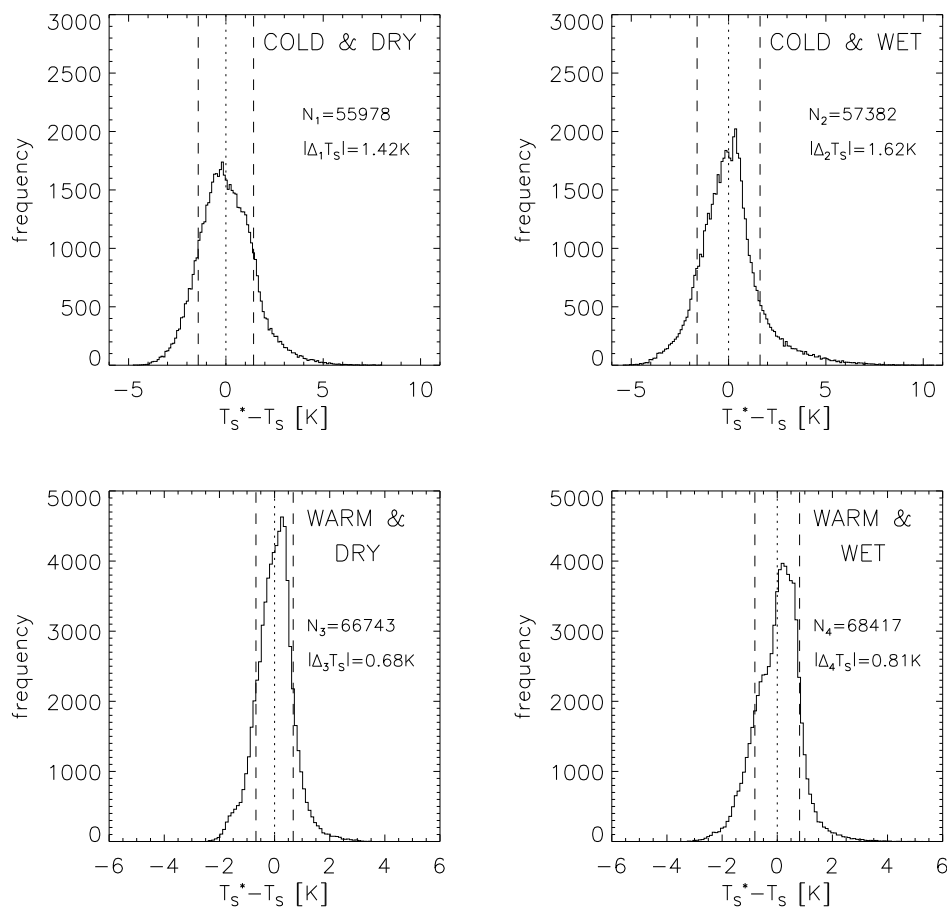


Figure 4.5: Frequency distribution of occurred temperature retrieval errors ($T_S^* - T_S$) versus true surface temperatures (T_S) after applying the entire algorithm utilizing the *water/vegetation* data set and simulated nighttime data with $|\Delta_j T_S| = \pm \Delta_j^{1.0} T_S$

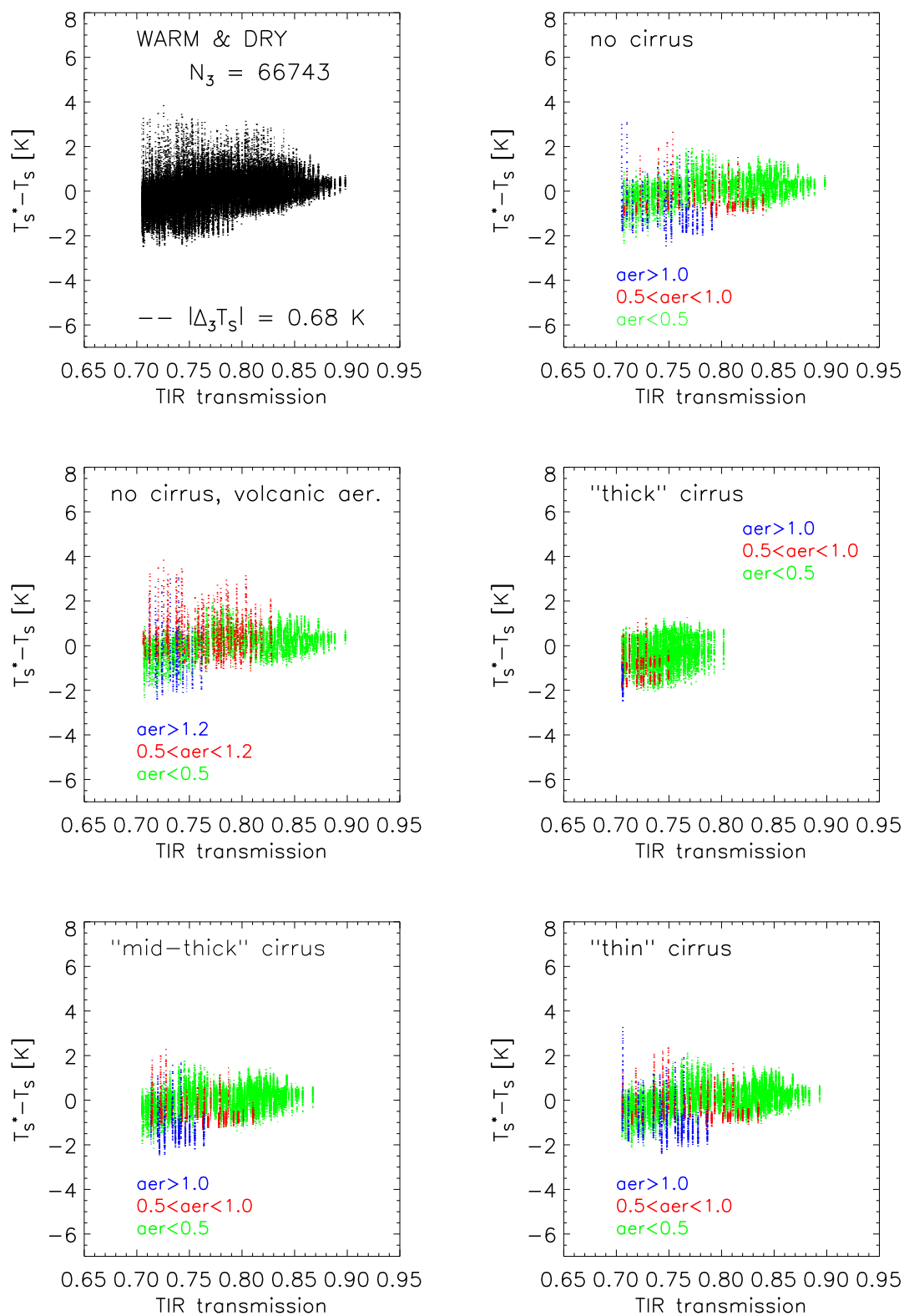


Figure 4.6: Temperature retrieval errors ($T_s^* - T_s$) versus TIR transmission after applying the entire algorithm utilizing the *water/vegetation* data set (subset warm/dry) and simulated nighttime data

Unfortunately, the proposed method and emissivity correction only works for high emissivity values (emissivity class: *water/vegetation*) during nighttime because under **daytime conditions** the sensor signal is additionally contaminated by the solar radiation within the mid infrared range. In this spectral range the thermal and solar radiation are of the same order of magnitude. The reason for unsatisfied retrieval errors is that the regression considers the MIR and TIR information but the emissivity correction is focused on the thermal infrared radiation. From the radiative transfer equation can be seen that for smaller emissivities the solar radiative contribution gets more influence on the total radiation. Results for the emissivity classes *water/vegetation* and *bare soil* as examples utilizing the regression method with and without emissivity correction and daytime simulated data are summarized in Table 4.10.

emissivity class	data set for regression coefficient	mean (rms) retrieval errors [K]			
		subsets			
		SC-AD	SW-AD	SC-AW	SW-AW
<i>wat-veg</i>	<i>blackbody</i>	1.96	2.40	1.49	1.43
	<i>wat-veg</i>	1.73	2.10	1.17	1.30
<i>bare soil</i>	<i>blackbody</i>	5.12	6.71	6.74	4.91
	<i>bare soil</i>	1.74	2.58	1.91	2.18

Table 4.10: Temperature retrieval errors after applying the entire algorithm with or without emissivity correction utilizing *water/vegetation* or *bare soil* data sets as well as simulated daytime data

The retrieval errors using *blackbody* regression coefficients and applying the emissivity correction are not acceptable for vegetation exploration under daytime conditions. Applying a regression on the data sets of the exemplary chosen surface types (*water/vegetation, bare soil ...*) lead to smaller retrieval errors but the usage of the investigated regression coefficients are strongly restricted on the chosen (input) emissivity. It is impossible to provide a database of regression coefficients for all possibly naturally occurred combinations of MIR and TIR emissivities. Finally, the application of the “Regression” - Approach during daytime is not recommended. Instead, the TISIE - Approach presented in the next chapter should be used for the retrieval of surface temperatures using daytime measurements.

Chapter 5

“TISIE” - Approach

The basic problem of land surface temperature retrieval is that the ground radiance includes coupled information on the emissivity and the surface temperature. In this chapter a method is proposed for retrieving land surface emissivity as well as temperature separately without a priori information on these quantities. A similar model applied on AVHRR data was first mentioned by Goita & Royer (Goita & Royer, 1997). The retrieval technique utilizes the ground radiances measured in the MIR and TIR channel of BIRD. An atmospheric correction has to be applied before starting the retrieval algorithm. The main issue of the model is the usage of the TIR brightness temperature derived from the TIR ground radiance for the estimation of the MIR emissivity. Due to the emissivity differences between both channels a correction factor called TISIE (Temperature Independent Spectral Index for Emissivity) has to be introduced. Knowing the mid infrared emissivity, the surface temperature and the emissivity in the TIR channel can be recovered. In the next sections the investigations on the “TISIE” - Approach are explained in detail.

5.1 Surface and Atmospheric Models

A synthetic data set of surface and atmospheric models was generated for the derivation of the “TISIE” - Approach which is partly based on a statistical method. Thermal at-ground and at-sensor (TOA) radiances were simulated applying the radiative transfer model MODTRAN3.5 (Berk et al., 1989) and the spectral characteristic of BIRD’s IR-sensors (Section 2.2).

The **atmospheric model** is set up by MODTRAN’s standard atmospheres (tropical, mid latitude summer, mid latitude winter, US-standard) assuming rural aerosols with a visibility of 23 km as a typical example. According to BIRD’s measurement geometry the view zenith angle and the relative azimuth angle are set equal to zero. The values $\theta_s = 0^\circ, 15^\circ, 30^\circ, 45^\circ, 60^\circ$ were chosen for the sun zenith angle.

The **surface conditions** are an assortment of emissivity extracted from the Salisbury & D’Aria database (Salisbury & D’Aria, 1992a; Salisbury & D’Aria, 1994). Surface

temperatures were taken out of the range from 250 K to 350 K in steps of 0.1 K. The used emissivity classes and their channel-integrated emissivity values of the samples are summarized in Table 5.1. The channel-integrated emissivity ε_i of each sample was calculated as

$$\varepsilon_i = \frac{\int_{\nu_1}^{\nu_2} f_{r_i}(\nu) \varepsilon_\nu d\nu}{\int_{\nu_1}^{\nu_2} f_{r_i}(\nu) d\nu} \quad (5.1)$$

with i channel index: 1 = MIR, 2 = TIR
 ν wavenumber in [cm^{-1}]
 ε_ν spectral emissivity for the wavenumber ν
 f_{r_i} spectral response function of the infrared channel i

emissivity classes	emissivity samples	emissivity range	
		ε_1	ε_2
meteorites	60	0.88 - 0.99	0.97 - 0.99
soils	43	0.68 - 0.93	0.81 - 0.98
metamorphic rocks	38	0.57 - 0.96	0.72 - 0.96
igneous rocks	36	0.84 - 0.97	0.66 - 0.98
sedimentary rocks	24	0.72 - 0.96	0.80 - 0.97
minerals	22	0.42 - 0.70	0.51 - 0.96
vegetation	9	0.84 - 0.99	0.96 - 0.99
water	3	0.96 - 0.98	0.98 - 0.99

Table 5.1: Emissivity database (Salisbury & D’Aria, 1992a; Salisbury & D’Aria, 1994)

One objective of the BIRD mission is the detection of natural hot spots such as volcanic activities. Therefore, the high number of rock samples in the emissivity database is reasonable. Almost all MIR emissivity values ε_1 lie in the range from 0.6 to 1.0. TIR emissivities ε_2 may exhibit low values for some bare rocks and dry bare soils in desert areas (silicates). Serious difficulties in handling BIRD data for these situations can be foreseen from the results presented in Chapter 4. In order to be consistent with consideration of BIRD main objectives, the values of TIR emissivity ε_2 were confined to the range from 0.94 to unity. Although this is somewhat arbitrary, this range encompasses most situations likely to be encountered. Note, the resulted MIR emissivity range is still quite large.

Realistic combinations of all surface and atmospheric models lead to an extensive data set allowing the application of statistical methods. The coupled surface and atmospheric models represent a variety of natural conditions. The information on them are combined in TOA radiances which are expected to be measured by BIRD’s sensors.

5.2 Method Description

As mentioned in the introduction chapter the retrieval of the surface temperature from airborne or satellite data consists of two main procedures, the atmospheric correction and the separation of the ground information in emissivity and surface temperature. The content of this section is focused on the separation problem. For the investigation of an approach it is always useful to prove its applicability under the assumption of Lambertian surfaces first.

The daytime MIR ground radiance for a Lambertian surface can be generally expressed as:

$$L_1^{grd} = B_1(T_{B,1}^{grd}) = \varepsilon_1 B_1(T_S) + (1 - \varepsilon_1) L_1^{atm\downarrow} + (1 - \varepsilon_1) \tau_1^{sun} \frac{E_1^{sun}}{\pi} \cos \theta_s \quad (5.2)$$

with	index $i = 1$	indicates integrated values for the MIR channel
	L_1^{grd}	ground radiance
	$B_1(T_{B,1}^{grd})$	blackbody radiance of the brightness temperature $T_{B,1}^{grd}$ corresponding to the MIR ground radiance L_1^{grd}
	$B_1(T_S)$	blackbody radiance of the surface temperature T_S
	ε_1	surface emissivity
	θ_s	solar zenith angle
	$L_1^{atm\downarrow}$	downwelling atmospheric radiance
	E_1^{sun}	extraterrestrial solar irradiance already corrected for the variation of the Earth-Sun distance
	τ_1^{sun}	transmittance in solar incidence direction

The TIR ground radiance equation mainly consists of two radiative transfer terms because the solar reflection contribution is negligibly small against the other radiation parts.

$$L_2^{grd} = B_2(T_{B,2}^{grd}) = \varepsilon_2 B_2(T_S) + (1 - \varepsilon_2) L_2^{atm\downarrow} \quad (5.3)$$

Equation (3.1) in Chapter 3 is a combined version of Equation (5.2) and (5.3) additionally containing the atmospheric contribution itself. As can be seen from the equations the problem is underestimated: we have three unknown surface parameters ($\varepsilon_1, \varepsilon_2, T_S$) but only two equations according to the number of BIRDS infrared channels. This problem is tackled by introducing a factor $TISIE = \varepsilon_1/\varepsilon_2$. In a regression procedure TISIE is linearly approximated, depending on the ratio of ground radiances. The regression is based on $\varepsilon_1, \varepsilon_2$ -combinations taken from the Salisbury database. Once TISIE is known from the ground radiances, the number of independent variables is reduced to two. Now, the equation system can be solved.

In order to get an impression of the orders of magnitude, the ground radiances and their brightness temperatures in the MIR and TIR channel as well as the corresponding surface temperatures for four standard atmospheres coupled to a soil surface are opposed as an example in Figures 5.1 and 5.2. Although the combination of a mid latitude winter atmospheres and a sun zenith angle of 45° is quite unrealistic this case is nevertheless included in the figures for comparing reasons.

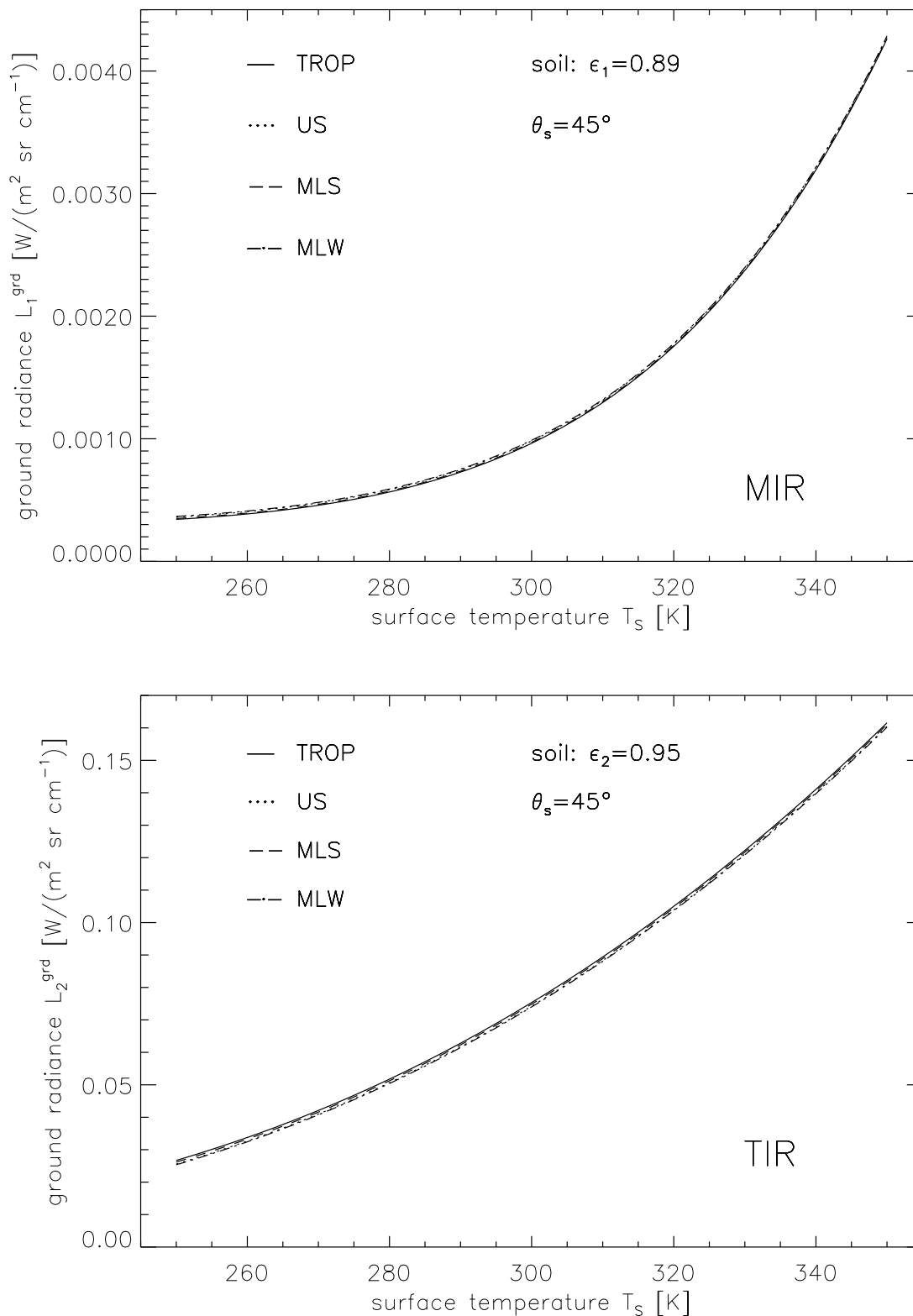


Figure 5.1: Ground radiances in the MIR and TIR channels and the corresponding surface temperatures for four standard atmospheres coupled to a soil surface (angles: $\theta_s = 45^\circ$, $\theta_v = 0^\circ$)

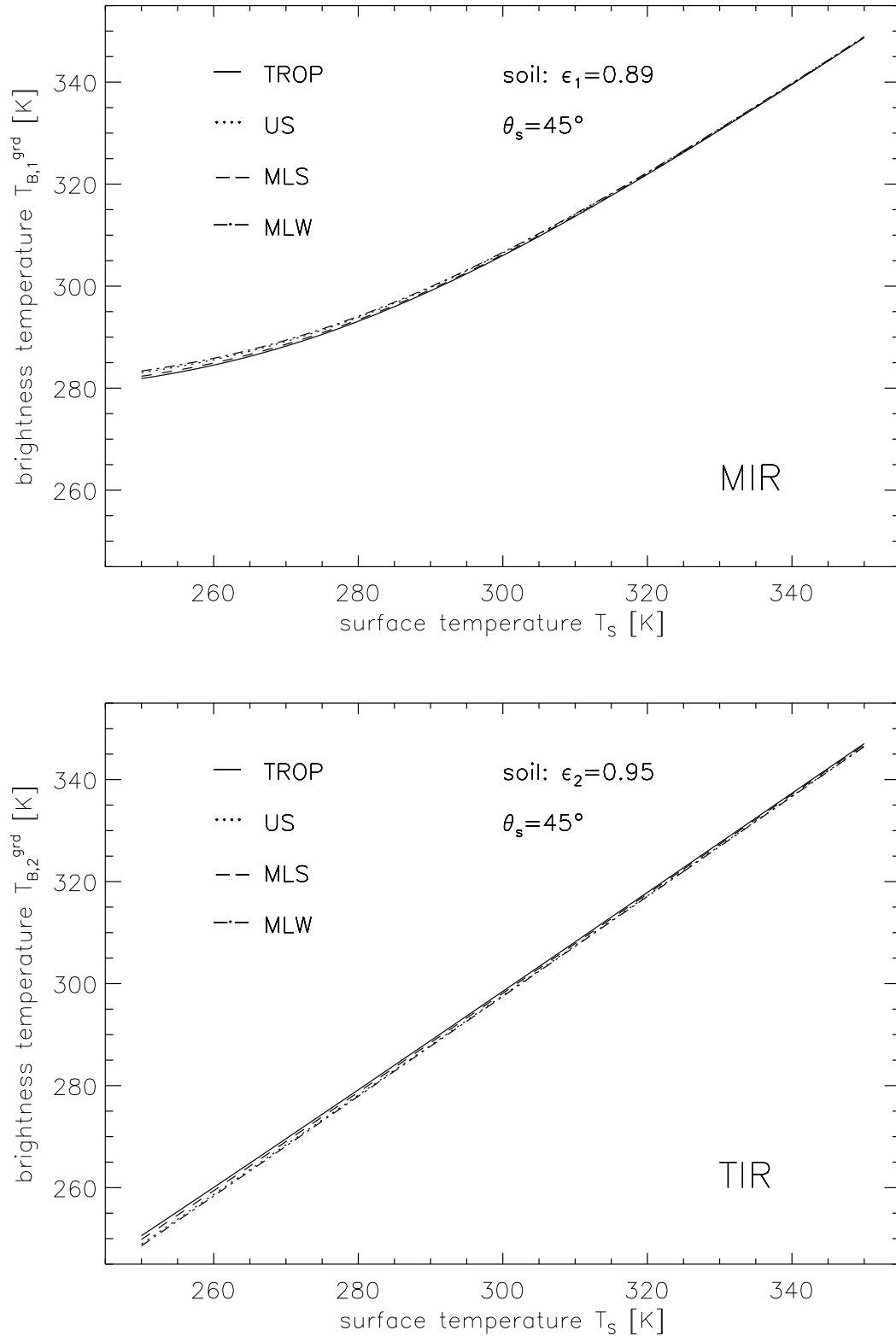


Figure 5.2: Brightness temperatures according to ground radiances in the MIR and TIR channels and the corresponding surface temperatures for four standard atmospheres coupled to a soil surface (angles: $\theta_s = 45^\circ$, $\theta_v = 0^\circ$)

On the next pages the retrieval equations for the surface emissivities ε_i^* and the surface temperature T_S^* are derived. Separating Equation (5.2) for the MIR emissivity ε_1 requires an assumption on the surface temperature T_S . The applied method utilizes the TIR at-ground brightness temperature $T_{B,2}^{grd}$ for the estimation of the thermal contribution ($\varepsilon_1 B_1(T_S)$) to the MIR at-ground radiance L_1^{grd} . From the replacing of $B_1(T_S)$ by $B_1(T_{B,2}^{grd})$ follows that a correction factor has to be introduced to account for the emissivities differences between the MIR and TIR channels. This factor can be derived as follows. The radiance of the surface emission in the channel i is described by

$$L_{S_i} = B_i(T_{B,i}^S) = \varepsilon_i B_i(T_S) \quad (5.4)$$

The integrated Planck radiance can be approximated for both IR channels of BIRD by a simple power function

$$B_i^*(T_S) = \alpha_i T_S^{n_i} \quad (5.5)$$

The parameters α_i, n_i were determined by a non-linear least square fit for the temperature range from 250 K to 350 K in steps of 0.1 K for each channel i . The fitting procedure is available as IDL - code called “curvfit.pro” (RSI, 1999). Using one set of (α_i, n_i) over the entire temperature range only is not enough to get the highest accuracy on the channel radiance. Some discrepancies are mainly to be observed at the lower temperature side. Figures 5.3 and 5.4 are essentially given for illustration purpose. As will be seen later (see Eq. (5.27), (5.28)), the coefficients, α_i and n_i , will actually appear in combinations that will be determined by direct fitting to the appropriate radiance ratio. Hence, full accuracy is recovered.

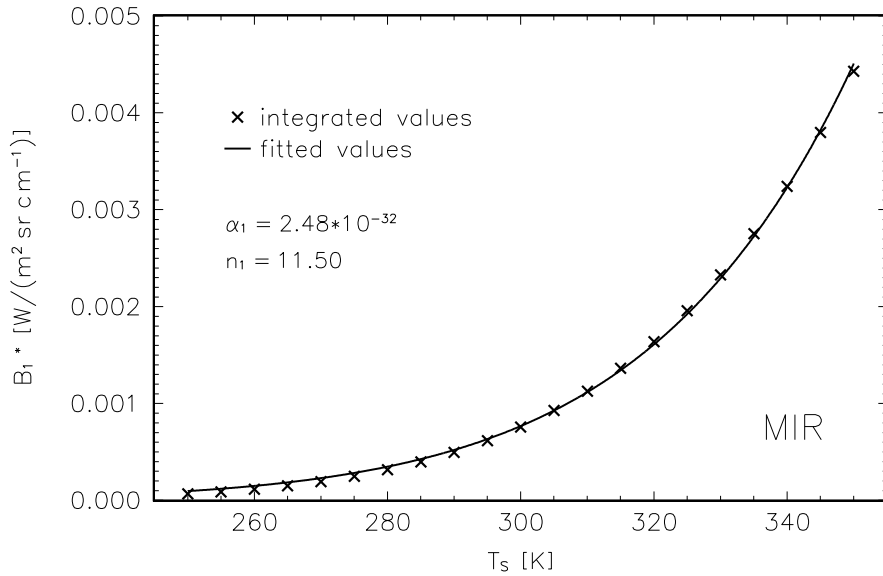


Figure 5.3: Non-linear least square fit for the Planck function integrated over wavenumbers and normalized by the MIR channel width

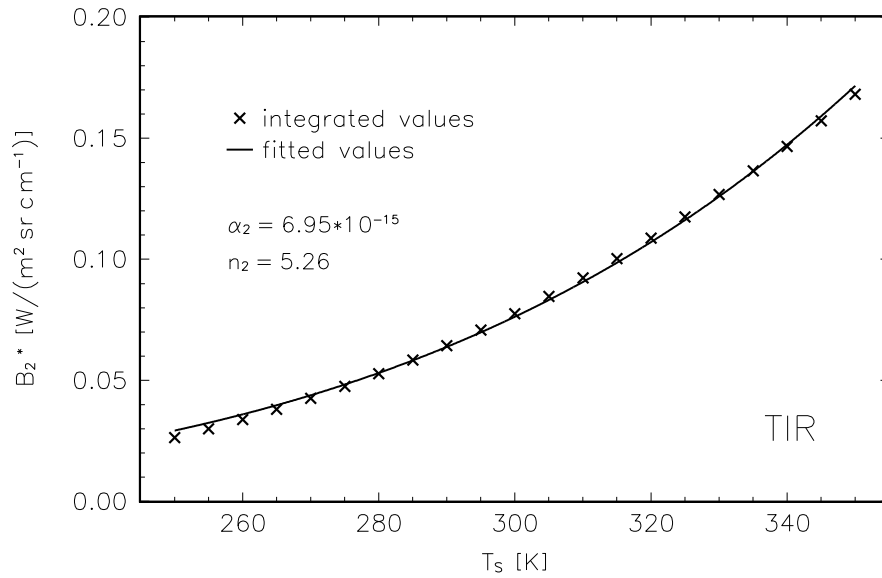


Figure 5.4: Non-linear least square fit for the Planck function integrated over wavenumbers and normalized by the TIR channel width

Introducing the fitted Planck function $B_1^*(T_S)$ (Eq. (5.5)) in Equation (5.4) the emitted MIR radiance of the surface is rewritten as

$$L_{S_1} = B_1(T_{B,1}^S) = \varepsilon_1 \alpha_1 T_S^{n_1} \quad (5.6)$$

Multiplying both sides of the last equation with a powered TIR emissivity $\varepsilon_2^{n_{12}}$ where $n_{12} = n_1/n_2$ leads to the expression

$$\begin{aligned} L_{S_1} = B_1(T_{B,1}^S) &= \frac{\varepsilon_1}{\varepsilon_2^{n_{12}}} \alpha_1 \varepsilon_2^{n_{12}} T_S^{n_1} \\ &= \frac{\varepsilon_1}{\varepsilon_2^{n_{12}}} \alpha_1 (\varepsilon_2 T_S^{n_2})^{n_{12}} \end{aligned} \quad (5.7)$$

Assuming the reflected downwelling TIR radiance is negligibly small against the other radiative transfer terms Eq. (5.3) reduces to

$$L_2^{grd}(T_S, \varepsilon_2) = \varepsilon_2 B_2(T_S) \quad (5.8)$$

Considering the radiance L_2^{grd} as an integrated Planck radiance a temperature, called the brightness temperature $T_{B,2}$, can be assigned. Thus, the last equation can be rewritten as

$$B_2(T_{B,2}^{grd}) = \varepsilon_2 B_2(T_S) \quad (5.9)$$

Applying the simple power function according to Equation (5.5) the latter equation changes to

$$\alpha_2 (T_{B,2}^{grd})^{n_2} = \alpha_2 \varepsilon_2 T_S^{n_2} \quad (5.10)$$

Thus, the TIR brightness temperature $T_{B,2}^{grd}$ can be directly related to the surface temperature T_S

$$T_{B,2}^{grd^{n_2}} = \varepsilon_2 T_S^{n_2} \quad (5.11)$$

Using the latter equation the formula of the emitted MIR radiance at ground (Eq. (5.7)) changes to

$$B_1(T_{B,1}^S) = \frac{\varepsilon_1}{\varepsilon_2^{n_{12}}} \alpha_1 T_{B,2}^{grd^{n_1}} \quad (5.12)$$

The ratio $\varepsilon_1/\varepsilon_2^{n_{12}}$ is called TISIE (Temperature Independent Spectral Index for Emissivity). It was first defined and applied by Becker & Li (Becker & Li, 1990a; Li & Becker, 1993). Now, the assumption on the surface temperature is made ($T_S \approx T_{B,2}^{grd}$). Thus, the blackbody radiance for the MIR channel can be rewritten as

$$B_1(T_S) \approx B_1(T_{B,2}^{grd}) = B_1^*(T_{B,2}^{grd}) = \alpha_1 T_{B,2}^{grd^{n_1}} \quad (5.13)$$

where $B_1^*(T_{B,2}^{grd})$ is calculated as in Eq. (5.5) only T_S is replaced by $T_{B,2}^{grd}$. Inserting the equation above into Eq. (5.12) the emitted ground radiance in the MIR channel is simplified to

$$\begin{aligned} B_1(T_{B,1}^S) &= \underbrace{\frac{\varepsilon_1}{\varepsilon_2^{n_{12}}}}_{TISIE} \underbrace{\alpha_1 T_{B,2}^{grd^{n_1}}}_{B_1^*(T_{B,2}^{grd})} \\ B_1(T_{B,1}^S) &= TISIE B_1^*(T_{B,2}^{grd}) \end{aligned} \quad (5.14)$$

At this point TISIE is assumed to be known. The next section contains studies on the determination of the TISIE parameter. The replacement of $\varepsilon_1 B_1(T_S)$ by $B_1(T_{B,1}^S)$ (Eq. (5.14)) in Eq. (5.2) enables the derivation of the MIR emissivity ε_1^* :

$$\varepsilon_1^* = 1 - \frac{L_1^{grd} - TISIE B_1^*(T_{B,2}^{grd})}{\tau_1^{sun} \frac{E_1^{sun}}{\pi} \cos \theta_S + L_1^{atm\downarrow}} \quad (5.15)$$

The retrieved MIR emissivity ε_1^* is introduced in Equation (5.2) which is rearranged to

$$B_1(T_S^*) = \underbrace{\left(\frac{L_1^{grd} - (1 - \varepsilon_1^*) \left(\tau_1^{sun} \frac{E_1^{sun}}{\pi} \cos \theta_S + L_1^{atm\downarrow} \right)}{\varepsilon_1^*} \right)}_X \quad (5.16)$$

Now, T_S^* is estimated from a look-up-table containing temperatures out of the range from 250 K to 350 K and the corresponding radiances X . The radiances for the look-up-table were obtained by numerical integration over the Planck function within BIRD's MIR and TIR channels (see Section 2.1).

Finally, the TIR emissivity ε_2^* is recovered using the equation for the TIR ground radiance (Eq. (5.3)).

$$\varepsilon_2^* = \frac{L_2^{grd} - L_2^{atm\downarrow}}{B_2(T_S^*) - L_2^{atm\downarrow}} \quad (5.17)$$

The results and a retrieval error discussion of the presented theory, applied on the data set described in Section 5.1, are analyzed in Section 5.4.

5.3 TISIE Determination

In this section the explored emissivity and radiance ratios as well as the relation between both of them are summarized and discussed.

Becker & Li (Becker & Li, 1990a; Li & Becker, 1993) defined temperature independent quantities called TISI (Temperature Independent Spectral Index) and TISIE (Temperature Independent Spectral Index for Emissivity) for the separation problem of the emissivity and temperature information from infrared remote sensing data.

5.3.1 Temperature Independent Spectral Indices

For the optimization of the TISIE - Approach two emissivity ratios, $TISIE_a$ and $TISIE_b$, were parallel investigated. They are defined as

$$TISIE_a = \frac{\varepsilon_1}{\varepsilon_2} \quad (5.18)$$

$$TISIE_b = \frac{\varepsilon_1}{\varepsilon_2^{n_{12}}} \quad (5.19)$$

The indices a and b characterize the kind of the emissivity ratio. Although $TISIE_b$ is by definition a temperature independent parameter, $TISIE_a$ is not the “true” $TISIE$ according to the definition given by Becker & Li. Actually, $TISIE_a$ is not temperature independent (see Subsection 5.3.2). However, the symbol $TISIE$ is kept for symmetry and ease of handling.

The relation between emissivity and radiance ratios can be derived from the radiative transfer equations (Eq. (5.2), (5.3)). First, only the ground emission of the surface is considered. That is the case of nighttime measurements (indicated by index n in the following equations) assuming the reflected radiance is negligible. The ground emission in both IR channels of BIRD is given according to Equation (5.4) and (5.5) by

$$L_{1,n}^{grd} = B_1(T_{B,1}^{grd}) = \varepsilon_1 B_1(T_S) = \varepsilon_1 \alpha_1 T_S^{n_1} \quad (5.20)$$

$$L_{2,n}^{grd} = B_2(T_{B,2}^{grd}) = \varepsilon_2 B_2(T_S) = \varepsilon_2 \alpha_2 T_S^{n_2} \quad (5.21)$$

Thus, the emissivity can be expressed as

$$\varepsilon_1 = \frac{B_1(T_{B,1}^{grd})}{\alpha_1 T_S^{n_1}} \quad (5.22)$$

$$\varepsilon_2 = \frac{B_2(T_{B,2}^{grd})}{\alpha_2 T_S^{n_2}} \quad (5.23)$$

The ratio of ε_1 and $\varepsilon_2^{n_{12}}$ leads to

$$\frac{\varepsilon_1}{\varepsilon_2^{n_{12}}} = \frac{B_1(T_{B,1}^{grd})}{\alpha_1 T_S^{n_1}} \frac{(\alpha_2 T_S^{n_2})^{n_{12}}}{(B_2(T_{B,2}^{grd}))^{n_{12}}} \quad (5.24)$$

where the left and right sides of the equation are called $TISIE$ and $TISI_B$, respectively.

$$\underbrace{\frac{\varepsilon_1}{\varepsilon_2^{n_{12}}}}_{TISIE} = \frac{\alpha_2^{n_{12}}}{\alpha_1} \underbrace{\frac{B_1(T_{B,1}^{grd})}{(B_2(T_{B,2}^{grd}))^{n_{12}}}}_{TISI_B} \quad (5.25)$$

with

$$n_{12} = \frac{n_1}{n_2} \quad \text{and} \quad M = \frac{\alpha_2^{n_{12}}}{\alpha_1}$$

Hence, the radiance ratio $TISI_B$ is defined as

$$TISI_B = M \frac{B_1(T_{B,1}^{grd})}{(B_2(T_{B,2}^{grd}))^{n_{12}}} = M \frac{L_{1,n}^{grd}}{(L_{2,n}^{grd})^{n_{12}}} \quad (5.26)$$

and is equal to $TISIE$ for nighttime measurements. $B_i(T_{B,i}^{grd})$ is calculated for each sample of each emissivity class, for each surface temperature and for both channels. The non-linear least square fitting procedure “curvfit.pro” was again used to determine the parameters n_{12} and M . For the estimation of the parameters the ratio of the MIR and the powered TIR Planck function, $B_1(T_S)$ and $B_2(T_S)$ was calculated, respectively.

$$\frac{B_1(T_S)}{(B_2(T_S))^{n_{12}}} = \frac{\alpha_1 T_S^{n_1}}{\alpha_2^{n_{12}} (T_S^{n_2})^{n_{12}}} \quad (5.27)$$

The values, $n_{12} = 2.3$ and $M = 3.9$, were determined by minimizing the reformulation of Equation (5.27). The calculated values for $n_{12} \approx 2.1$ and $M \approx 4.1$ using α_i and n_i given in Figures 5.3 and 5.4 slightly differ from the fitted values due to uncertainties in numerical calculations (see explanation before Fig. 5.3).

$$\ln B_1(T_S) = n_{12} \ln B_2(T_S) - \ln M \quad (5.28)$$

In the least square fitting method 1000 pairs of surface temperatures and their corresponding Planck functions were included.

The radiance ratio $TISI_L$ is mentioned here as well for comparison. For daytime conditions all radiative transfer terms (that includes the solar contributions) in Equations (5.2) and (5.3) have to be considered. Applying the same mathematical procedure as for the derivation of $TISIE_B$ the radiance ratio $TISI_L$ is defined as

$$TISI_L = M \frac{L_1^{grd}}{\left(L_2^{grd}\right)^{n_{12}}} \quad (5.29)$$

The relation between $TISIE$ and $TISI_L$ is then given by

$$TISI_L = C_{12} TISIE \quad (5.30)$$

with

$$C_{12} = \frac{C_1}{C_2^{m_{12}}} \quad (5.31)$$

$$C_1 = 1 + \frac{(1 - \varepsilon_1)L_1^{atm\downarrow} + (1 - \varepsilon_1)\tau_1^{sun} \frac{E_1^{sun}}{\pi} \cos \theta_s}{\varepsilon_1 B_1(T_S)} \quad (5.32)$$

$$C_2 = 1 + \frac{(1 - \varepsilon_2)L_2^{atm\downarrow}}{\varepsilon_2 B_2(T_S)} \quad (5.33)$$

All ratios were calculated for 1000 surface temperatures out of the range from 250 K to 350 K and each sample of the emissivity database. The considered atmospheric and surface models were introduced in Section 5.1 .

Figure 5.5 shows the temperature independent quantities and radiance ratios defined above. The equivalence of $TISIE_b$ and $TISIE_B$ is obvious from Equation (5.25). The difference between $TISI_L$ and $TISIE_B$ is based on the influence of the solar reflected radiative contribution on the MIR ground radiance. The higher the surface temperature the more predominant is the surface emission. The same effect can be seen in the lower part of Figure 5.5. The difference between the ratio of TOA radiances (L_1^{toa}/L_2^{toa}) and the ratio of ground radiances (L_1^{grd}/L_2^{grd}) decreases with increasing surface temperature. The different extinctive behavior of the standard atmospheres is responsible for the variation of the ratios seen in the upper part of Figure 5.5.

5.3.2 Estimation of TISIE Using Linear Regression

In order to solve Equation (5.2) to retrieve the MIR emissivity it is desirable to determine the TISIE parameter by a model using measured BIRD data. A linear relation between the parameters $TISIE_{a,b}$ and the ratio of MIR and TIR ground radiances $L_1^{grd}/L_2^{grd} = B_1(T_{B,1}^{grd})/B_2(T_{B,2}^{grd})$ was observed using the entire data set. For a certain surface temperature within the range from 250 K to 350 K the relation can be described by a linear function which can be computed by a linear regression.

$$TISIE_{a,b} = I_{a,b} + S_{a,b} \frac{B_1(T_{B,1}^{grd})}{B_2(T_{B,2}^{grd})} \quad (5.34)$$

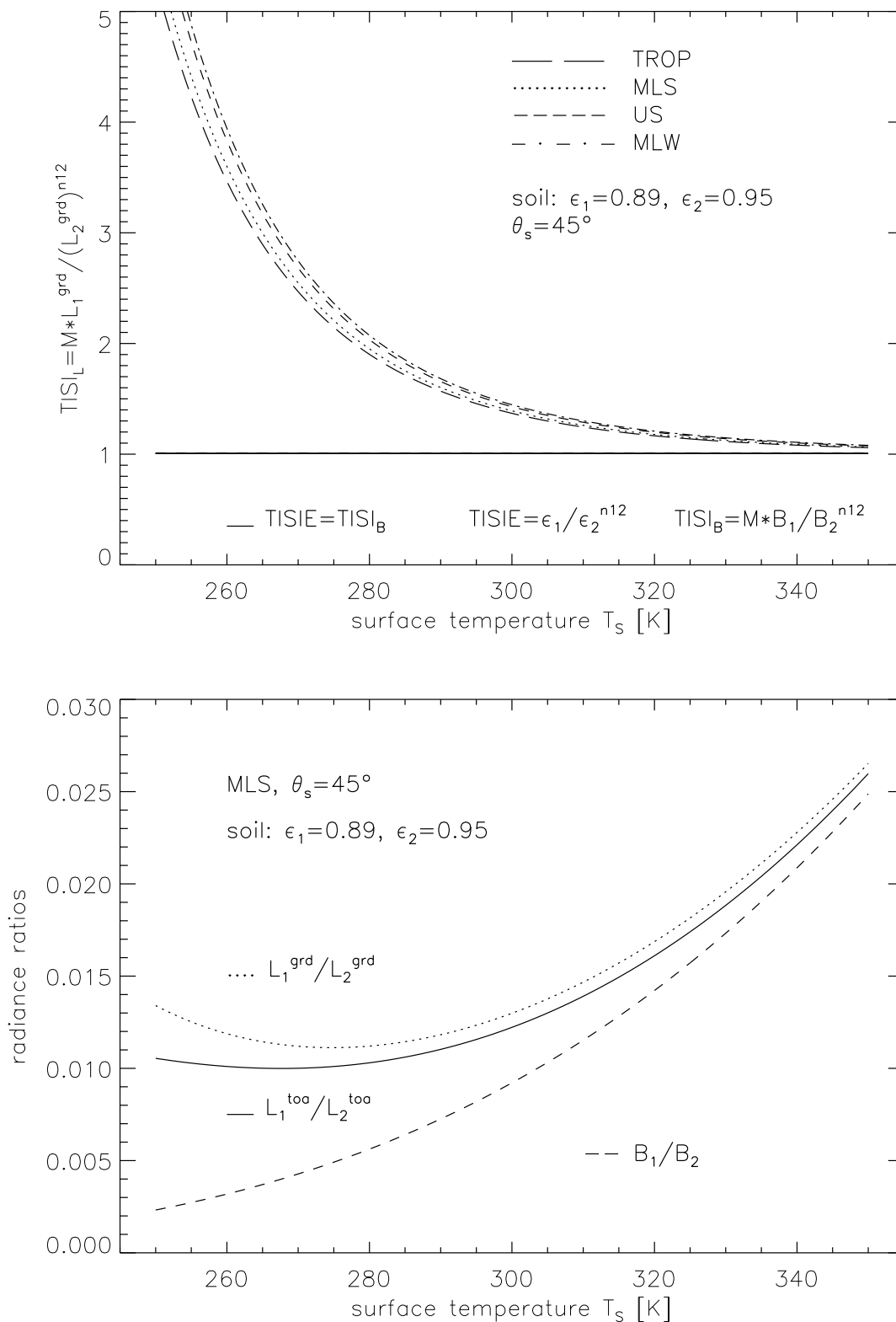


Figure 5.5: Several radiance ratios in relation to the surface temperature for a soil surface, different atmospheres and the angles, $\theta_s = 45^\circ$, $\theta_v = 0^\circ$

The regression coefficient $I_{a,b}$ (intercept) and $S_{a,b}$ (slope) are estimated for each standard atmosphere (TROP, MLS, MLW, US-ST) and sun angle ($\theta_s = 0^\circ, 15^\circ, 30^\circ, 45^\circ, 60^\circ$). The indices a and b refer to $TISIE_a$ and $TISIE_b$, respectively. A reduced emissivity database consisting of 114 samples was used for the investigations. A significant regression correlation coefficient ($R > 0.95$) was found for most coupled atmospheric and surface models using the parameter $TISIE_a$ (see tables in Appendix B). Utilizing $TISIE_a$ instead of $TISIE_b$ in the model (Eq. 5.15) is justified because the parameter n_{12} is around two and the TIR emissivity is greater than 0.94 (see Eq. 5.35).

$$\begin{aligned} TISIE_b &= \frac{\varepsilon_1}{\varepsilon_2^{n_{12}}} \\ &= \underbrace{\frac{\varepsilon_1}{\varepsilon_2}}_{TISIE_a} \underbrace{\frac{1}{\varepsilon_2}}_{1 \dots 1.06} \end{aligned} \quad (5.35)$$

Thus, $TISIE_a$, further simply called TISIE, was chosen to be used for ongoing investigations on this approach.

Figures 5.6 and 5.7 show as an example the regression model for several surface temperatures $T_S = 270, 300, 320 \text{ K}$, a sun zenith angle of $\theta_s = 45^\circ$ and a MLS atmosphere. The dependence of the coefficients for a $TISIE_a$ -regression on the surface and brightness temperature as well as on the sun zenith angle is displayed in Figure 5.8 sharing the same simulated conditions as explained in the previous sentence.

It would be an advantage if **no a priori information concerning the atmospheric conditions** were necessary for the estimation of TISIE. Investigations on including the entire data set for the TISIE regression were performed. It turned out that the relations between the emissivity and ground radiance ratios strongly depend on the surface temperature and the sun zenith angle as well as on the type of the atmosphere. The dependence of TISIE on the surface temperature can be approximately (neglecting the reflected terms) explained by the following equations.

$$TISIE = I + S \frac{L_1^{grd}}{L_2^{grd}} = I + S \frac{\varepsilon_1 \alpha_1 T_S^{n_1}}{\varepsilon_2 \alpha_2 T_S^{n_2}} = I + S \frac{\varepsilon_1 \alpha_1}{\varepsilon_2 \alpha_2} T_S^{n_1 - n_2} \quad (5.36)$$

$$\frac{\partial TISIE}{\partial T_S} = S \frac{\varepsilon_1 \alpha_1}{\varepsilon_2 \alpha_2} (n_1 - n_2) T_S^{n_1 - n_2 - 1} \quad (5.37)$$

Introducing the values $n_1 \approx 11.5$ and $n_2 \approx 5$ the derivation of $TISIE$ to the surface temperature T_S can be approximately written as.

$$\frac{\partial TISIE}{\partial T_S} \approx T_S^5 \quad (5.38)$$

Thus, the quality of the $TISIE$ determination using the described linear regression method approximately changes with the fifth power of surface temperature T_S .

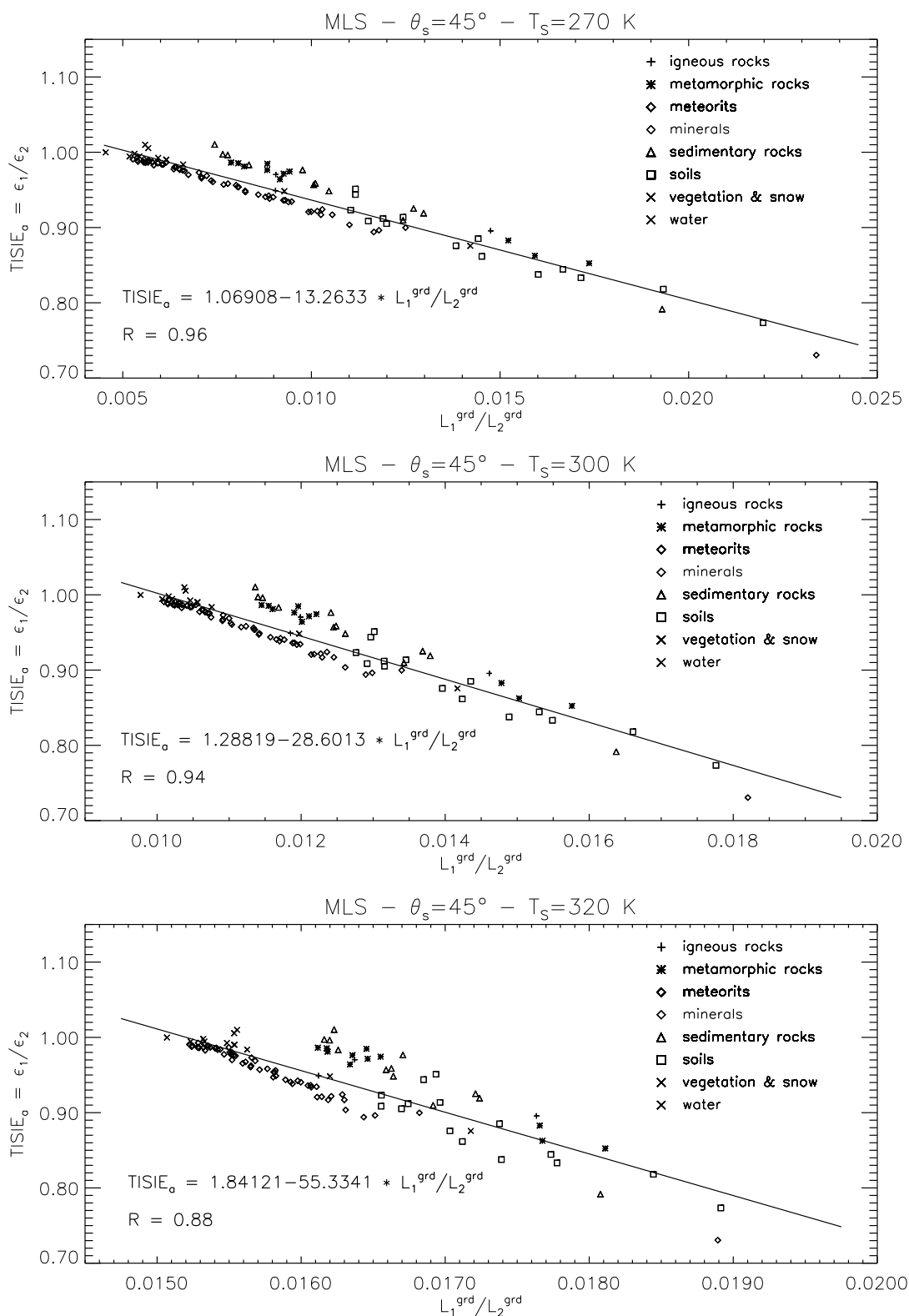


Figure 5.6: Relation between emissivity ratio ($TISIE_a$) and the ratio of ground radiances (Eq. (5.18), (5.34)) for several surface temperatures, mid latitude summer standard atmosphere and the angles, $\theta_s = 45^\circ$, $\theta_v = 0^\circ$. Solid lines correspond to a linear regression model. R is the correlation coefficient.

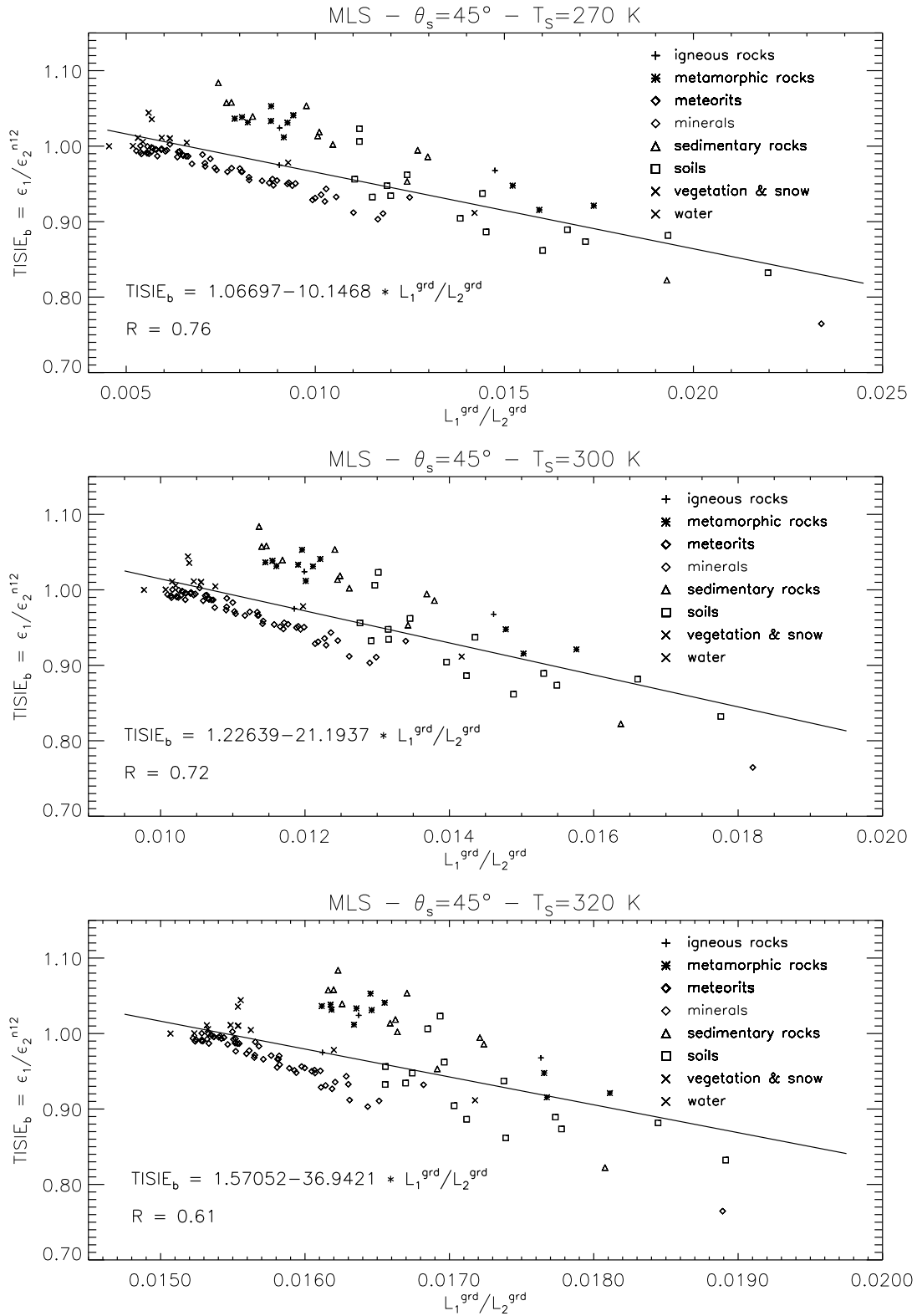


Figure 5.7: Same as Figure 5.6 but the emissivity ratio is $TISIE_b$ (Eq. (5.19))

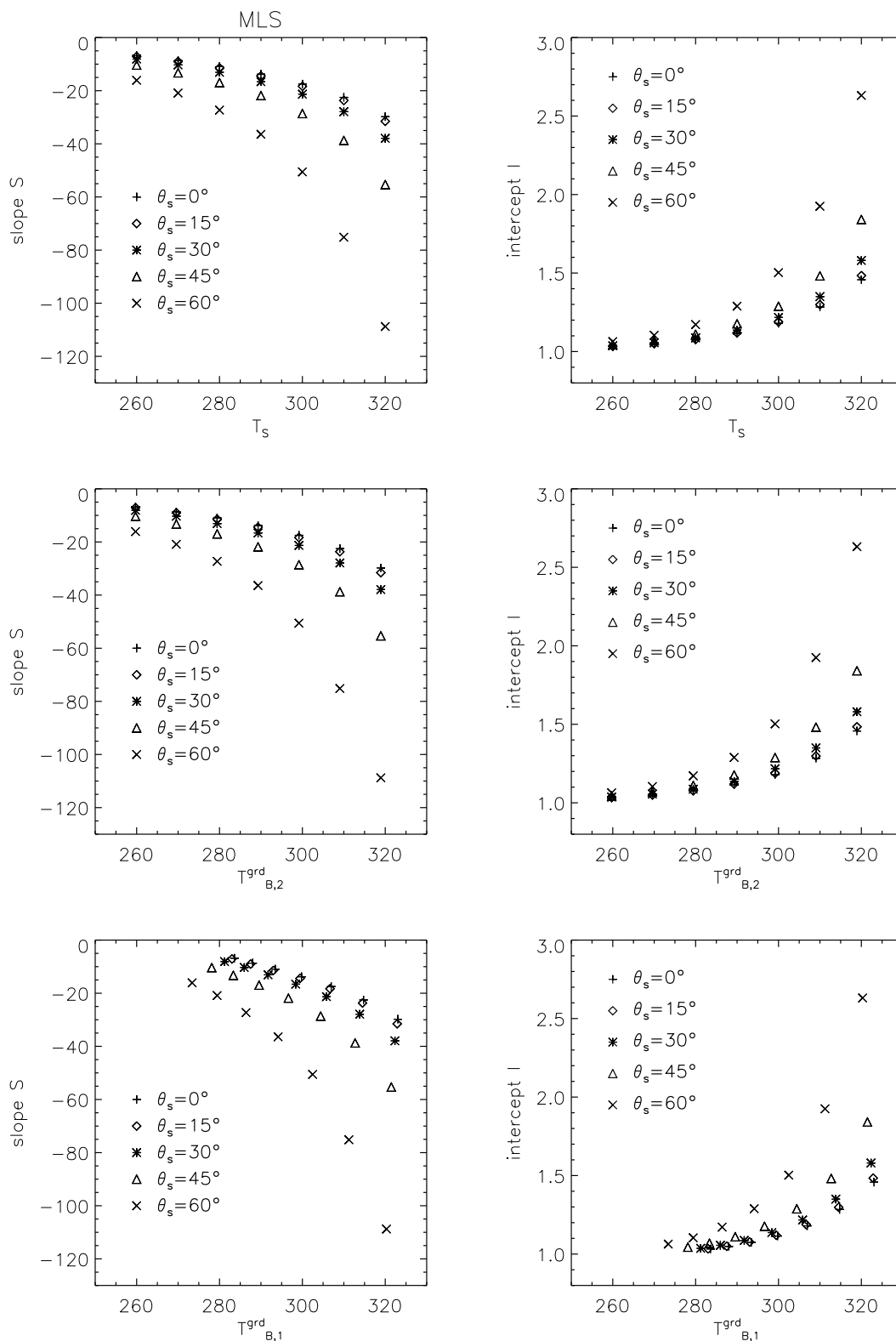


Figure 5.8: Variation of the regression parameters for $TISIE_a$ (Eq. (5.18), (5.34)) with the surface temperature T_s and the brightness temperatures at ground $T_{B,1}^{grd}$, $T_{B,2}^{grd}$ for a mid latitude summer standard atmosphere

In Figure 5.9 and 5.10 all coupled surface and atmospheric models are included. From these figures can be seen that a determination of TISIE using a regression method subject to atmospheric states is useful and improves the quality of the regression (increase of the value of the regression correlation coefficients). Since one will have information on the sun zenith angle during the overpass of the satellite it is useful to divide the entire data set into data subsets according to the sun zenith angle and running the regression on these data subsets (see Fig. 5.10). The dependence on the surface temperature has to be kept for any TISIE regression model. For the application of the algorithm the surface temperature T_S is replaced by the TIR brightness temperature $T_{B,2}^{grd}$ which can be assumed to be almost equal to the surface temperature.

A study on using **simulated TOA data** for the determination of the TISIE parameter was done as well. The quality of the regression using TOA data was worse than of the regression using ground simulated data ($R_{toa\ data} \leq R_{ground\ data}$). For that reason and since the “TISIE” - Approach requires an atmospheric correction anyway (utilizes ground radiances L_i^{grd}) the usage of TOA data for the determination of TISIE will mainly improve the method retrieval errors of the “TISIE” - Approach. Thus, the results are not further discussed in this document. Regression coefficients and the corresponding plots for the study using TOA data are summarized in an internal DLR report (Lippert, 2000).

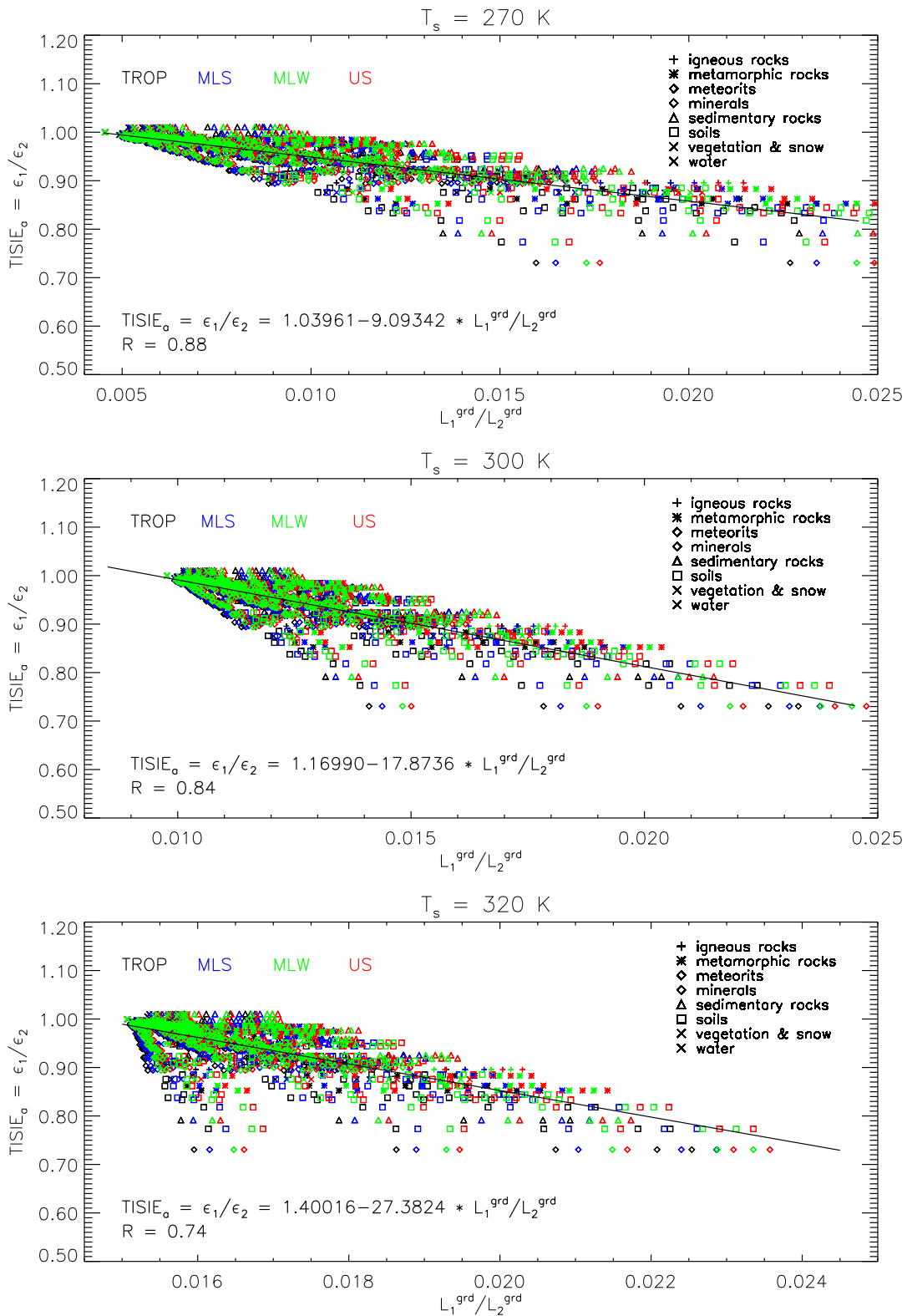


Figure 5.9: Relation between emissivity ratio ($TISIE_a$) and the ratio of ground radiances (Eq. (5.18), (5.34)) for the entire data set. Solid lines correspond to a linear regression model. R is the correlation coefficient.

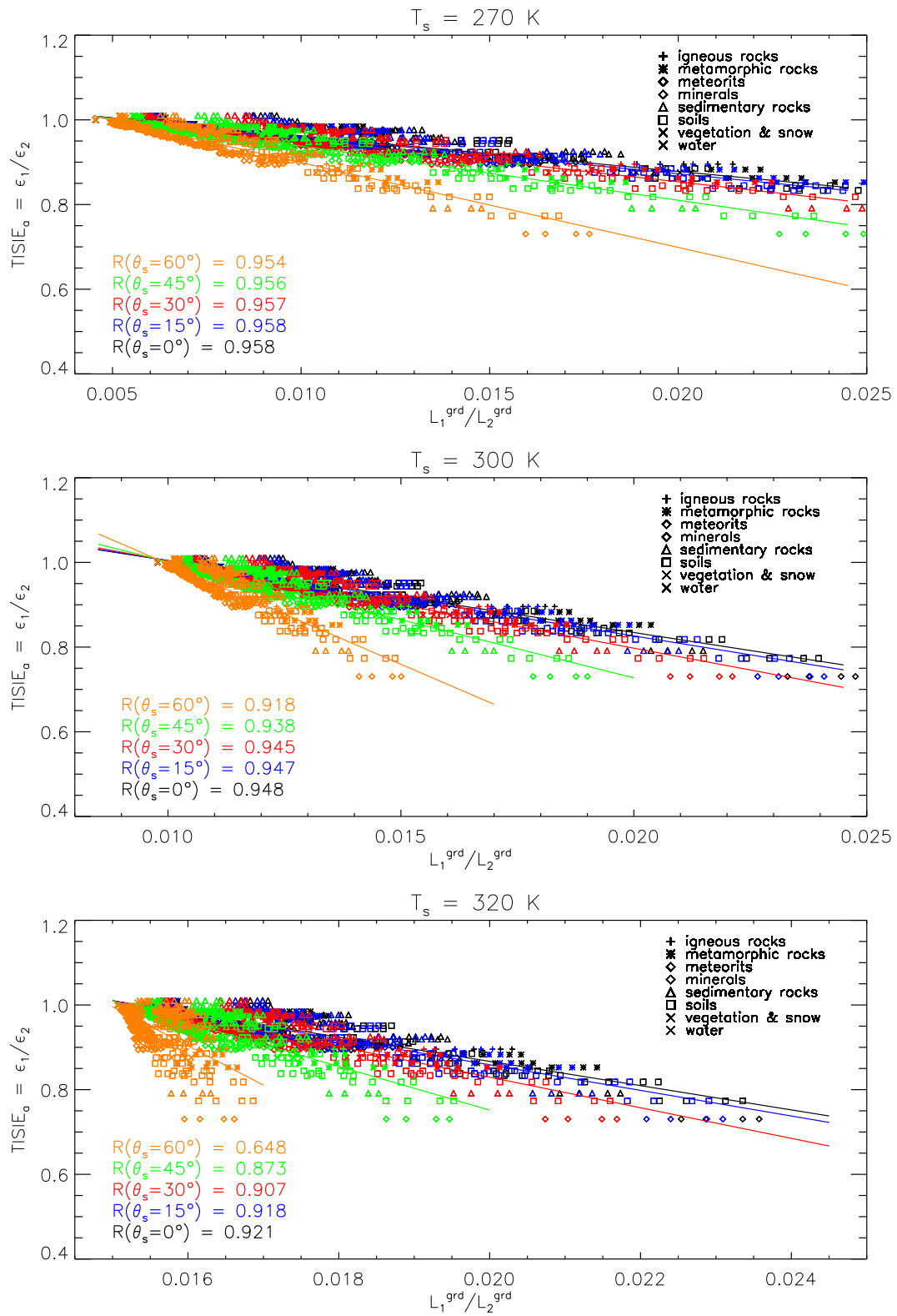


Figure 5.10: Same as Figure 5.9 but data set points are marked according to their sun zenith angles.

5.4 Results

In this section the results of the proposed emissivity and surface temperature separation method (“TISIE” - Approach) are discussed. The quality of the presented model is analyzed in terms of retrieval errors for the emissivity and the surface temperature. It has been distinguished between method retrieval errors (Subsection 5.4.1) and overall simulation errors (Subsection 5.4.2). The method retrieval errors express the quality of the methods itself whereas the uncertainty of the atmospheric correction is included in the calculation of the overall retrieval errors. An estimation of final errors considering all relevant error sources is given in Chapter 6.

Both error types, method and overall, are based on the comparison between the retrieved surface parameters (see Eq. (5.15), (5.16), (5.17)) and the corresponding input values of the simulation which are the coupled surface and atmospheric models described in Section 5.1. Thus, the data set contains four types of standard atmospheres, five sun zenith angles, 114 emissivity samples and 1000 surface temperatures. For the tropical region surface temperatures greater than 280 K are only considered. In the error plots only 100 surface temperatures are included in order to get a manageable size of the plots.

The parameter TISIE is estimated by the linear regression fit using the coefficient for $TISIE_a$ (Eq. (5.34)).

The root mean square and the maximum errors were computed according to Equations (5.39) and (5.40).

$$(\Delta Q)_{rms} = \sqrt{\frac{\sum_{j=1}^N (Q_j^* - Q_j)^2}{N - 1}} \quad (5.39)$$

$$(\Delta Q)_{max} = \max \left[|(Q_j^* - Q_j)_{j=1}^{j=N}| \right] \quad (5.40)$$

with rms root mean square error
 max maximum error
 $j = 1 \dots N$
 N number of considered data points
 Q_j true (input) value for $\varepsilon_1, \varepsilon_2, T_S$
 Q_j^* estimated value for $\varepsilon_1, \varepsilon_2, T_S$

5.4.1 Method Retrieval Errors

The method retrieval error quantifies the consistency of the developed approach. In Table 5.2 the mean (rms) and maximum errors are summarized considering the entire data set. Rms - errors between 0.006 and 0.02 for the mid infrared emissivity lead to temperature retrieval rms - errors around 0.6 K and rms - errors for the TIR emissivity

θ_s [°]	$(\Delta Q)_{rms}$			$(\Delta Q)_{max}$		
	$\Delta\varepsilon_1$	$\Delta\varepsilon_2$	ΔT_s [K]	$\Delta\varepsilon_1$	$\Delta\varepsilon_2$	ΔT_s [K]
0	0.0065	0.015	0.61	0.0391	0.066	2.21
15	0.0068	0.015	0.61	0.0410	0.066	2.19
30	0.0078	0.015	0.59	0.0476	0.066	2.13
45	0.0103	0.014	0.56	0.0643	0.065	2.04
60	0.0186	0.013	0.47	0.1170	0.064	1.86
all θ_s	0.0100	0.014	0.57	0.0618	0.065	2.09

Table 5.2: Method retrieval errors for MIR and TIR emissivity and surface temperature for different solar zenith angles θ_s , estimating TISIE by linear regression (Eq. (5.34)), considering the data set described in Section 5.1; $260 < T_S < 320$ K, except: $280 < T_S < 320$ K for tropical standard atmosphere

around 0.014. The maximum errors may arise up to 0.1 for the emissivity and around 2 K for the surface temperature. The error distribution is displayed in Figures 5.11, 5.12 and 5.13. The plots for the MIR emissivity show that the maximum errors occur at higher temperatures. The effect can be explained by the dependence of the calculated MIR emissivity ε_1 according to Equation (5.15) from the surface temperature T_S .

$$\varepsilon_1^* = 1 - \frac{L_1^{grd} - TISIE B_1^*(T_{B,2}^{grd})}{\tau_1^{sun} \frac{E_1^{sun}}{\pi} \cos \theta_S + L_1^{atm\downarrow}} \quad (5.41)$$

A coarse estimation of the error magnitude can be given by neglecting the reflected terms for the description of $L_1^{grd} = \varepsilon_1 B_1(T_S)$. Inserting the approximated integrated Planck function $B_1^*(T_S) = \alpha_1 T_S^{n_1}$ for $B_1(T_S)$ and using the relation $B_1^*(T_{B,2}^{grd}) \approx B_1^*(T_S) = \alpha_1 T_S^{n_1}$ the last equation can be rewritten to

$$\varepsilon_1^* = 1 - \frac{\varepsilon_1 \alpha_1 T_S^{n_1} - TISIE \alpha_1 T_S^{n_1}}{\tau_1^{sun} \frac{E_1^{sun}}{\pi} \cos \theta_S + L_1^{atm\downarrow}} \quad (5.42)$$

Applying the latter assumptions $TISIE$ can be expressed by

$$TISIE = I + S \frac{L_1^{grd}}{L_2^{grd}} = I + S \frac{\varepsilon_2 B_1^*}{\varepsilon_2 B_2^*} = I + S \frac{\varepsilon_1 \alpha_1 T_S^{n_1}}{\varepsilon_2 \alpha_2 T_S^{n_2}} \quad (5.43)$$

Now, the equation for ε_1^* can be rewritten to

$$\begin{aligned}\varepsilon_1^* &= 1 - \frac{\varepsilon_1 \alpha_1 T_S^{n_1} - \left(I + S \frac{\varepsilon_1 \alpha_1}{\varepsilon_2 \alpha_2} T_S^{n_1 - n_2} \right) \alpha_1 T_S^{n_1}}{\tau_1^{sun} \frac{E_1^{sun}}{\pi} \cos \theta_S + L_1^{atm\downarrow}} \\ &= 1 - \frac{\alpha_1 (\varepsilon_1 - I) T_S^{n_1} - \left(S \frac{\varepsilon_1 \alpha_1^2}{\varepsilon_2 \alpha_2} T_S^{2n_1 - n_2} \right)}{\tau_1^{sun} \frac{E_1^{sun}}{\pi} \cos \theta_S + L_1^{atm\downarrow}}\end{aligned}\quad (5.44)$$

The derivation of ε_1^* to T_S is then given by

$$\frac{\partial \varepsilon_1^*}{\partial T_S} = \frac{n_1 \alpha_1 (\varepsilon_1 - I) T_S^{n_1 - 1} - \left(S \frac{\varepsilon_1 \alpha_1^2}{\varepsilon_2 \alpha_2} (2n_1 - n_2) T_S^{2n_1 - n_2 - 1} \right)}{\tau_1^{sun} \frac{E_1^{sun}}{\pi} \cos \theta_S + L_1^{atm\downarrow}}\quad (5.45)$$

Introducing the values $n_1 \approx 11.5$ and $n_2 \approx 5$ the error magnitude of the MIR emissivity is approximated by

$$\frac{\partial \varepsilon_1^*}{\partial T_S} \approx \frac{n_1 \alpha_1 (\varepsilon_1 - I) T_S^{10.5} - \left(S \frac{\varepsilon_1 \alpha_1^2}{\varepsilon_2 \alpha_2} (2n_1 - n_2) T_S^{17} \right)}{\tau_1^{sun} \frac{E_1^{sun}}{\pi} \cos \theta_S + L_1^{atm\downarrow}}\quad (5.46)$$

From this equation follows that the error magnitude is mainly controlled by the seventeenth power of the surface temperature T_S . This term arises from the product of $TISIE \times B_1^*$. The estimated power dependence agrees with the shape of the error distribution in Figure 5.11. Therefore, the quality of the linear regression method used for the determination of TISIE is mainly responsible for the quality of the estimated MIR emissivity.

The error distribution for the TIR emissivity is almost inverse to the error distribution of the MIR emissivity. This results from the equation for the determination of the TIR emissivity. Applying statistical approaches like a linear regression method a Gaussian error distribution is desired. As seen in Appendix C this condition is given.

In order to analyze the dependence of the errors on the type of the atmosphere the entire data set was divided into four data subsets according to standard atmosphere types, TROP, MLS, MLW, US. Their resulting retrieval errors for the emissivity as well as the temperature are similar. The mean (rms) errors lie around 0.011 and 0.014 for the MIR and TIR emissivity respectively. The temperature retrieval errors vary from 0.4 K to 0.7 K. An overview on the errors according to atmosphere types are given in Table 5.3.

In the error tables the dependence of the method retrieval errors on the sun zenith angle is obvious. The behavior is displayed for a MLS atmosphere in Figures 5.14, 5.15 and 5.16. The figures for the other three atmospheres are located in Appendix C.

Finally, the achieved method retrieval errors demonstrate that the developed TISIE approach will be applicable for the analysis of upcoming BIRD data.

ATM	θ_s [°]	$(\Delta Q)_{rms}$			$(\Delta Q)_{max}$		
		$\Delta\varepsilon_1$	$\Delta\varepsilon_2$	ΔT_s [K]	$\Delta\varepsilon_1$	$\Delta\varepsilon_2$	ΔT_s [K]
TROP	0	0.0058	0.0134	0.417	0.0299	0.0493	1.420
	15	0.0061	0.0133	0.413	0.0314	0.0492	1.398
	30	0.0071	0.0129	0.399	0.0370	0.0488	1.321
	45	0.0096	0.0122	0.366	0.0520	0.0481	1.185
	60	0.0196	0.0104	0.281	0.1142	0.0461	0.947
	all θ_s	0.0109	0.0125	0.378	0.1142	0.0493	1.420
MLS	0	0.0058	0.0148	0.482	0.0338	0.0662	1.676
	15	0.0060	0.0147	0.477	0.0355	0.0662	1.650
	30	0.0070	0.0145	0.463	0.0416	0.0660	1.582
	45	0.0094	0.0139	0.430	0.0575	0.0656	1.463
	60	0.0175	0.0125	0.350	0.1131	0.0646	1.251
	all θ_s	0.0101	0.0141	0.443	0.1131	0.0662	1.676
MLW	0	0.0072	0.0164	0.770	0.0391	0.0452	2.212
	15	0.0075	0.0163	0.765	0.0410	0.0451	2.192
	30	0.0086	0.0161	0.747	0.0476	0.0450	2.128
	45	0.0113	0.0154	0.708	0.0643	0.0447	2.036
	60	0.0191	0.0139	0.615	0.1170	0.0441	1.864
	all θ_s	0.0116	0.0157	0.723	0.1170	0.0452	2.212
US	0	0.0068	0.0157	0.678	0.0378	0.0434	2.053
	15	0.0071	0.0156	0.673	0.0396	0.0433	2.035
	30	0.0082	0.0153	0.656	0.0461	0.0431	1.971
	45	0.0108	0.0147	0.618	0.0626	0.0427	1.859
	60	0.0186	0.0132	0.528	0.1162	0.0417	1.665
	all θ_s	0.0112	0.0149	0.633	0.1162	0.0434	2.053

Table 5.3: Same as Table 5.2, but the entire data set is split into four standard atmospheres

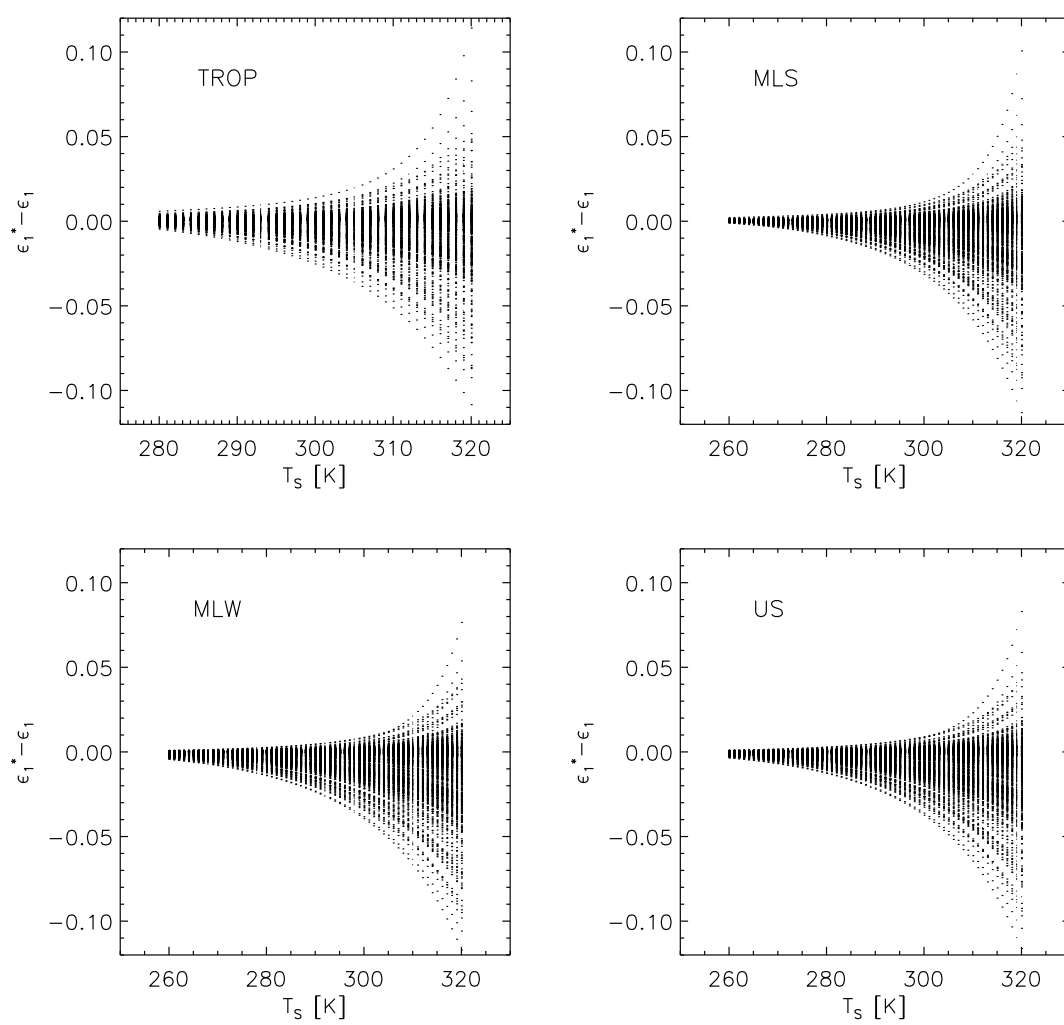


Figure 5.11: MIR emissivity retrieval errors in relation to surface temperatures considering the entire data set (Section 5.1)

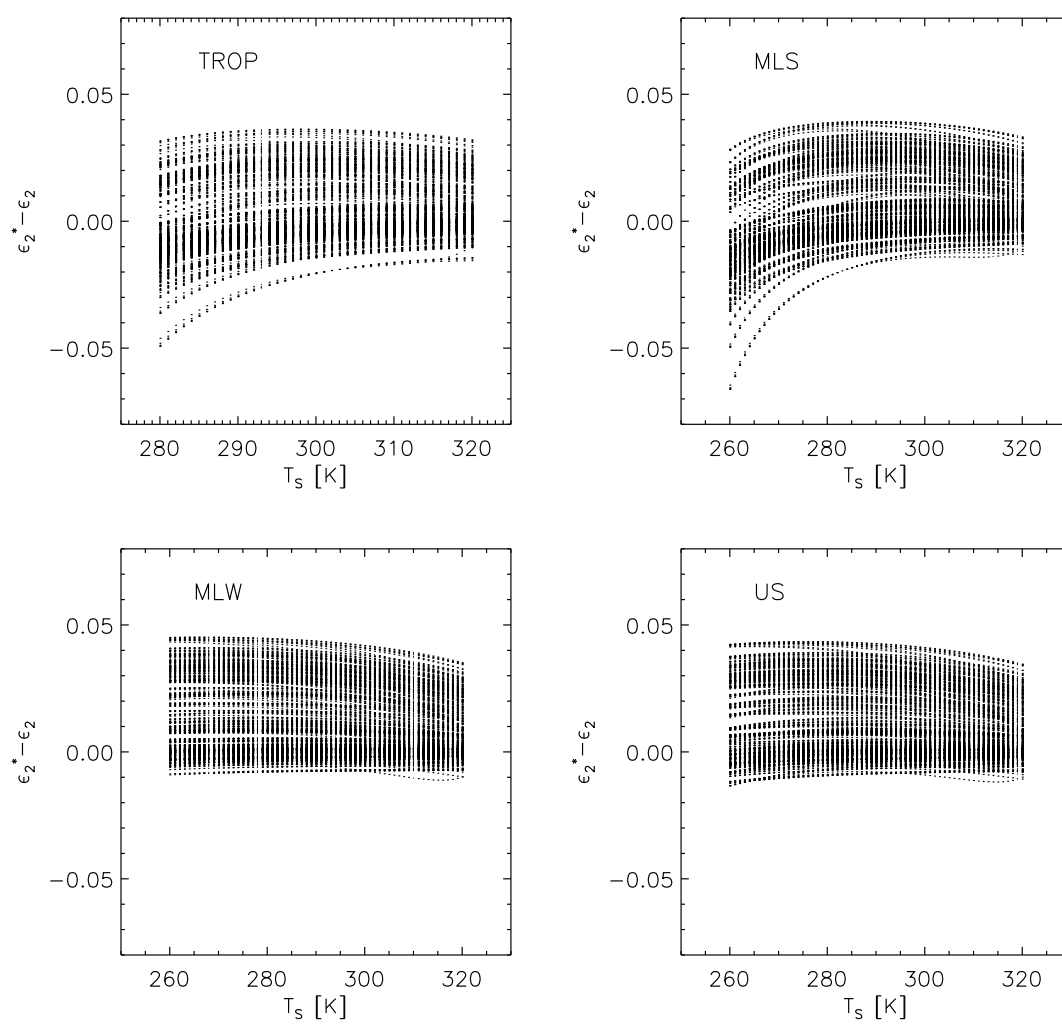


Figure 5.12: TIR emissivity retrieval errors in relation to surface temperatures considering the entire data set (Section 5.1)

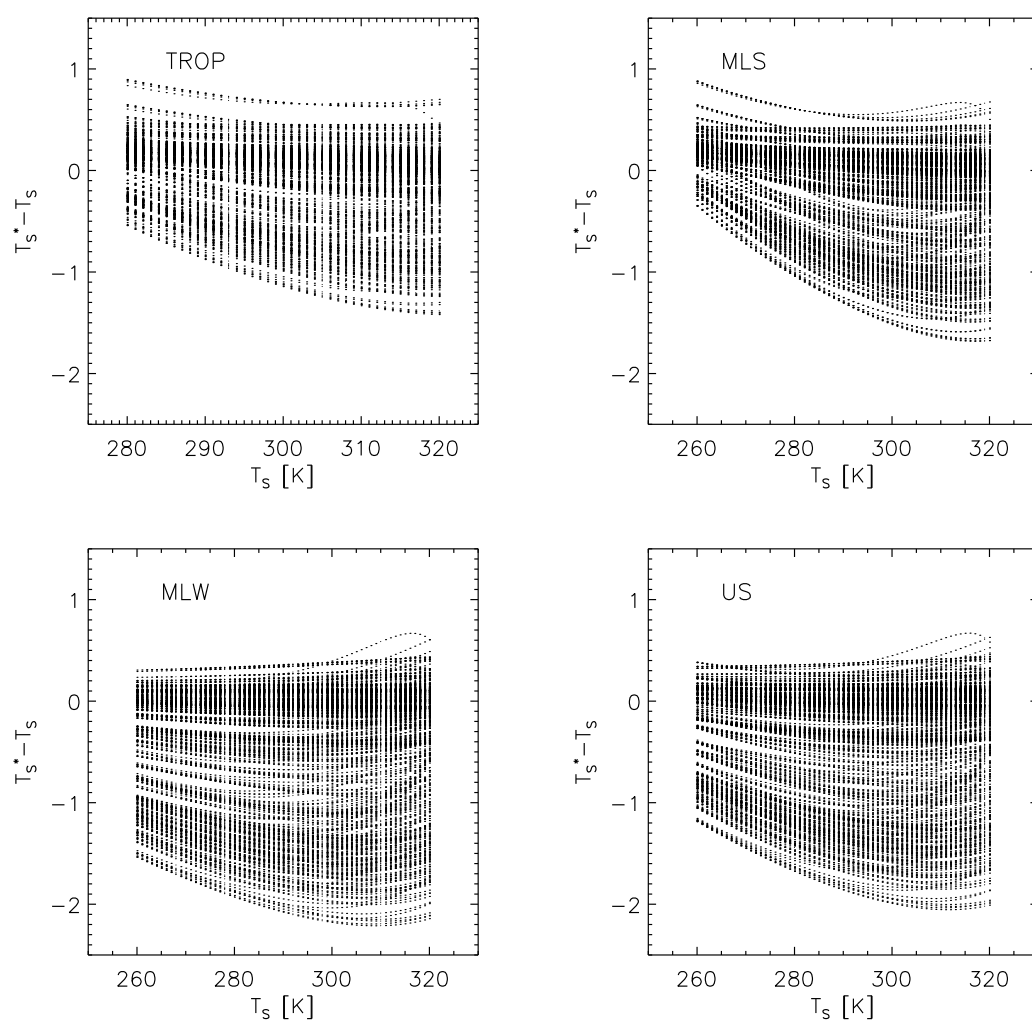


Figure 5.13: Temperature retrieval errors in relation to surface temperatures considering the entire data set (Section 5.1)

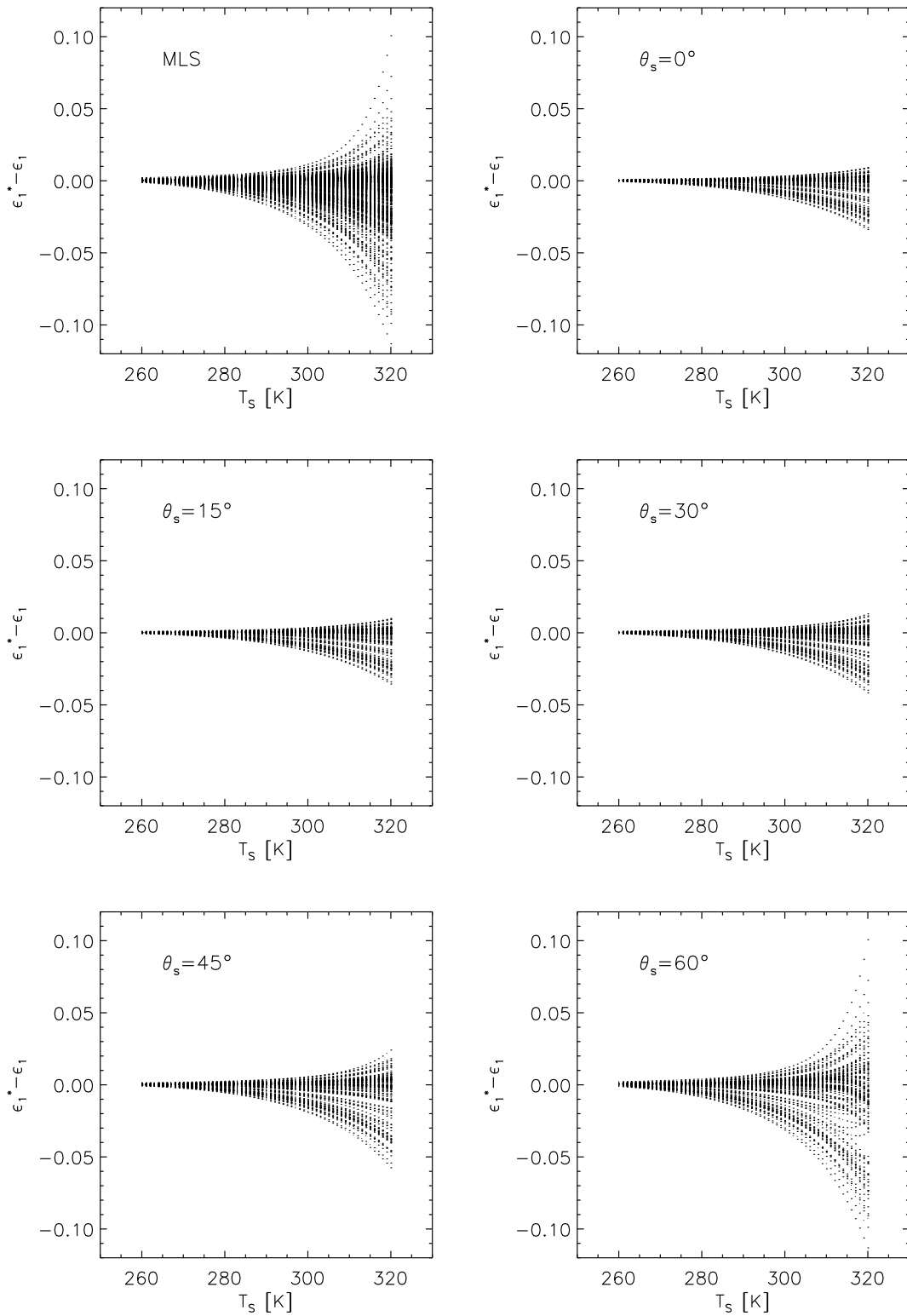


Figure 5.14: MIR emissivity retrieval errors in relation to surface temperatures and solar zenith angles for a mid latitude summer standard atmosphere

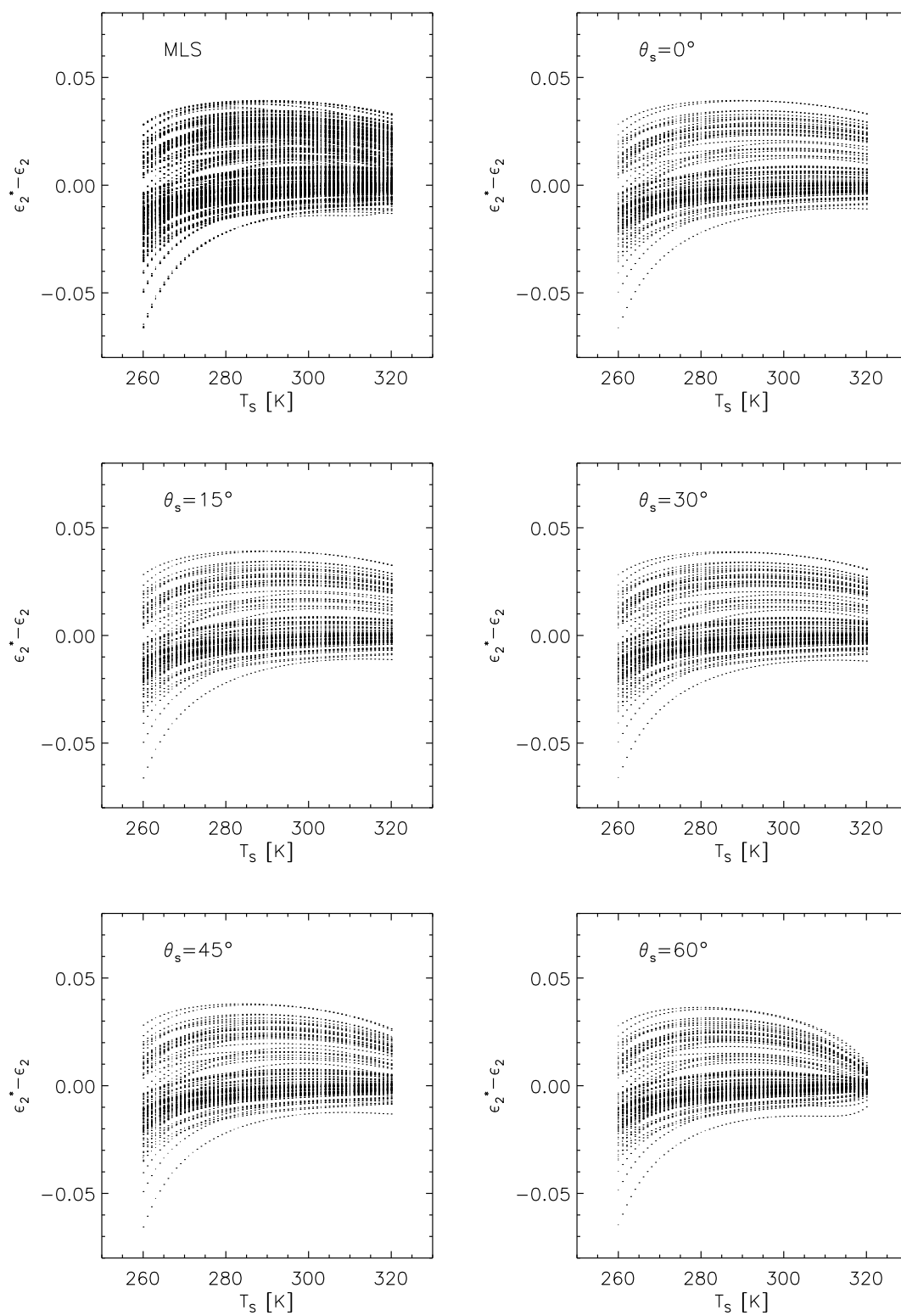


Figure 5.15: TIR emissivity retrieval errors in relation to surface temperatures and solar zenith angles for a mid latitude summer standard atmosphere

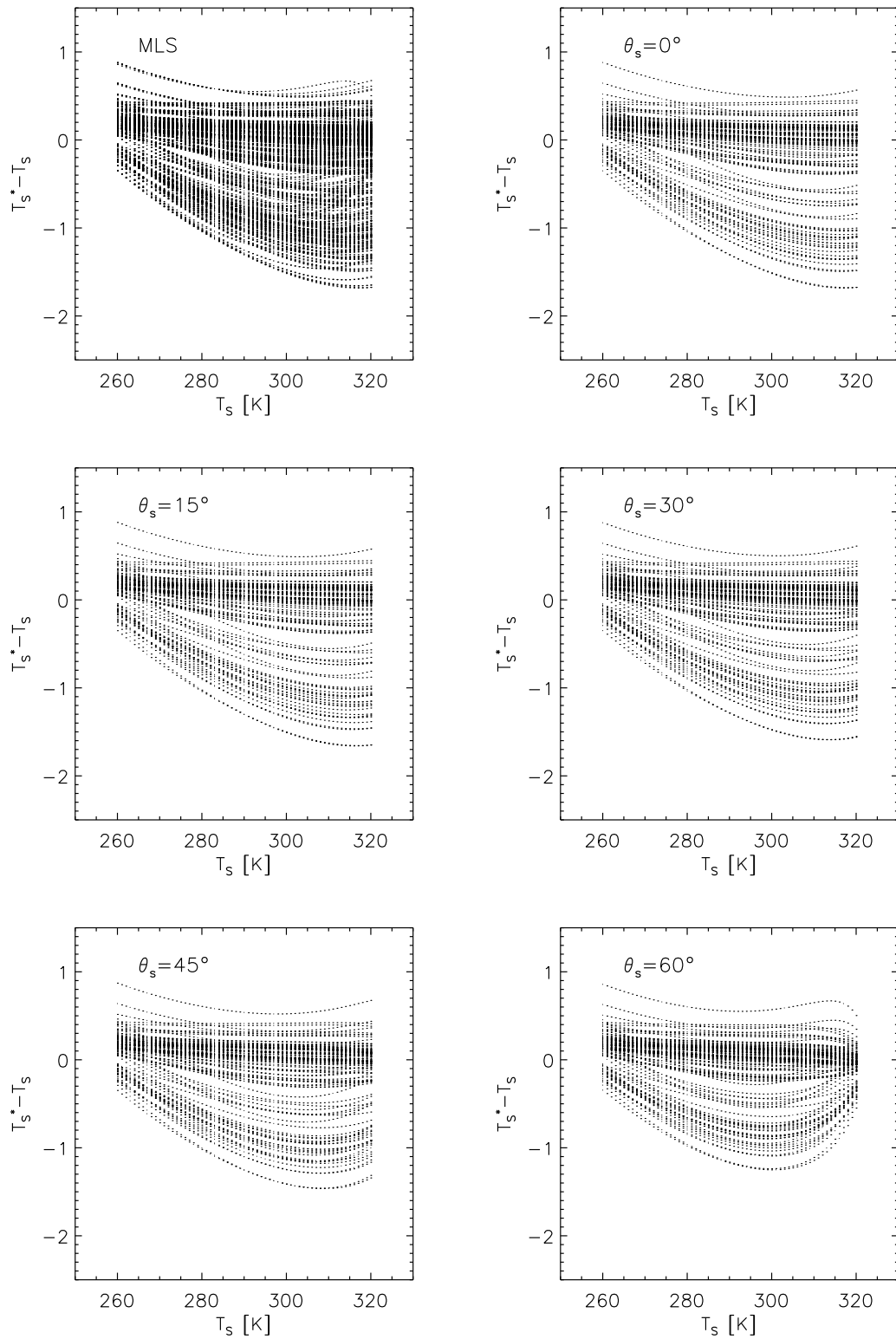


Figure 5.16: Temperature retrieval errors in relation to surface temperatures and solar zenith angles for a mid latitude summer standard atmosphere

5.4.2 Overall Simulation Error

The intention of calculating the overall simulation error was to demonstrate the increase of the retrieval error magnitude due to atmospheric correction using MODTRAN and due to inclusion of noise in the TOA radiance. Thus, the investigations were limited to a mid latitude summer atmosphere. The simulation of the overall error for the entire data set ($\approx 2.3 \times 10^6$ MODTRAN runs for each IR channel) would be extremely time and memory consuming. The purpose of the presented analysis was to approximately examine the influence of the mentioned error sources.

The **flow chart** (Fig. 5.17) gives an overview on the calculation procedure. The MLS data set (see Section 5.1) was used as input data including the true values for the emissivities ε_i , the surface temperature T_S , and the atmospheric properties. For the simulation of realistic conditions, the final atmospheric signal consists of TOA radiances calculated with MODTRAN and a contribution due to atmospheric noise. One cannot presume that MODTRAN’s atmospheric transfer simulations are error free. Therefore, an experience value of 1 % of the TOA radiance calculated with MODTRAN was chosen as random noise based on a Gaussian function.

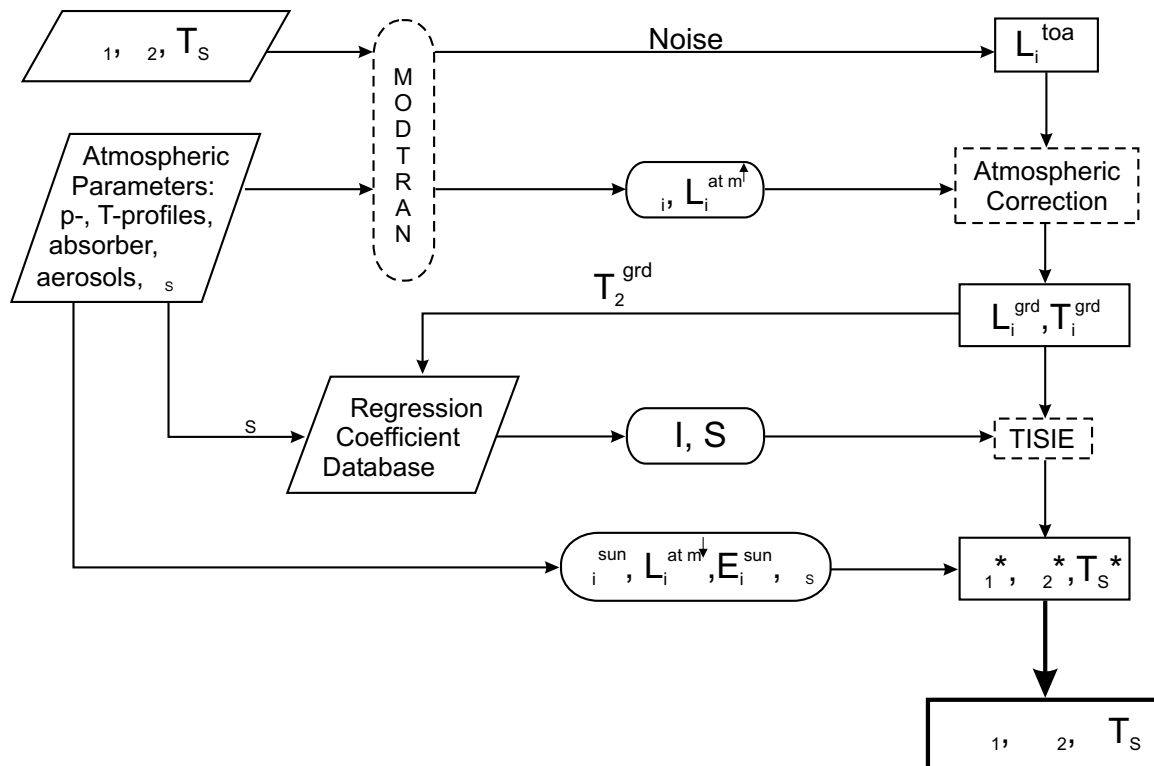


Figure 5.17: Flow chart for the estimation of the overall simulation error

Once having the at-sensor radiance an atmospheric correction is necessary for the determination of the ground radiances. According to the radiative transfer equation at TOA (Eq. (3.1)) an estimation of the ground radiances L_i^{grd} is possible if one neglects the reflected terms. This procedure is appropriate due to the relation of radiance magnitude between emitted and reflected contributions. Thus, the error which is made using the assumption is included in the determined overall retrieval error. Atmospheric quantities like τ_i , L_i^{atm} are given by simulations using MODTRAN depending on the chosen atmospheric conditions.

$$\underbrace{L_1^{toa}(T_{B,1})}_{\text{sensor signal}} = \underbrace{\varepsilon_1 B_1(T_S)}_{L_1^{grd}} \tau_1 + \underbrace{L_1^{atm\uparrow}}_{\text{MODTRAN}} + \underbrace{(1 - \varepsilon_1) L_1^{atm\downarrow} \tau_1 + \frac{(1 - \varepsilon_1)}{\pi} \tau_1^{sun} E_1^{sun} \cos \theta_S \tau_1}_{\text{neglected}} \quad (5.47)$$

$$\underbrace{L_2^{toa}(T_{B,2})}_{\text{sensor signal}} = \underbrace{\varepsilon_2 B_2(T_S)}_{L_2^{grd}} \tau_2 + \underbrace{L_2^{atm\uparrow}}_{\text{MODTRAN}} + \underbrace{(1 - \varepsilon_2) L_2^{atm\downarrow} \tau_2}_{\text{neglected}} \quad (5.48)$$

From Equations (5.47) and (5.48) follows that the ground radiances can be estimated by

$$L_i^{grd} = \frac{L_i^{toa} - L_i^{atm\uparrow}}{\tau_i} \quad (5.49)$$

If the TIR ground radiance is provided the corresponding brightness temperature $T_{B,2}^{grd}$ can be assigned using precalculated look-up tables. $T_{B,2}^{grd}$ is needed for the choice of the appropriate regression coefficients I and S presuming $T_{B,2}^{grd} \approx T_S$. The precalculated regression coefficients are used to retrieve the parameter TISIE which is then inserted in the equation for getting the MIR emissivity (Eq. (5.15)). Again, the atmospheric quantities are calculated using MODTRAN. Now, the surface temperature and the TIR emissivity are easy to recover. The differences between the estimated (ε_i^* , T_S^*) (Eq. (5.17), (5.16)) and true values lead to the overall simulation errors ($\Delta\varepsilon_i$, ΔT_S). The described procedure was applied to each sample of the MLS data set.

The **overall simulation errors** for MIR and TIR emissivity and surface temperature for the MLS data set are summarized in Table 5.4. Comparing the results with the method retrieval errors in Table 5.2 it turns out that both, the atmospheric correction and simulated radiances including random noise, increase the method retrieval error about 100 %. Nevertheless, temperature retrieval errors (rms) of less than 1 K, only arising from the applied method and radiative transfer simulations itself, are acceptable in respect of the BIRD mission objectives. Plots of the overall simulation errors are not presented in this document because the distribution of the overall simulation errors is almost the same as for the method retrieval errors (see Figures 5.11, 5.12, 5.13). The entire retrieval error including all possible error sources and its propagation is discussed in Chapter 6.1.

MLS						
θ_s [°]	$(\Delta Q)_{rms}$			$(\Delta Q)_{max}$		
	$\Delta\varepsilon_1$	$\Delta\varepsilon_2$	ΔT_s [K]	$\Delta\varepsilon_1$	$\Delta\varepsilon_2$	ΔT_s [K]
0	0.0208	0.0239	0.898	0.0554	0.0606	3.121
15	0.0212	0.0239	0.896	0.0532	0.0609	2.790
30	0.0218	0.0240	0.868	0.0493	0.0608	2.837
45	0.0238	0.0243	0.903	0.0645	0.0614	2.900
60	0.0303	0.0255	0.831	0.1285	0.0612	2.656
all θ_s	0.0238	0.0243	0.879	0.1285	0.0614	3.121

Table 5.4: Overall simulation errors for MIR and TIR emissivity and surface temperature for a MLS atmosphere

Chapter 6

Outlook on Both Approaches

In this chapter an estimation of the final retrieval errors for the surface temperature as well as the MIR and TIR emissivity are given.

The algorithms for the application of the presented approaches, “TISIE” and “REGRESSION”, using upcoming BIRD data are summarized in flow charts.

6.1 Final Retrieval Error Estimation

The quality of the retrieved surface temperature and emissivity using one of the investigated methods depends on

- the accuracy of the applied retrieval approach itself ($\Delta T_S, \Delta \varepsilon_i$)
- the quality of radiance measurements at the sensor ($\Delta T^{sensor}, \Delta \varepsilon_i^{sensor}$)
- uncertainty of a priori information on the atmosphere ($\Delta T^{AP}, \Delta \varepsilon_i^{AP}$)

Thus, the final maximum retrieval errors can be expressed as

$$\Delta T_S^{final} \leq \Delta T_S + \Delta T^{sensor} + \Delta T^{AP} \quad (6.1)$$

$$\Delta \varepsilon_i^{final} \leq \Delta \varepsilon_i + \Delta \varepsilon_i^{sensor} + \Delta \varepsilon_i^{AP} \quad (6.2)$$

where index $i = 1, 2$ indicates the infrared BIRD channels MIR and TIR, respectively. Assuming a Gaussian shape for the error distributions the final error distribution $\Delta T_S^{final}, \Delta \varepsilon_i^{final}$ is represented by a Gaussian function with the standard deviation $\Delta T_S^{mean}, \Delta \varepsilon_i^{mean}$.

$$\Delta T_S^{mean} = \sqrt{(\Delta T_S)^2 + (\Delta T^{sensor})^2 + (\Delta T^{AP})^2} \quad (6.3)$$

$$\Delta \varepsilon_i^{mean} = \sqrt{(\Delta \varepsilon_i)^2 + (\Delta \varepsilon_i^{sensor})^2 + (\Delta \varepsilon_i^{AP})^2} \quad (6.4)$$

Then, the probability to find the true value within the interval $[T_S^* - T_S^{mean}, T_S^* + T_S^{mean}]$ and $[\varepsilon_i^* - \varepsilon_i^{mean}, \varepsilon_i^* + \varepsilon_i^{mean}]$ is 68 % where T_S^* and ε_i^* are the estimated values. In the following each error distribution is separately discussed.

Accuracy of investigated approaches

The mean (rms) temperature retrieval errors for the ‘‘TISIE’’ - Approach and the ‘‘Regression’’ - Approach under nighttime condition lie within a range of 0.5 to 2.5 K. The application of the ‘‘Regression’’ - Approach under daytime condition is not recommended due to mean square temperature retrieval errors greater than 5 K to account for extreme atmospheric conditions as volcanic aerosols. The advantage of applying the ‘‘TISIE’’ - Approach is that the temperature as well as the emissivity will be retrieved and thus, no a priori information on the emissivity are necessary.

Average errors between 0.005 and 0.02 for the mid infrared emissivity and around 0.01 for the emissivity in the TIR channel result from the simulation.

Influence of sensor noise on the retrieved quantities

The approaches utilize the at-sensor brightness temperatures either T_i determined by the inversion of the Planck function for the center wavelength of channel i or the at-ground radiances. The impact of sensor noise on the TOA brightness temperature can be estimated by

$$\Delta T_i = \left| \frac{\partial T_i}{\partial L_i^{toa}} \right| \Delta L_i^{toa} \quad (6.5)$$

According to the definition of the Planck function (see Chapter 3) the brightness temperature T_i is given as

$$T_i = \frac{c_2}{\bar{\lambda}_i \ln \left(\frac{c_1 \bar{\lambda}_i^{-5}}{L_{\bar{\lambda}_i}^{toa}} + 1 \right)} \quad (6.6)$$

where $\bar{\lambda}_i$ is the center wavelength of channel i . Thus, ΔT_i can be derived

$$\Delta T_i = \left| \frac{c_1 c_2 \bar{\lambda}_i^{-6}}{\underbrace{L_{\bar{\lambda}_i}^{toa} \left(\ln \left(\frac{c_1 \bar{\lambda}_i^{-5}}{L_{\bar{\lambda}_i}^{toa}} + 1 \right) \right)^2}_{Z_i} (c_1 \bar{\lambda}_i^{-5} + L_{\bar{\lambda}_i}^{toa})} \right| \Delta L_i^{toa} \quad (6.7)$$

The determination of the sensor noise ΔL_i^{toa} for ‘‘normal’’ surface temperatures is still under evaluation. Therefore, a final value for ΔT_i cannot be given at the moment. Introducing typical mean channel-integrated radiances L_i^{toa} for the MLS standard atmosphere, assuming a blackbody ($\varepsilon_i = 1.0$) and the associated center wavelength of BIRD’s MIR and TIR channel in Equation (6.7), a coarse estimation of factor Z_i can be made. As an example, a sensor error ΔL_i^{toa} of 3 % of the at-sensor radiance L_i^{toa} leads to brightness temperature errors ΔT_i of about 1 K within the MIR and about 2.5 K for the TIR channels.

channel	i	$\bar{\lambda}_i$ [μm]	L_i^{toa} [$\text{W}/(\text{m}^2\text{sr}\mu\text{m})$]	Z_i [$\frac{\text{K}}{\text{W}/(\text{m}^2\text{sr}\mu\text{m})}$]	ΔL_i^{toa} [$\text{W}/(\text{m}^2\text{sr}\mu\text{m})$]	ΔT_i [K]
MIR	1	3.8	0.3	73.3	0.009	≈ 0.7
TIR	2	8.9	7.6	6.70	0.228	≈ 1.5

Table 6.1: Exemplary values for an error estimation (part1)

The error propagation of ΔT_i on the surface temperature and emissivity retrieval is summarized and expressed in equations for both approaches in the following.

Taking the basic equation of the “**Regression**” - **Approach** (Eq. 4.13)

$$T_{regr} = a_0 + a_1 T_1 + a_2 T_2 + a_3 W + T_{\epsilon_{corr}} \quad (6.8)$$

the surface temperature error due to sensor noise ΔT_{regr}^{sensor} can be calculated as:

$$\begin{aligned} \Delta T_{regr}^{sensor} &= \left| \frac{\partial T_{regr}}{\partial T_1} \right| \Delta T_1 + \left| \frac{\partial T_{regr}}{\partial T_2} \right| \Delta T_2 \\ &= |a_1| \Delta T_1 + |a_2| \Delta T_2 \end{aligned} \quad (6.9)$$

The application of the “**Regression**” - **Approach** presumes that an emissivity class is known. Therefore, an investigation of an error propagation of sensor noise on the emissivity is not necessary.

In contrast thereto, for the “**TISIE**” - **Approach** the error propagation of sensor noise has to be considered on the determined surface temperature as well as on the retrieved emissivity.

Based on Equations (5.15) the MIR emissivity $\epsilon_{TISIE,1}$ estimated using the “**TISIE**” - **Approach** is given by

$$\begin{aligned} \epsilon_{TISIE,1}(L_i^{toa}) &= 1 - (L_1^{grd}(L_1^{toa}) - \\ &\quad TISIE(L_i^{grd}(L_i^{toa})) B_1^*(T_{B,2}^{grd}(L_2^{toa})) \underbrace{\frac{1}{\tau_1^{sun} \frac{E_1^{sun}}{\pi} \cos \theta_S + L_1^{atm\downarrow}}}_Y \\ &= 1 - L_1^{grd} Y - TISIE B_1^* Y \end{aligned} \quad (6.10)$$

The MIR ground radiance L_1^{grd} is determined according to Equations (5.49).

$$L_i^{grd} = \frac{L_i^{toa} - L_i^{atm\uparrow}}{\tau_i} \quad (6.11)$$

Thus, the MIR emissivity error due to sensor noise can be estimated as

$$\Delta \varepsilon_{TISIE,1}^{sensor} = \left| \frac{\partial \varepsilon_{TISIE,1}}{\partial L_1^{grd}} \frac{\partial L_1^{grd}}{\partial L_1^{toa}} + \frac{\partial \varepsilon_{TISIE,1}}{\partial TISIE} \frac{\partial TISIE}{\partial L_1^{grd}} \frac{\partial L_1^{grd}}{\partial L_1^{toa}} \right| \Delta L_1^{toa} + \left| \frac{\partial \varepsilon_{TISIE,1}}{\partial TISIE} \frac{\partial TISIE}{\partial L_2^{grd}} \frac{\partial L_2^{grd}}{\partial L_2^{toa}} + \frac{\partial \varepsilon_{TISIE,1}}{\partial B_1^*} \frac{\partial B_1^*}{\partial T_{B,2}^{grd}} \frac{\partial T_{B,2}^{grd}}{\partial L_2^{grd}} \frac{\partial L_2^{grd}}{\partial L_2^{toa}} \right| \Delta L_2^{toa} \quad (6.12)$$

Introducing the partial derivations of B_i^* to $T_{B,2}$ according to the definition of B_i^* (Eq. (5.5)), the partial derivations of $TISIE$ to L_i^{grd} (L_i^{toa}) according to (Eq. (5.34)) and the partial derivation of L_1^{grd} to L_1^{toa} the last equation changes to

$$\Delta \varepsilon_{TISIE,1}^{sensor} = \left| Y \tau_1^{-1} + \frac{Y S B_1^*}{\tau_1 L_2^{grd}} \right| \Delta L_1^{toa} + \left| \frac{Y S B_1^* L_1^{grd}}{\tau_2 (L_2^{grd})^2} + TISIE \alpha_1 n_1 Y \left(T_{B,2}^{grd} \right)^{n_1-1} \tau_2^{-1} Z_2 \Big|_{L_2^{grd}} \right| \Delta L_2^{toa} \quad (6.13)$$

The TISIE - Approach starts with the retrieval of the MIR emissivity, then the surface temperature is determined and finally the TIR emissivity is estimated (Eq. (5.15), (5.16) and (5.17)). The propagation of $\Delta \varepsilon_{TISIE,1}^{sensor}$ on the retrieved surface temperature T_{TISIE}^{sensor} and on the TIR emissivity $\varepsilon_{TISIE,2}$ can be calculated using the following equations.

$$\Delta T_{TISIE}^{sensor} = \left| \frac{\partial T_{TISIE}^{sensor}}{\partial B_1} \frac{\partial B_1}{\partial X} \frac{\partial X}{\partial \varepsilon_{TISIE,1}} \right| \Delta \varepsilon_{TISIE,1}^{sensor} \quad (6.14)$$

The first fraction $\frac{\partial T_{TISIE}^{sensor}}{\partial B_1}$ is defined in the same way as Equations (6.5) to (6.7) where $L_{\lambda_i}^{toa}$ is replaced by B_1 . The derivation of B_1 to $X(\varepsilon_{TISIE,1})$ is zero. According to Eq. (5.16) $X(\varepsilon_{TISIE,1})$ is defined as

$$X(\varepsilon_{TISIE,1}) = \left(\frac{L_1^{grd} - (1 - \varepsilon_{TISIE,1}) \left(\tau_1^{sun} \frac{E_1^{sun}}{\pi} \cos \theta_S + L_1^{atm \downarrow} \right)}{\varepsilon_{TISIE,1}} \right)$$

The third term is given by

$$\frac{\partial X}{\partial \varepsilon_{TISIE,1}} = \frac{L_1^{grd} - (1 - \varepsilon_{TISIE,1}) \left(\tau_1^{sun} \frac{E_1^{sun}}{\pi} \cos \theta_S + L_1^{atm \downarrow} \right) - \left(\tau_1^{sun} \frac{E_1^{sun}}{\pi} \cos \theta_S + L_1^{atm \downarrow} \right) \varepsilon_{TISIE,1}}{(\varepsilon_{TISIE,1})^2}$$

Finally, $\Delta T_{TISIE}^{sensor}$ and $\Delta \varepsilon_{TISIE,2}^{sensor}$ can be calculated as

$$\Delta T_{TISIE}^{sensor} = \left| Z_1 \frac{L_1^{grd} - \overbrace{\left(\tau_1^{sun} \frac{E_1^{sun}}{\pi} \cos \theta_S + L_1^{atm \downarrow} \right)}^{1/Y}}{(\varepsilon_{TISIE,1})^2} \right| \Delta \varepsilon_{TISIE,1}^{sensor} \quad (6.15)$$

$$\begin{aligned}
\Delta \varepsilon_{TISIE,2}^{sensor} &= \left| \frac{\partial \varepsilon_{TISIE,2}^{sensor}}{\partial B_2(T_{TISIE}^{sensor})} \frac{\partial B_2(T_{TISIE}^{sensor})^{sensor}}{\partial T_{TISIE}} \right| \Delta T_{TISIE}^{sensor} \\
&= \left| \frac{L_2^{grd} - L_2^{atm,\downarrow}}{(B_2(T_{TISIE}^{sensor}) - L_2^{atm,\downarrow})^2} \alpha_2 n_2 (T_{TISIE}^{sensor})^{n_2-1} \right| \Delta T_{TISIE}^{sensor} \quad (6.16)
\end{aligned}$$

In the following an example of the error estimation for $\Delta \varepsilon_{TISIE,i}^{sensor}$, $\Delta T_{TISIE}^{sensor}$ is given. Utilizing the values in Table 6.1 and 6.2 the errors due to sensor noise, which is conservatively assumed to be 3 % of the sensor signal, are:

$$\begin{aligned}
\Delta \varepsilon_{TISIE,1}^{sensor} &\approx 2.6 * 10^{-7} + 6 * 10^{-7} + 1.2 * 10^{-6} = 2 * 10^{-6} \\
\Delta T_{TISIE}^{sensor} &\approx 2 K \\
\Delta \varepsilon_{TISIE,2}^{sensor} &\approx 0.16 \\
\Delta T_{regr}^{sensor} &\approx 3 K
\end{aligned}$$

MLS standard atmosphere			
quantity	unit	MIR i=1	TIR i=2
T_S	K	289,2	
ε_i		1.0	
θ_s	$^\circ$	30	
$\bar{\lambda}_i$	μm	3.8	8.9
L_i^{toa}	$W/(m^2 sr \mu m)$	≈ 0.30	≈ 7.64
$L_i^{grd} = B_i$	$W/(m^2 sr \mu m)$	≈ 0.313	≈ 7.99
$T_{B,i}^{grd} = T_S$	K	289,2	
τ_i		0.85	0.75
a_i		2.26	1.24
α_i	$W/(m^2 sr \mu m)/K^n$	$1.5 * 10^{-29}$	$3.9 * 10^{-12}$
n_i		11.50	5.26
Y	$[W/(m^2 sr \mu m)]^{-1}$	$\approx 7 * 10^{-5}$	-
S		≈ -16.6	

Table 6.2: Exemplary values for an error estimation (part2)

Uncertainty of a priori information

The results of the sensitivity study (Chapter 3.1) are utilized for the error evaluation due to the uncertainty of a priori information on atmospheric conditions. Assuming a realistic estimation error of 25 % for atmospheric parameters (aerosols, temperature profile and water vapor) the temperature errors summarized in Table 6.3 will be made for a humid MLS atmosphere including rural aerosol. The temperature errors were determined performing radiative transfer simulations for each channel (MIR and TIR) separately (see Chapter 3.1; e.g. $\Delta W = W^{mls} * 0.25$).

atmospheric parameters	$\Delta T_i^{AP} [K]$	
	MIR (i=1)	TIR (i=2)
aerosols	2	1
T-profile	1	3
water vapor	1	3
$\Delta T^{mean,AP} [K]$	2.5	4.3

Table 6.3: Uncertainties of a priori information on atmospheric parameters.

$$\Delta T^{mean,AP} = \sqrt{(\Delta T_i^{AP,aerosols})^2 + (\Delta T_i^{AP,T-profile})^2 + (\Delta T_i^{AP,water vapor})^2}$$

From this summary it is evident that a temperature retrieval error ($\Delta T^{AP} = \Delta T^{mean,AP}$) of about 3.5 K due to uncertainties in the estimation of atmospheric parameters has to be taken into account.

The uncertainty of a priori information on the emissivity has to be considered for the “Regression” - Approach only and is assumed to be 0.1 for both channels.

In conclusion, the mean final retrieval error for the surface temperature and the emissivity will approximately have a magnitude of

$$\begin{aligned} \Delta T_{S,reg}^{mean} &= \sqrt{(\Delta T_S)^2 + (\Delta T_{reg}^{sensor})^2 + (\Delta T^{AP})^2} \\ &\lesssim \sqrt{(1.5 K)^2 + (3 K)^2 + (3.5 K)^2} \lesssim 4.8 K \end{aligned} \quad (6.17)$$

$$\begin{aligned} \Delta T_{S,TISIE}^{mean} &= \sqrt{(\Delta T_S)^2 + (\Delta T_{TISIE}^{sensor})^2 + (\Delta T^{AP})^2} \\ &\lesssim \sqrt{(1.5 K)^2 + (2 K)^2 + (3.5 K)^2} \lesssim 4.3 K \end{aligned} \quad (6.18)$$

$$\begin{aligned} \Delta \varepsilon_i^{mean} &= \sqrt{(\Delta \varepsilon_i)^2 + (\Delta \varepsilon_i^{sensor})^2 + (\Delta \varepsilon_i^{AP})^2} \\ \Delta \varepsilon_1^{mean} &\lesssim \sqrt{0.02^2 + (2 * 10^{-6})^2 + 0.1^2} \lesssim 0.1 \end{aligned} \quad (6.19)$$

$$\Delta \varepsilon_2^{mean} \lesssim \sqrt{0.02^2 + 0.16^2 + 0.1^2} \lesssim 0.2 \quad (6.20)$$

These errors are not comparable with the results of the common temperature retrieval methods using for instance AVHRR data since the utilized channels do not completely lie within the optimal atmospheric window around 10 μm . It has to be pointed out that the error magnitudes result from a trade-off between the main and secondary

objectives of the BIRD mission which are the HTE detection and vegetation monitoring, respectively. These errors might be acceptable within the frame of these objectives for some vegetation studies under the condition that a sufficient amount of precise a priori information are provided.

6.2 Algorithm for Upcoming BIRD Data

The flow charts on the next pages (Fig. 6.1, 6.2) demonstrate the sequence of temperature and emissivity retrieval for upcoming BIRD data utilizing the investigated methods.

For both approaches a priori information is needed. Look-up tables for certain parameters (integrated Planck function, regression coefficients) are required. They were calculated in the course of this work and are provided in files that are accessible through the Institute of Space Sensor Technology and Planetary Exploration of DLR (maria.schoenermark@dlr.de). The advantage of the “TISIE” - Approach is that the surface temperature as well as the emissivity for both channels can be retrieved. Furthermore, the investigations of this approach show a feasibility for daytime conditions, while the “Regression” - Approach is applicable under nighttime conditions only .

Both algorithms are intended to be used for case studies (non operational usage) of upcoming BIRD images since some a priori information has to be provided. Considering the focus of the BIRD mission, which shall demonstrate the new technological and scientific feasibility of a remote sensing small satellite mission under low budget constrains, the possible accuracy of surface temperature retrieval is encouraging. Provided the proper a priori information, a total maximum retrieval error of $\approx \pm 3.5 K$ for the temperature is predictable for normal surface temperatures. However, the need of a priori information is a serious drawback for an operational application.

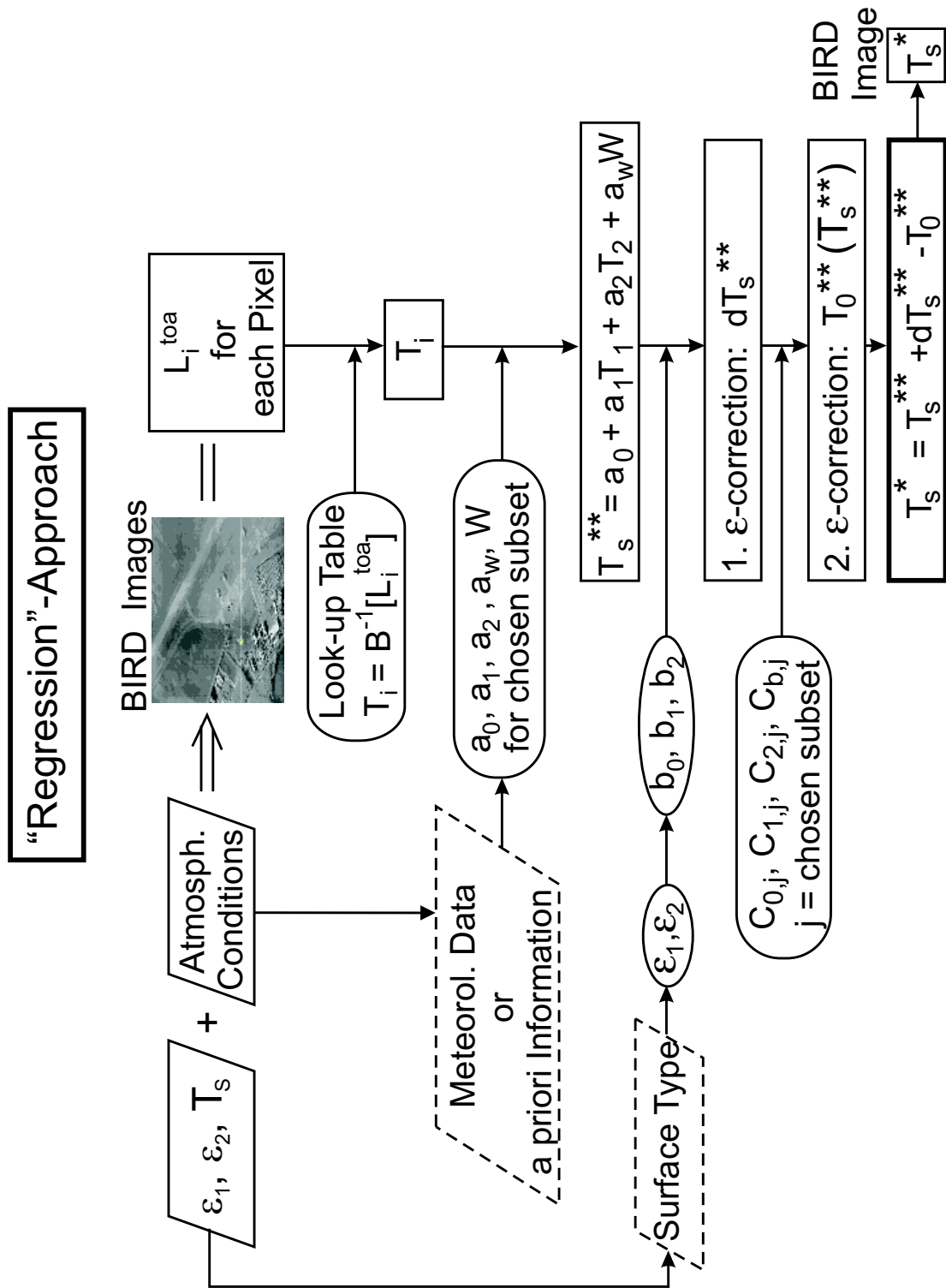


Figure 6.1: Flow chart for the application of the “Regression” - Approach

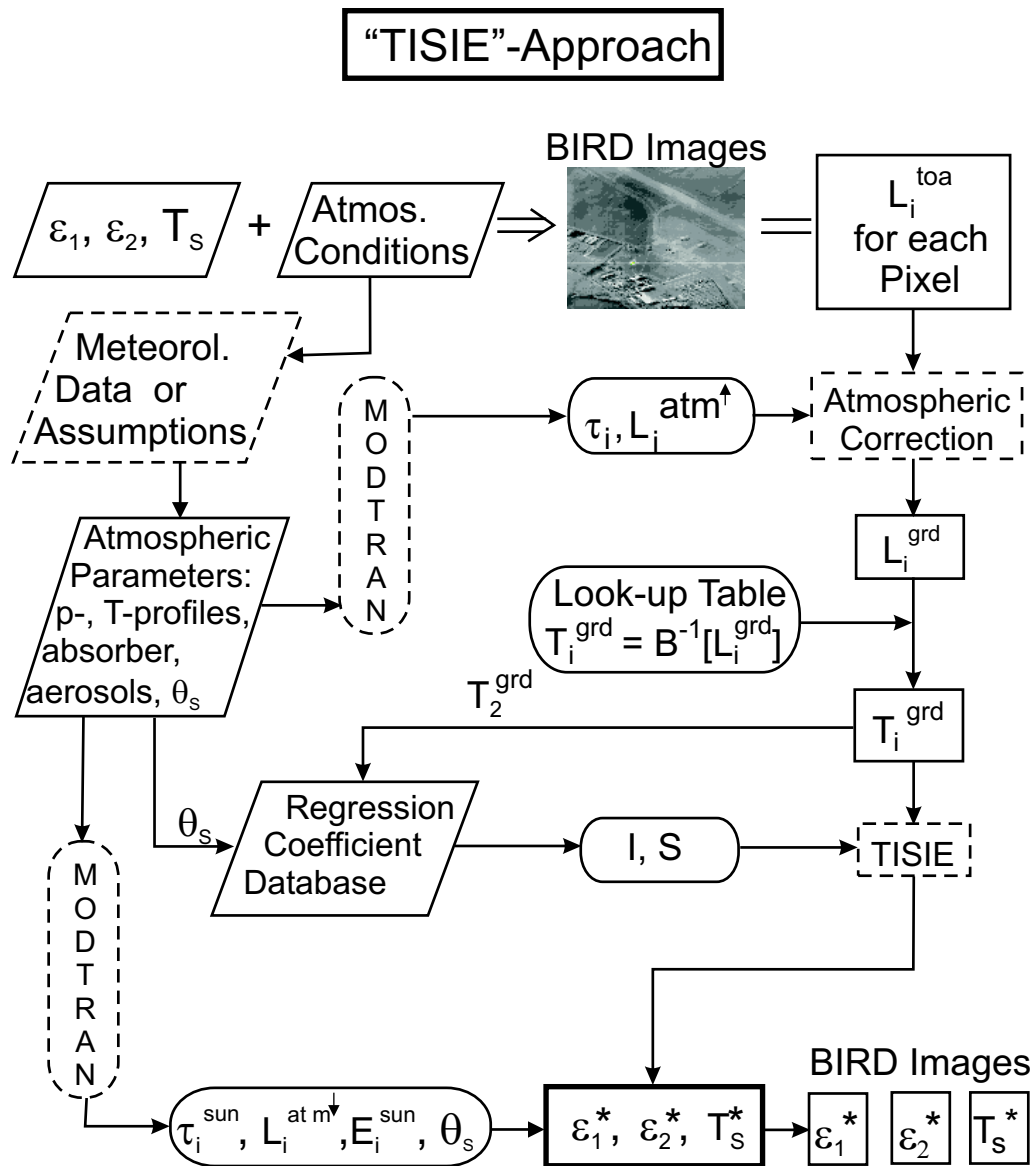


Figure 6.2: Flow chart for the application of the “TISIE” - Approach

Chapter 7

Conclusions

The German Aerospace Center (Deutsches Zentrum für Luft- und Raumfahrt - DLR) is going to launch a multi-spectral sensor system called BIRD (Bi-spectral InfraRed Detection) in 2001. The main scientific objectives of the BIRD mission are the investigation of High-Temperature-Events and vegetation exploration (see Chapter 2). BIRD does not have any thermal channel located within the atmospheric window between 10 and 12 μm . This spectral region is generally used for temperature retrieval due to the high transparency of the atmosphere. Although several methods using atmospheric window channels are established and validated none of them can be applied to BIRD. For that purpose temperature retrieval methods for land surfaces adapted to the specified channel configuration of BIRD (3.4 – 4.2 μm and 8.5 – 9.3 μm) were necessary to be developed.

Two land surface temperature retrieval approaches are presented in this document. One method is based on a bi-spectral technique utilizing the top-of-atmosphere brightness temperatures of both infrared BIRD channels (see Chapter 4). For the investigation of that approach a large synthetic data set consisting of 792 000 coupled surface and atmospheric models was produced using the radiative transfer model MODTRAN. Land surfaces are characterized by the emissivity. Therefore, a two-step emissivity correction was employed.

The second approach separates the temperature and emissivity using ground radiances from BIRD's MIR and TIR channels (see Chapter 5). The TIR at-ground brightness temperature is utilized for the estimation of the thermal contribution to the MIR ground radiance. Thus, an emissivity correction factor called TISIE was introduced to account for the emissivity differences between both IR channels. Once the MIR emissivity is derived from the inverted radiative transfer equation, the temperature and the TIR emissivity can be retrieved as well. An atmospheric correction has to be applied first.

Both investigated methods lead to similar results for surfaces with high emissivity which is the case for considered samples such as lake water, soil, and vegetation. The results are valid for the Lambertian condition and homogeneous pixels. The temperature retrieval rms-errors for the "TISIE" - Approach and the "Regression" - Approach under nighttime conditions lie around 1 K and within a range of 0.5 to 2.5 K, respec-

tively, considering high emissivity. The advantage of applying the “TISIE”-approach is that no a priori information on the emissivity are necessary although an atmospheric correction has to be applied first. The maximum error could arise up to 3 K for the “TISIE” - Approach and up to around 8 K for the “Regression” - Approach due to the inclusion of extreme atmospheric states as volcanic aerosols. The extreme models must be considered in order to estimate realistic errors for the usage of upcoming BIRD data. The application of the “Regression” - Approach during daytime is not recommended due to rms temperature retrieval errors greater than 5 K .

A final discussion of all possible error sources given in Chapter 6 leads to temperature retrieval errors of about 5 K and emissivity errors of 0.15. The maximum errors of the “Regression” - Approach are not satisfactory for vegetation applications.

It turns out that BIRD’s infrared channels are inappropriate for “normal” temperature retrieval with an accuracy known from AVHRR data algorithm. The error magnitude results from a trade-off between the main and secondary objectives of the BIRD mission, which are the HTE detection and vegetation monitoring, respectively. The algorithm might be applicable within the frame of these objectives for particular vegetation studies using certain a priori information which has to be provided with a good precision. But, considering the focus of the BIRD mission, which shall demonstrate the new technological and scientific feasibility of a remote sensing small satellite mission under low budget constrains, the possible accuracy of surface temperature retrieval is encouraging particularly as in the framework of later missions as FOCUS. Within that mission the Fourier transform spectro-radiometer MIROR (Michelson Interferometer with ROTating Retroreflector) might deliver more and precise information on the atmospheric state during the overpass time.

In conclusion, the presented results are to be considered as a first case study of utilizing BIRD’s MIR and TIR channel to examine vegetation surfaces. Finally, it is obvious that both algorithms have to be validated on air- and spaceborne data. Further investigations on the presented subject are in progress.

Appendix A

Further Results of “Regression” - Approach

In this appendix the regression coefficients for the bi-spectral regression method (method_B) using the *blackbody* data set are summarized for simulated night- and daytime data. Further plots of the temperature retrieval distributions for certain surface types are included.

surface type	simulated data
<i>blackbody</i>	daytime
<i>water/vegetation</i>	daytime
<i>bare soil</i>	nighttime
<i>urban areas</i>	nighttime
<i>forest</i>	nighttime

AP-Index	coefficients				
	a_0	a_1	a_2	a_3	R
SC-AD	-77.89	1.81	-0.65	-2.01	0.97
SC-AW	-95.23	2.24	-1.06	-0.52	0.96
SW-AD	-48.22	2.26	-1.24	-1.75	0.99
SW-AW	-35.16	2.09	-1.10	-1.02	0.99
non	-67.81	2.03	-0.92	-0.91	0.99

Table A.1: Temperature retrieval regression coefficients $a_i, i = 0, \dots, 3$ and the regression correlation coefficient R between true and estimated surface temperatures utilizing a *blackbody* data set $\varepsilon_i = 1.0$ and simulated nighttime data (AP-index=non: no division into subsets)

AP-Index	coefficients				
	a_0	a_1	a_2	a_3	R
SC-AD	-72.31	1.10	0.09	-1.98	0.96
SC-AW	-108.82	1.69	-0.42	-0.89	0.94
SW-AD	-53.20	2.09	-1.04	-1.61	0.99
SW-AW	-41.72	2.03	-1.02	-1.01	0.99
non	-76.10	1.85	-0.71	-0.86	0.99

Table A.2: Same as Table A.1 but using simulated daytime data

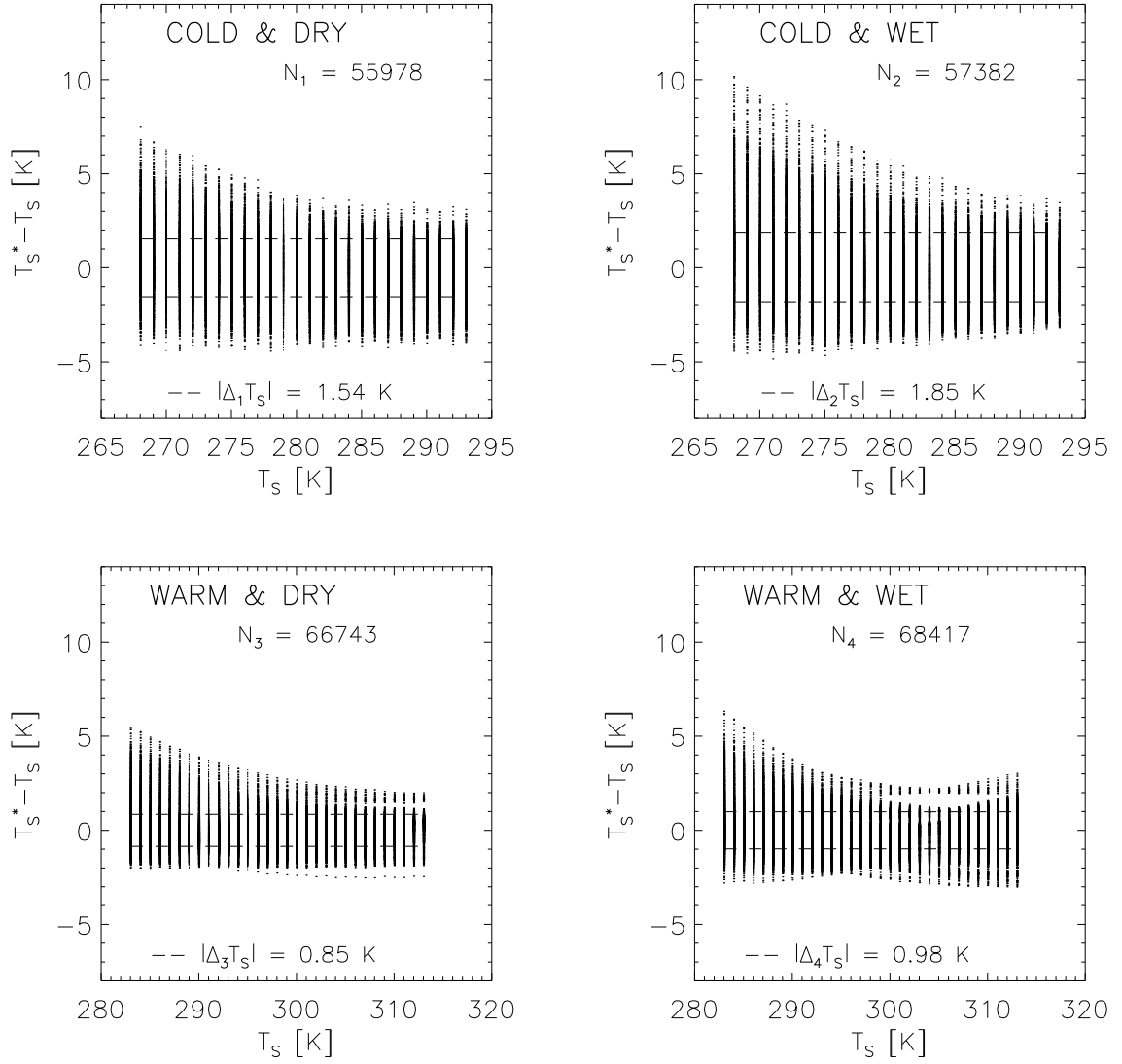


Figure A.1: Temperature retrieval errors ($T_s^* - T_s$) versus surface temperatures (T_s) utilizing the *blackbody* data set and simulated daytime data with $|\Delta_j T_s| = \pm \Delta_j^{1,0} T_s$. Note, that $T_s^{**} = T_s^*$ for the *blackbody* data set since no emissivity correction is needed.

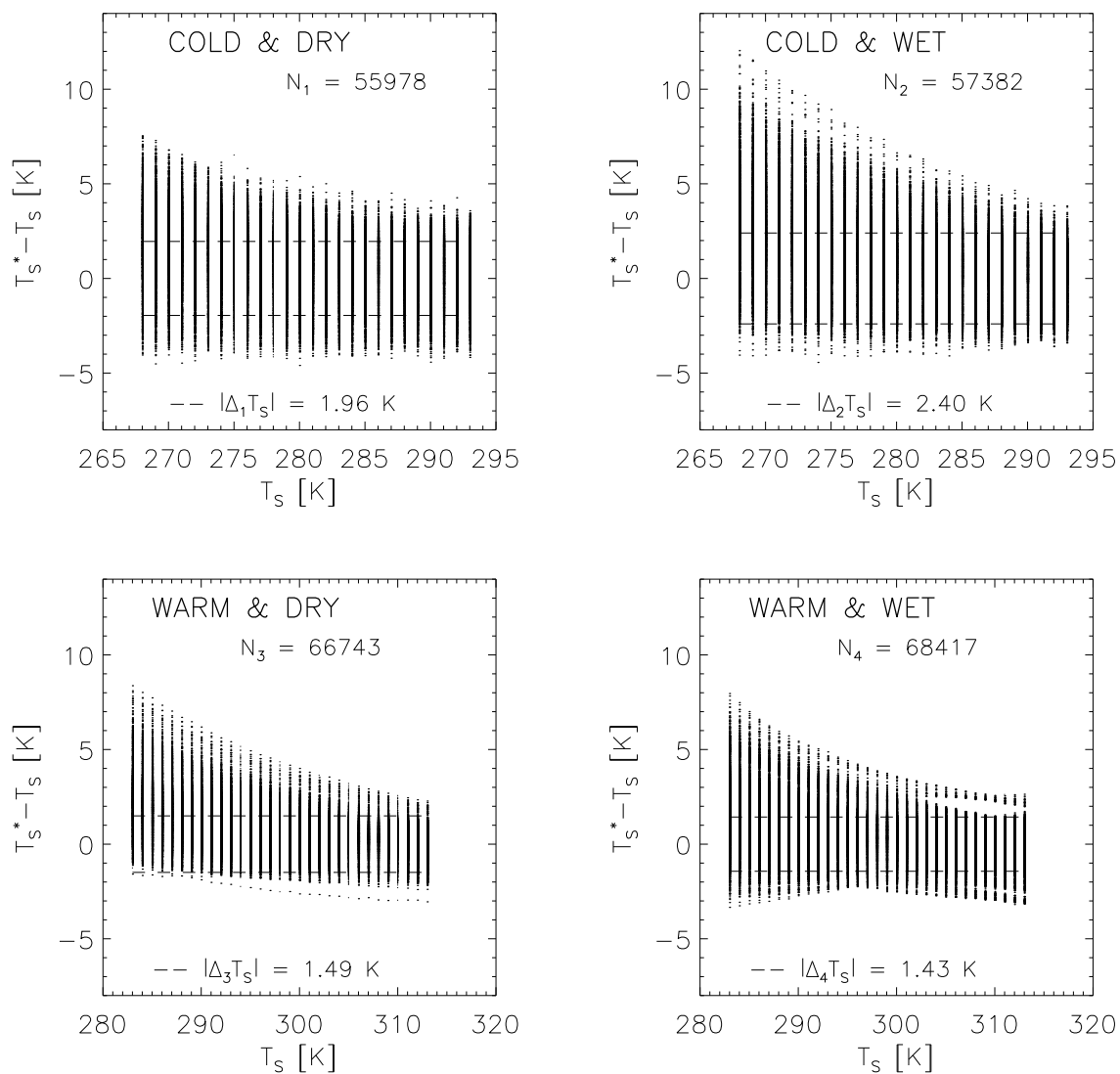


Figure A.2: Temperature retrieval errors ($T_s^* - T_s$) versus surface temperatures (T_s) utilizing the *water/vegetation* data set and simulated daytime data with $|\Delta_j T_s| = \pm \Delta_j^{1.0} T_s$

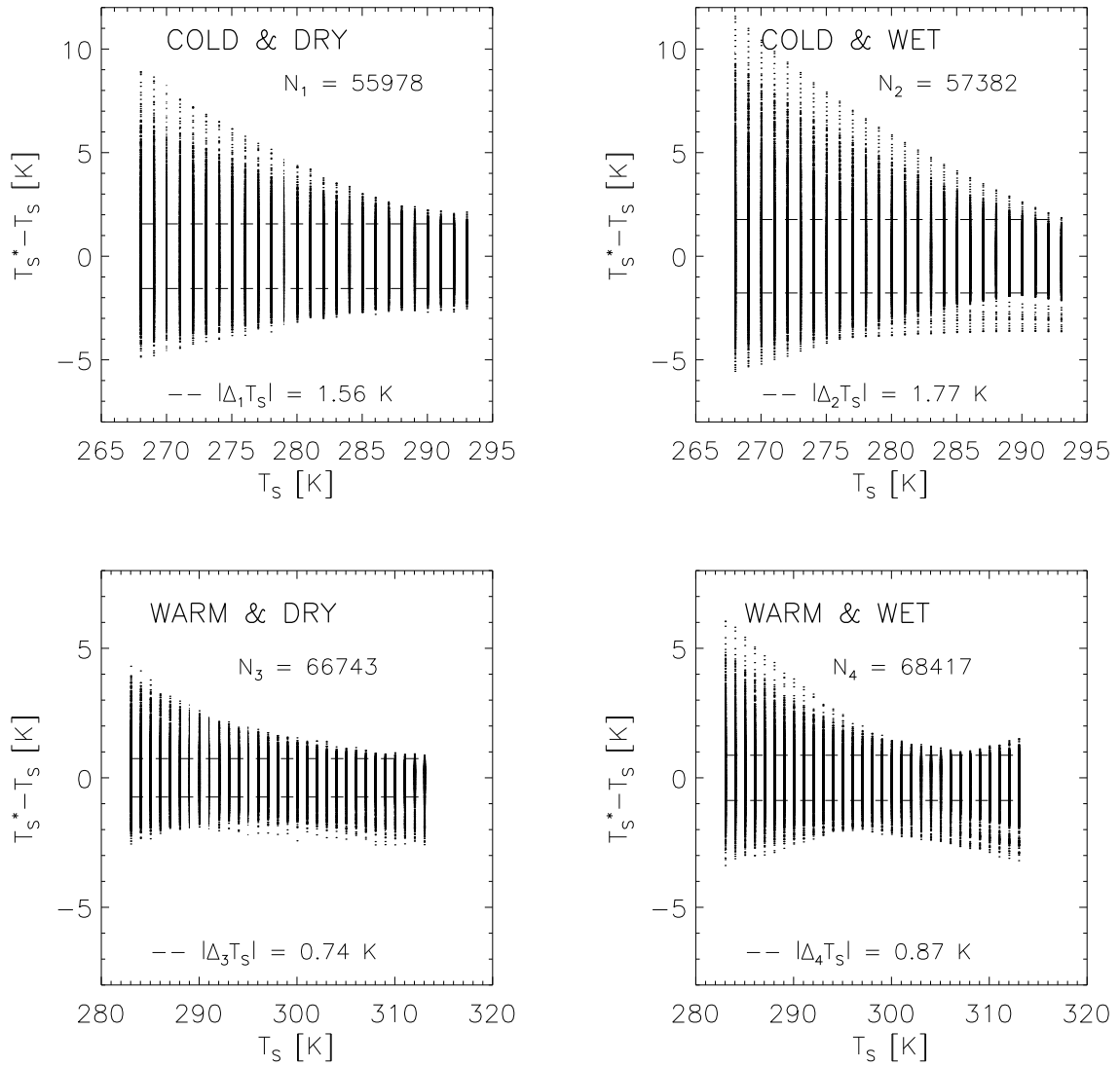


Figure A.3: Temperature retrieval errors ($T_s^* - T_s$) versus surface temperatures (T_s) utilizing the *bare soil* data set and simulated nighttime data with $|\Delta_j T_s| = \pm \Delta_j^{1.0} T_s$

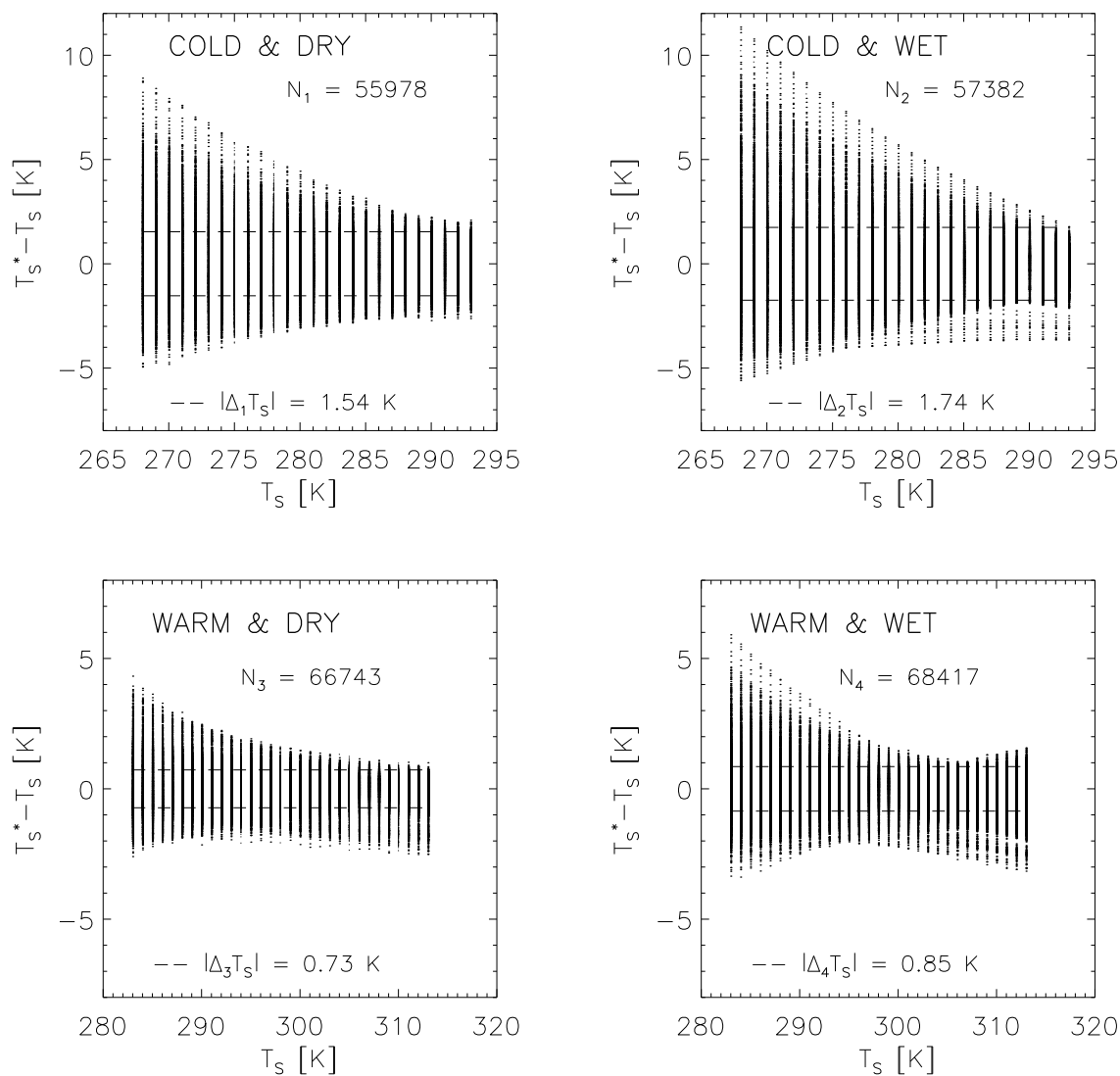


Figure A.4: Temperature retrieval errors ($T_s^* - T_s$) versus surface temperatures (T_s) utilizing the data set for *urban areas* and simulated nighttime data with $|\Delta_j T_s| = \pm \Delta_j^{1.0} T_s$

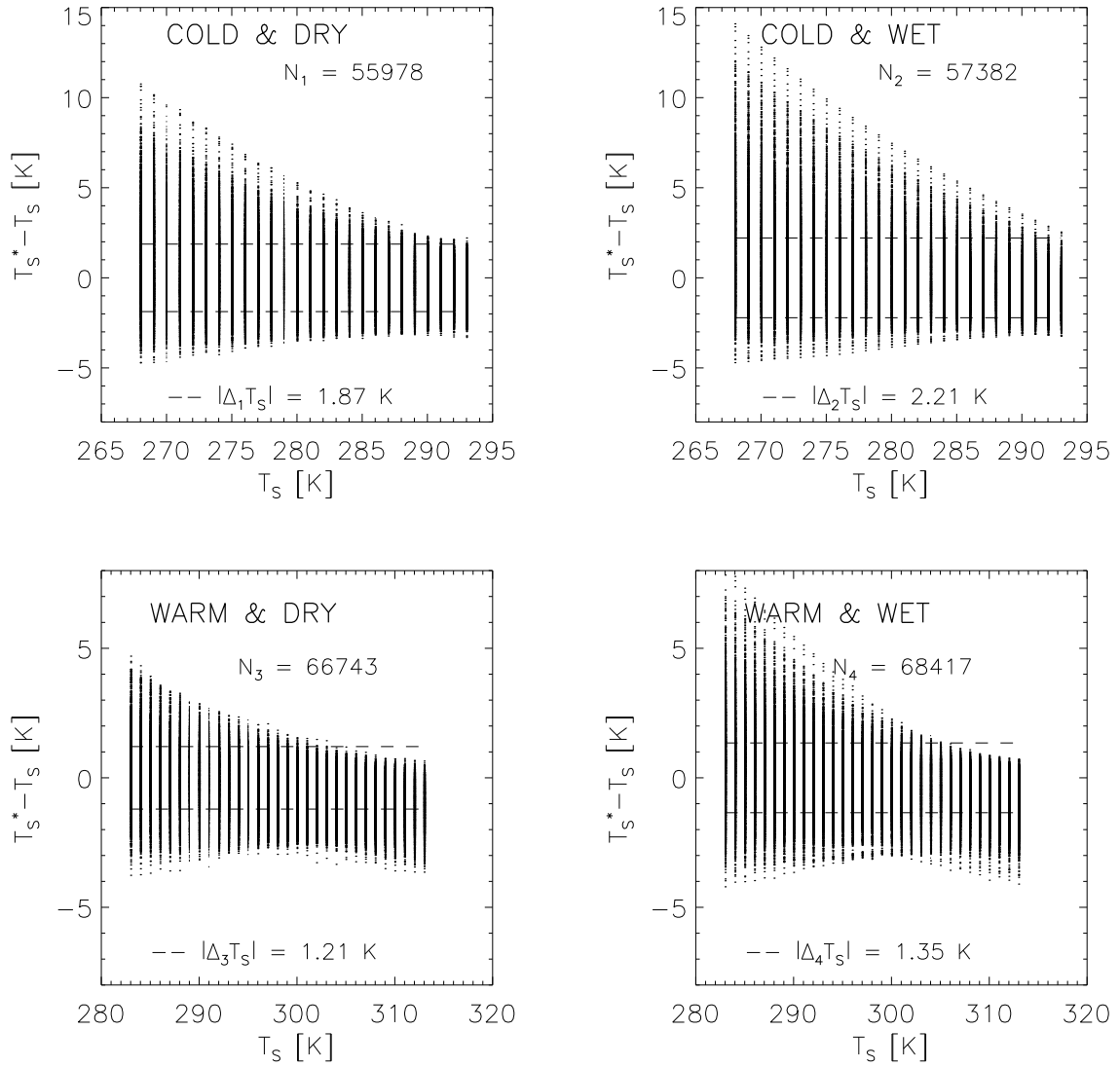


Figure A.5: Temperature retrieval errors ($T_s^* - T_s$) versus surface temperatures (T_s) utilizing the *forest* data set and simulated nighttime data with $|\Delta_j T_s| = \pm \Delta_j^{1.0} T_s$

Appendix B

TISIE Regression Coefficients

The tables on the regression and correlation coefficients for the linear fit of $TISIE_a$ and $TISIE_b$ (Eq. (5.34)) are included in this appendix.

- $TISIE_a$
 - mid latitude summer standard atmosphere (MLS), Fig. B.1
 - tropical standard atmosphere (TROP), Fig. B.2
 - mid latitude winter standard atmosphere (MLW), Fig. B.3
 - US-standard atmosphere (US), Fig. B.4

- $TISIE_b$
 - mid latitude summer standard atmosphere (MLS), Fig. B.5
 - tropical standard atmosphere (TROP), Fig. B.6
 - mid latitude winter standard atmosphere (MLW), Fig. B.7
 - US-standard atmosphere (US), Fig. B.8

MLS				
θ_s [°]	T_s [K]	<i>Intercept</i>	<i>Slope</i>	<i>R</i>
0	260	1.0322	-6.8254	0.96
	270	1.0482	-8.6681	0.96
	280	1.0741	-10.9427	0.96
	290	1.1150	-13.8005	0.96
	300	1.1798	-17.5028	0.95
	310	1.2840	-22.5260	0.94
	320	1.4576	-29.7920	0.93
15	260	1.0331	-7.1100	0.96
	270	1.0499	-9.0356	0.96
	280	1.0769	-11.4185	0.96
	290	1.1198	-14.4238	0.96
	300	1.1879	-18.3388	0.95
	310	1.2982	-23.6929	0.94
	320	1.4836	-31.5221	0.92
30	260	1.0365	-8.0956	0.96
	270	1.0557	-10.3120	0.96
	280	1.0868	-13.0788	0.96
	290	1.1366	-16.6144	0.95
	300	1.2170	-21.3098	0.95
	310	1.3497	-27.9101	0.94
	320	1.5799	-37.9252	0.91
45	260	1.0441	-10.3573	0.96
	270	1.0691	-13.2633	0.96
	280	1.1100	-16.9640	0.96
	290	1.1768	-21.8372	0.95
	300	1.2882	-28.6013	0.94
	310	1.4817	-38.7282	0.93
	320	1.8412	-55.3341	0.88
60	260	1.0634	-16.0835	0.96
	270	1.1036	-20.8774	0.96
	280	1.1716	-27.2943	0.95
	290	1.2890	-36.4088	0.95
	300	1.5025	-50.5623	0.93
	310	1.9251	-75.1521	0.88
	320	2.6314	-108.7659	0.66

Table B.1: Regression coefficients and correlation coefficient R for the relation between $TISIE_a$ and at-ground radiance ratio L_1^{grd}/L_2^{grd} (Eq. (5.18), (5.34)) for the mid latitude summer standard atmosphere

TROP				
θ_s [°]	T_s [K]	<i>Intercept</i>	<i>Slope</i>	<i>R</i>
0	260	1.0334	-7.0977	0.96
	270	1.0500	-8.9977	0.96
	280	1.0767	-11.3518	0.96
	290	1.1192	-14.3254	0.96
	300	1.1868	-18.2075	0.95
	310	1.2964	-23.5346	0.95
	320	1.4817	-31.3777	0.93
15	260	1.0345	-7.3976	0.96
	270	1.0518	-9.3847	0.96
	280	1.0797	-11.8535	0.96
	290	1.1243	-14.9848	0.96
	300	1.1955	-19.0975	0.95
	310	1.3118	-24.7902	0.94
	320	1.5102	-33.2751	0.93
30	260	1.0380	-8.4379	0.96
	270	1.0579	-10.7316	0.96
	280	1.0902	-13.6083	0.96
	290	1.1421	-17.3093	0.96
	300	1.2265	-22.2730	0.95
	310	1.3675	-29.3559	0.94
	320	1.6170	-40.3715	0.92
45	260	1.0461	-10.8334	0.96
	270	1.0720	-13.8589	0.96
	280	1.1148	-17.7368	0.96
	290	1.1851	-22.8918	0.96
	300	1.3035	-30.1502	0.95
	310	1.5130	-41.2723	0.93
	320	1.9162	-60.2877	0.89
60	260	1.0666	-16.9336	0.96
	270	1.1089	-21.9906	0.96
	280	1.1810	-28.8370	0.96
	290	1.3070	-38.7347	0.95
	300	1.5419	-54.5705	0.93
	310	2.0302	-83.7174	0.89
	320	2.8905	-126.0671	0.64

Table B.2: Regression coefficients and correlation coefficient R for the relation between $TISIE_a$ and at-ground radiance ratio L_1^{grd}/L_2^{grd} (Eq. (5.18), (5.34)) for the tropical standard atmosphere

MLW				
θ_s [°]	T_s [K]	<i>Intercept</i>	<i>Slope</i>	<i>R</i>
0	260	1.0298	-6.3176	0.96
	270	1.0450	-8.0487	0.96
	280	1.0691	-10.1710	0.96
	290	1.1071	-12.8124	0.95
	300	1.1667	-16.1884	0.95
	310	1.2612	-20.6795	0.94
	320	1.4150	-26.9855	0.92
15	260	1.0307	-6.5735	0.96
	270	1.0465	-8.3794	0.96
	280	1.0716	-10.5984	0.96
	290	1.1113	-13.3691	0.95
	300	1.1739	-16.9271	0.95
	310	1.2735	-21.6920	0.94
	320	1.4369	-28.4407	0.92
30	260	1.0337	-7.4569	0.96
	270	1.0516	-9.5240	0.96
	280	1.0805	-12.0829	0.95
	290	1.1263	-15.3143	0.95
	300	1.1993	-19.5322	0.94
	310	1.3177	-25.3108	0.93
	320	1.5164	-33.7339	0.91
45	260	1.0405	-9.4680	0.96
	270	1.0635	-12.1461	0.96
	280	1.1010	-15.5180	0.95
	290	1.1615	-19.8853	0.95
	300	1.2605	-25.7990	0.94
	310	1.4275	-34.3176	0.92
	320	1.7217	-47.4328	0.88
60	260	1.0575	-14.4875	0.96
	270	1.0937	-18.7920	0.95
	280	1.1542	-24.4402	0.95
	290	1.2564	-32.2217	0.94
	300	1.4354	-43.7243	0.92
	310	1.7651	-62.0892	0.87
	320	2.2975	-86.4052	0.70

Table B.3: Regression coefficients and correlation coefficient R for the relation between $TISIE_a$ and at-ground radiance ratio L_1^{grd}/L_2^{grd} (Eq. (5.18), (5.34)) for the mid latitude winter standard atmosphere

US				
θ_s [°]	T_s [K]	<i>Intercept</i>	<i>Slope</i>	<i>R</i>
0	260	1.0305	-6.4649	0.96
	270	1.0459	-8.2289	0.96
	280	1.0705	-10.3957	0.96
	290	1.1094	-13.0997	0.95
	300	1.1704	-16.5690	0.95
	310	1.2677	-21.2100	0.94
	320	1.4271	-27.7805	0.92
15	260	1.0314	-6.7290	0.96
	270	1.0475	-8.5701	0.96
	280	1.0732	-10.8368	0.96
	290	1.1138	-13.6752	0.95
	300	1.1779	-17.3350	0.95
	310	1.2806	-22.2652	0.94
	320	1.4501	-29.3100	0.92
30	260	1.0345	-7.6413	0.96
	270	1.0528	-9.7519	0.96
	280	1.0823	-12.3709	0.96
	290	1.1293	-15.6892	0.95
	300	1.2044	-20.0418	0.95
	310	1.3268	-26.0479	0.93
	320	1.5341	-34.8991	0.91
45	260	1.0415	-9.7227	0.96
	270	1.0651	-12.4662	0.96
	280	1.1036	-15.9315	0.95
	290	1.1659	-20.4408	0.95
	300	1.2683	-26.5889	0.94
	310	1.4425	-35.5392	0.92
	320	1.7537	-49.5497	0.88
60	260	1.0592	-14.9362	0.96
	270	1.0965	-19.3768	0.96
	280	1.1591	-25.2359	0.95
	290	1.2654	-33.3757	0.94
	300	1.4535	-45.5687	0.92
	310	1.8064	-65.4639	0.87
	320	2.3806	-91.9728	0.69

Table B.4: Regression coefficients and correlation coefficient R for the relation between $TISIE_a$ and at-ground radiance ratio L_1^{grd}/L_2^{grd} (Eq. (5.18), (5.34)) for the US-standard atmosphere

MLS				
θ_s [°]	T_s [K]	<i>Intercept</i>	<i>Slope</i>	<i>R</i>
0	260	1.0390	-5.2458	0.76
	270	1.0511	-6.6412	0.76
	280	1.0705	-8.3492	0.75
	290	1.1010	-10.4657	0.75
	300	1.1484	-13.1461	0.73
	310	1.2226	-16.6479	0.72
	320	1.3400	-21.3800	0.68
15	260	1.0398	-5.4643	0.76
	270	1.0524	-6.9220	0.76
	280	1.0727	-8.7100	0.75
	290	1.1045	-10.9327	0.74
	300	1.1543	-13.7602	0.73
	310	1.2326	-17.4758	0.71
	320	1.3570	-22.5251	0.68
30	260	1.0423	-6.2209	0.76
	270	1.0568	-7.8965	0.76
	280	1.0801	-9.9675	0.75
	290	1.1170	-12.5703	0.74
	300	1.1754	-15.9325	0.73
	310	1.2685	-20.4373	0.71
	320	1.4184	-26.6579	0.66
45	260	1.0482	-7.9560	0.76
	270	1.0670	-10.1468	0.76
	280	1.0975	-12.9012	0.75
	290	1.1467	-16.4501	0.74
	300	1.2264	-21.1937	0.72
	310	1.3575	-27.8091	0.68
	320	1.5705	-36.9421	0.61
60	260	1.0629	-12.3434	0.76
	270	1.0931	-15.9321	0.75
	280	1.1434	-20.6395	0.74
	290	1.2280	-27.0861	0.72
	300	1.3735	-36.4033	0.69
	310	1.6217	-49.7997	0.60
	320	1.6811	-45.6958	0.29

Table B.5: Regression coefficients and correlation coefficient R for the relation between $TISIE_b$ and at-ground radiance ratio L_1^{grad}/L_2^{grad} (Eq. (5.19), (5.34)) for the mid latitude summer standard atmosphere

TROP				
θ_s [°]	T_s [K]	<i>Intercept</i>	<i>Slope</i>	<i>R</i>
0	260	1.0403	-5.4776	0.77
	270	1.0528	-6.9209	0.76
	280	1.0729	-8.6960	0.76
	290	1.1047	-10.9105	0.75
	300	1.1545	-13.7419	0.74
	310	1.2333	-17.4931	0.72
	320	1.3599	-22.6746	0.69
15	260	1.0411	-5.7091	0.77
	270	1.0542	-7.2182	0.76
	280	1.0752	-9.0788	0.76
	290	1.1085	-11.4083	0.75
	300	1.1609	-14.4016	0.74
	310	1.2442	-18.3940	0.72
	320	1.3789	-23.9501	0.69
30	260	1.0438	-6.5120	0.77
	270	1.0588	-8.2526	0.76
	280	1.0832	-10.4167	0.76
	290	1.1219	-13.1596	0.75
	300	1.1837	-16.7459	0.74
	310	1.2836	-21.6408	0.71
	320	1.4484	-28.6115	0.67
45	260	1.0500	-8.3610	0.77
	270	1.0697	-10.6529	0.76
	280	1.1018	-13.5579	0.75
	290	1.1540	-17.3451	0.74
	300	1.2396	-22.4973	0.73
	310	1.3835	-29.8921	0.69
	320	1.6272	-40.6613	0.62
60	260	1.0659	-13.0699	0.77
	270	1.0979	-16.8844	0.76
	280	1.1517	-21.9595	0.75
	290	1.2437	-29.0636	0.73
	300	1.4066	-39.7202	0.70
	310	1.7010	-56.2268	0.61
	320	1.7394	-49.6878	0.26

Table B.6: Regression coefficients and correlation coefficient R for the relation between $TISIE_b$ and at-ground radiance ratio L_1^{grd}/L_2^{grd} (Eq. (5.19), (5.34)) for the tropical standard atmosphere

MLW				
θ_s [°]	T_s [K]	<i>Intercept</i>	<i>Slope</i>	<i>R</i>
0	260	1.0368	-4.8228	0.75
	270	1.0481	-6.1275	0.75
	280	1.0661	-7.7115	0.75
	290	1.0942	-9.6520	0.74
	300	1.1373	-12.0706	0.73
	310	1.2038	-15.1586	0.71
	320	1.3064	-19.1896	0.67
15	260	1.0375	-5.0176	0.75
	270	1.0493	-6.3780	0.75
	280	1.0680	-8.0324	0.74
	290	1.0973	-10.0645	0.74
	300	1.1425	-12.6062	0.72
	310	1.2124	-15.8654	0.70
	320	1.3203	-20.1334	0.67
30	260	1.0397	-5.6896	0.75
	270	1.0532	-7.2438	0.75
	280	1.0746	-9.1453	0.74
	290	1.1083	-11.5016	0.73
	300	1.1607	-14.4842	0.72
	310	1.2425	-18.3625	0.70
	320	1.3698	-23.4749	0.65
45	260	1.0448	-7.2175	0.75
	270	1.0621	-9.2224	0.75
	280	1.0898	-11.7089	0.74
	290	1.1338	-14.8505	0.73
	300	1.2036	-18.9302	0.71
	310	1.3148	-24.3709	0.67
	320	1.4858	-31.3624	0.60
60	260	1.0576	-11.0186	0.75
	270	1.0845	-14.2064	0.74
	280	1.1286	-18.2903	0.73
	290	1.2010	-23.6863	0.71
	300	1.3204	-31.0505	0.67
	310	1.5093	-40.6655	0.59
	320	1.6077	-40.5822	0.34

Table B.7: Regression coefficients and correlation coefficient R for the relation between $TISIE_b$ and at-ground radiance ratio L_1^{grd}/L_2^{grd} (Eq. (5.19), (5.34)) for the mid latitude winter standard atmosphere

US				
θ_s [°]	T_s [K]	<i>Intercept</i>	<i>Slope</i>	<i>R</i>
0	260	1.0374	-4.9446	0.75
	270	1.0490	-6.2757	0.75
	280	1.0674	-7.8955	0.75
	290	1.0961	-9.8861	0.74
	300	1.1405	-12.3783	0.73
	310	1.2091	-15.5805	0.71
	320	1.3157	-19.7998	0.68
15	260	1.0381	-5.1461	0.75
	270	1.0502	-6.5347	0.75
	280	1.0694	-8.2276	0.75
	290	1.0994	-10.3138	0.74
	300	1.1459	-12.9356	0.73
	310	1.2181	-16.3201	0.71
	320	1.3305	-20.7967	0.67
30	260	1.0405	-5.8418	0.75
	270	1.0542	-7.4310	0.75
	280	1.0762	-9.3809	0.75
	290	1.1108	-11.8065	0.74
	300	1.1648	-14.8942	0.72
	310	1.2497	-18.9421	0.70
	320	1.3831	-24.3439	0.65
45	260	1.0458	-7.4273	0.75
	270	1.0635	-9.4849	0.75
	280	1.0920	-12.0465	0.74
	290	1.1374	-15.3005	0.73
	300	1.2099	-19.5594	0.71
	310	1.3264	-25.3074	0.67
	320	1.5080	-32.8269	0.60
60	260	1.0591	-11.3880	0.75
	270	1.0869	-14.6858	0.74
	280	1.1327	-18.9379	0.73
	290	1.2084	-24.6106	0.71
	300	1.3345	-32.4704	0.68
	310	1.5377	-42.9779	0.59
	320	1.6286	-42.0315	0.32

Table B.8: Regression coefficients and correlation coefficient R for the relation between $TISIE_b$ and at-ground radiance ratio L_1^{grd}/L_2^{grd} (Eq. (5.19), (5.34)) for the US-standard atmosphere

Appendix C

Further Results of “TISIE”-Approach

This Appendix contains:

- plots of the retrieval errors in relation to solar zenith angles for the tropical standard atmosphere (Fig. C.1, C.2, C.3)
- plots of the retrieval errors in relation to solar zenith angles for the mid latitude winter standard atmosphere (Fig. C.4, C.5, C.6)
- plots of the retrieval errors in relation to solar zenith angles for the US-standard atmosphere (Fig. C.7, C.8, C.9)

- plots of the frequency distribution of errors on the retrieved surface parameters (Fig. C.10, C.11, C.12)

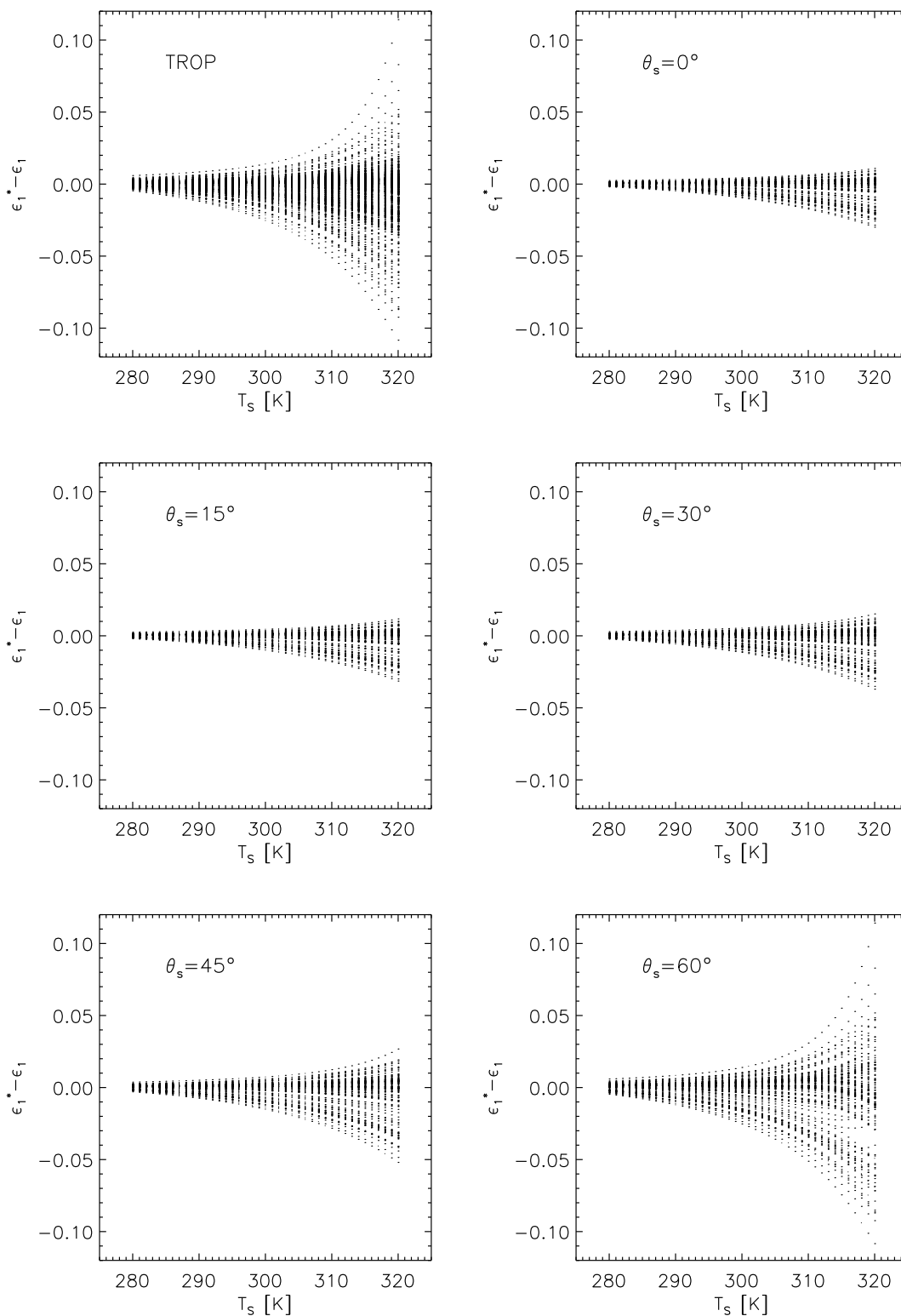


Figure C.1: MIR emissivity retrieval errors in relation to surface temperatures and solar zenith angles for the tropical standard atmosphere

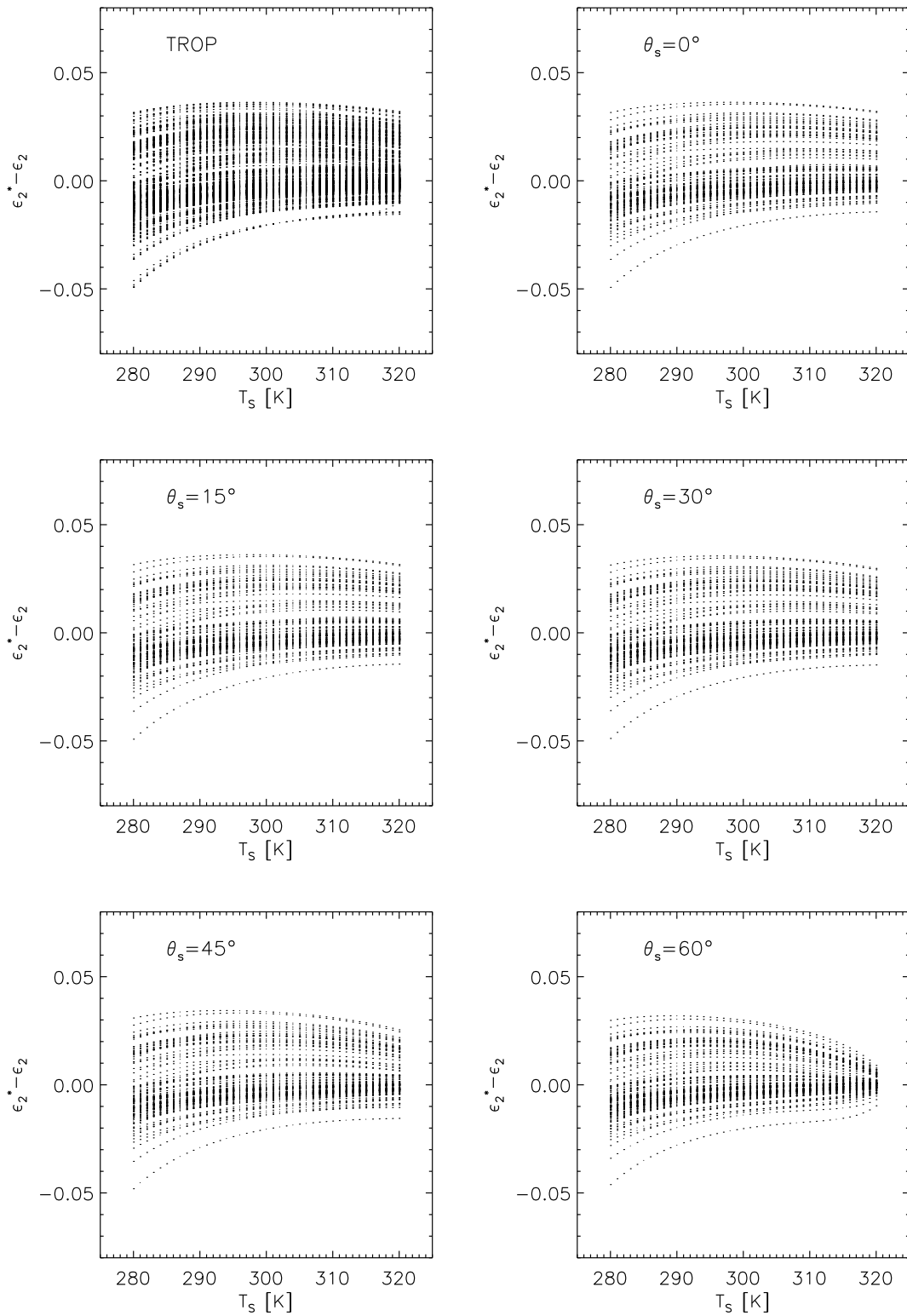


Figure C.2: TIR emissivity retrieval errors in relation to surface temperatures and solar zenith angles for the tropical standard atmosphere

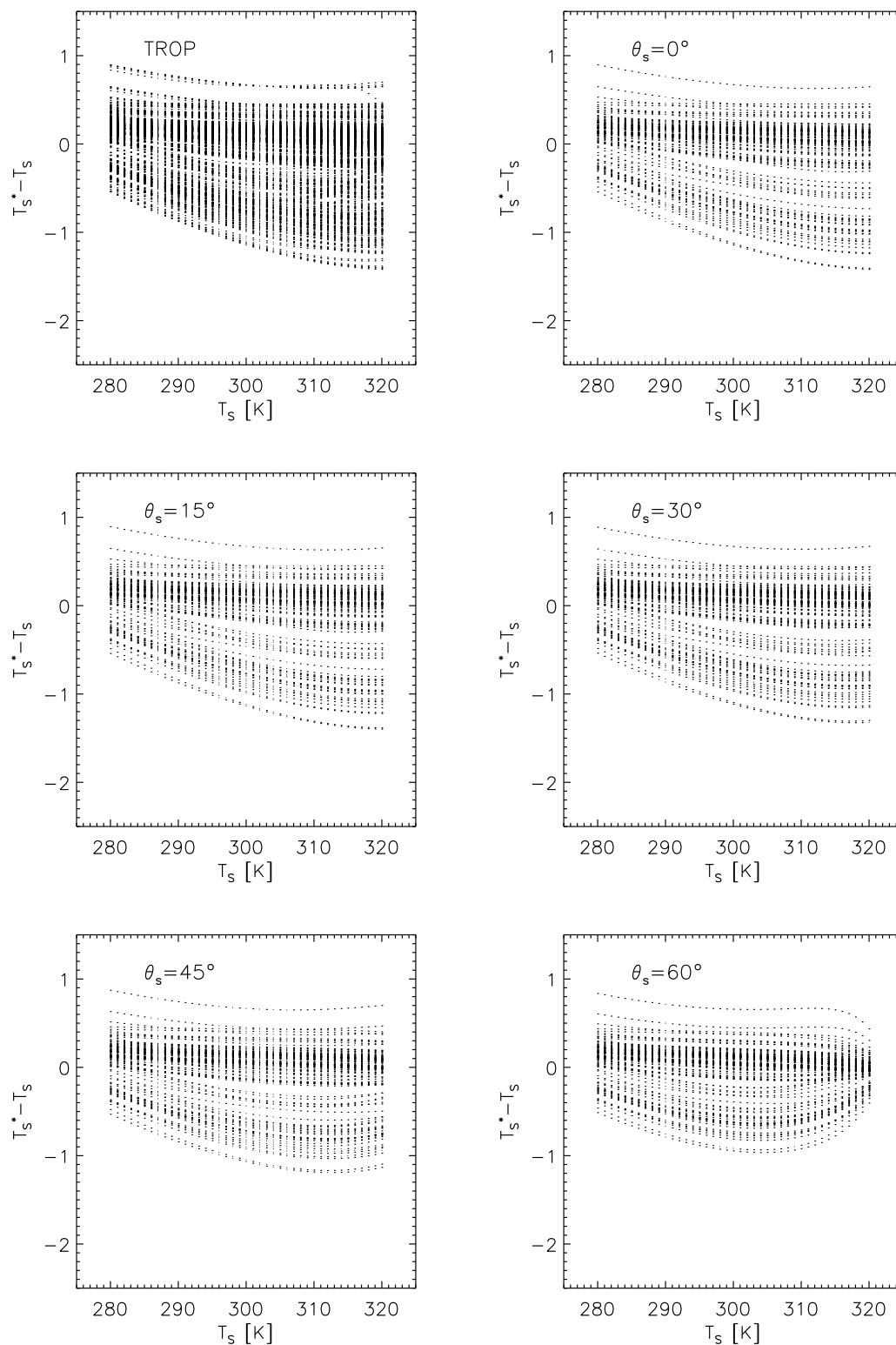


Figure C.3: Temperature retrieval errors in relation to surface temperatures and solar zenith angles for the tropical standard atmosphere

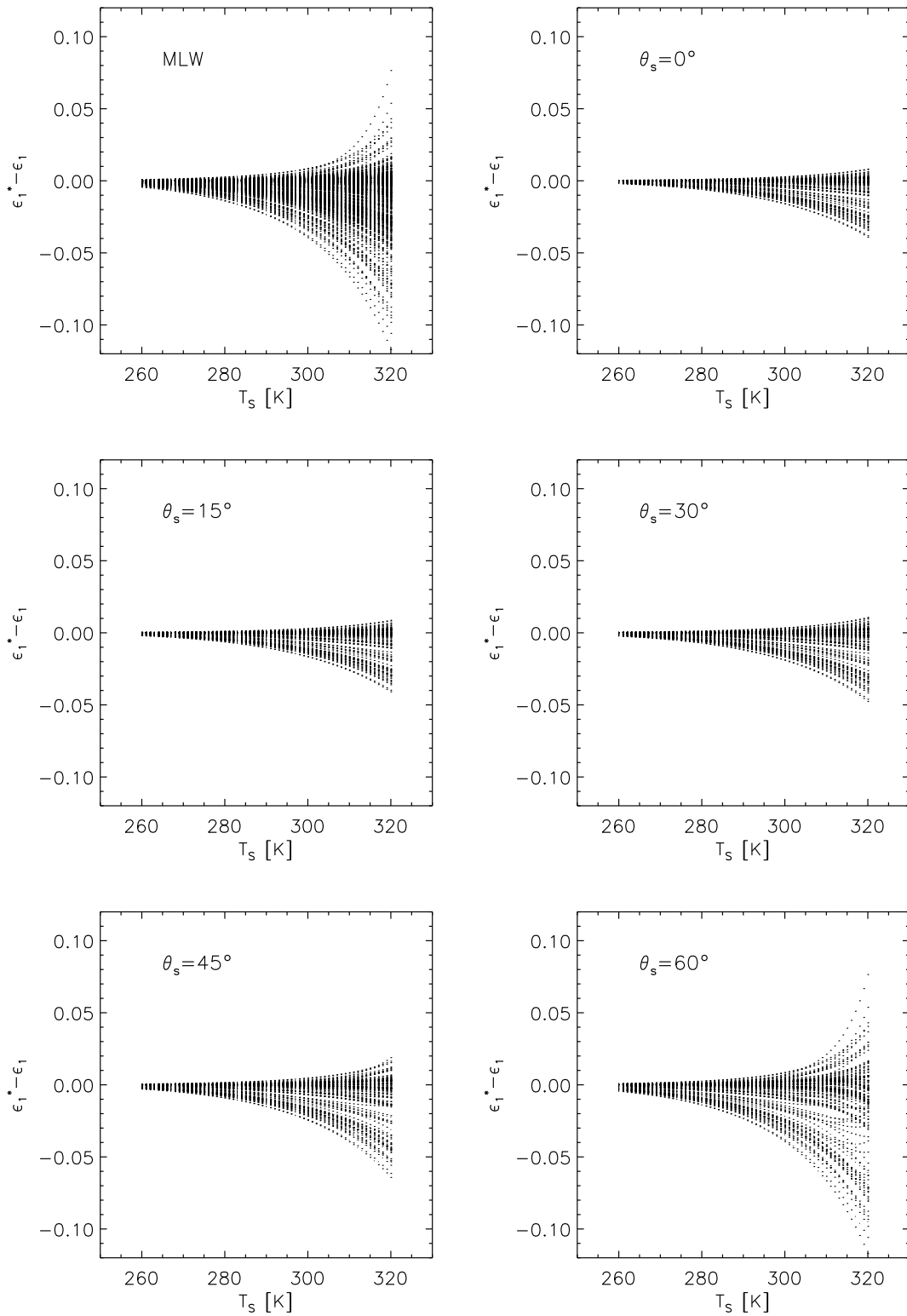


Figure C.4: MIR emissivity retrieval errors in relation to surface temperatures and solar zenith angles for the mid latitude winter standard atmosphere

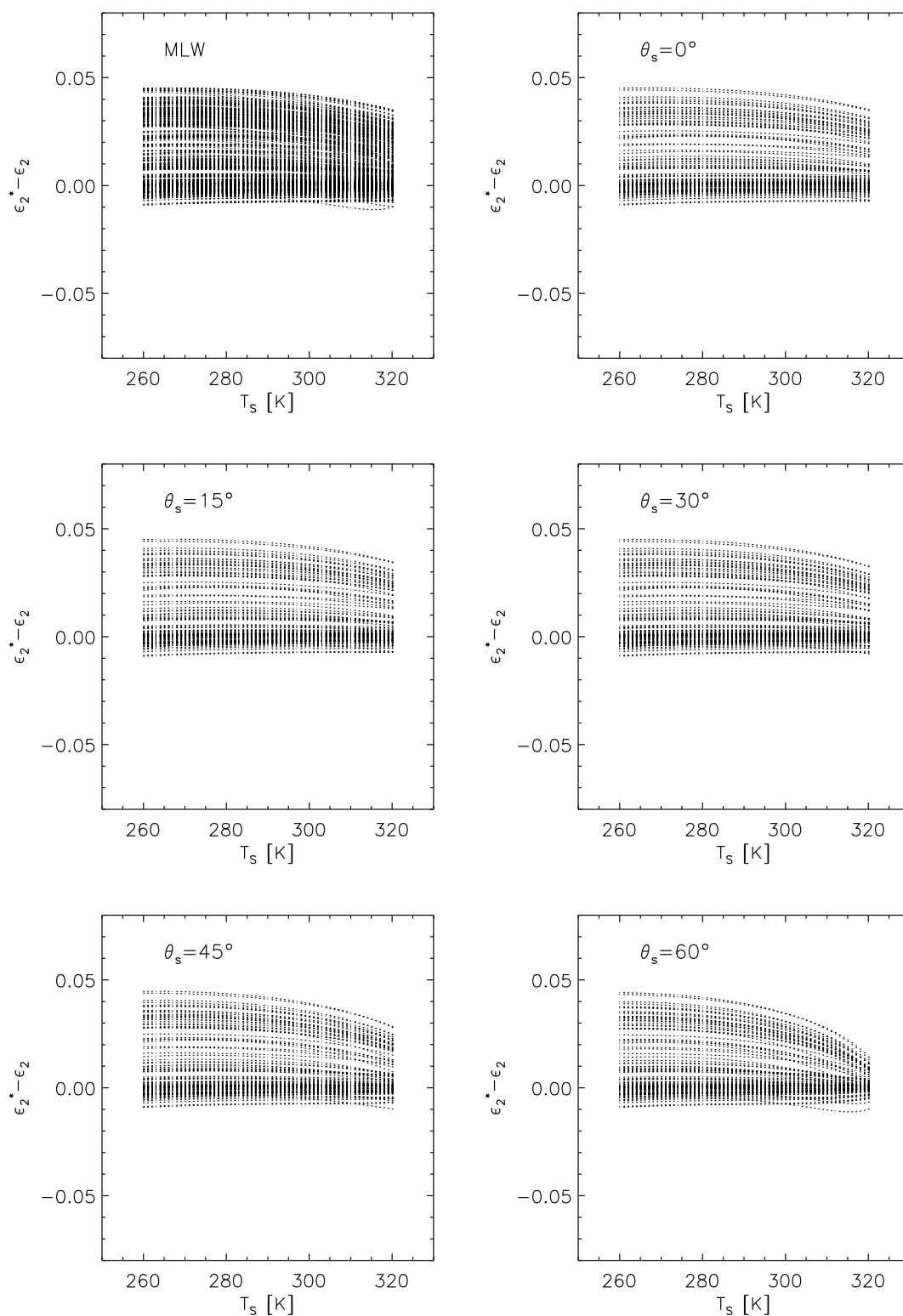


Figure C.5: TIR emissivity retrieval errors in relation to surface temperatures and solar zenith angles for the mid latitude winter standard atmosphere

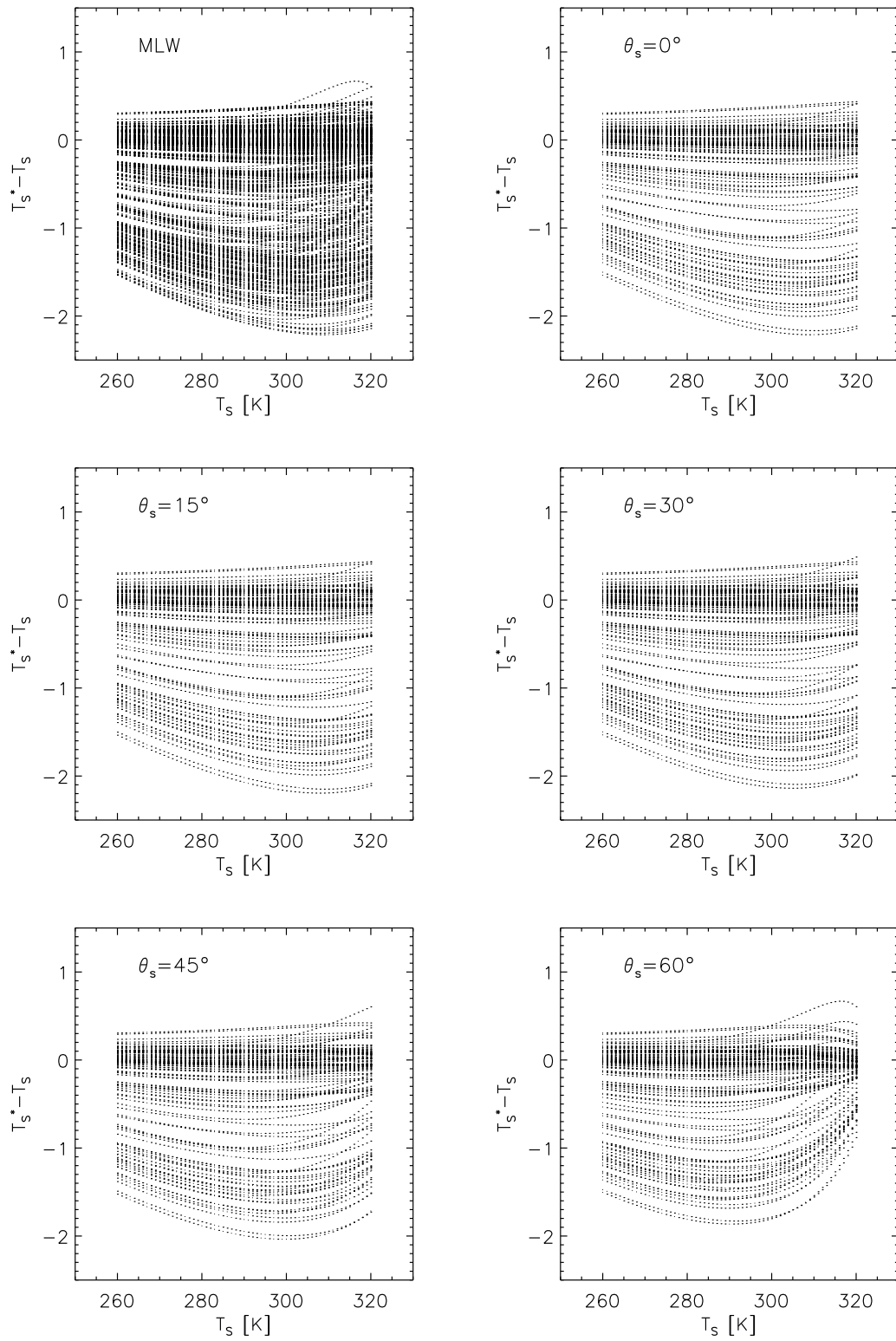


Figure C.6: Temperature retrieval errors in relation to surface temperatures and solar zenith angles for the mid latitude winter standard atmosphere

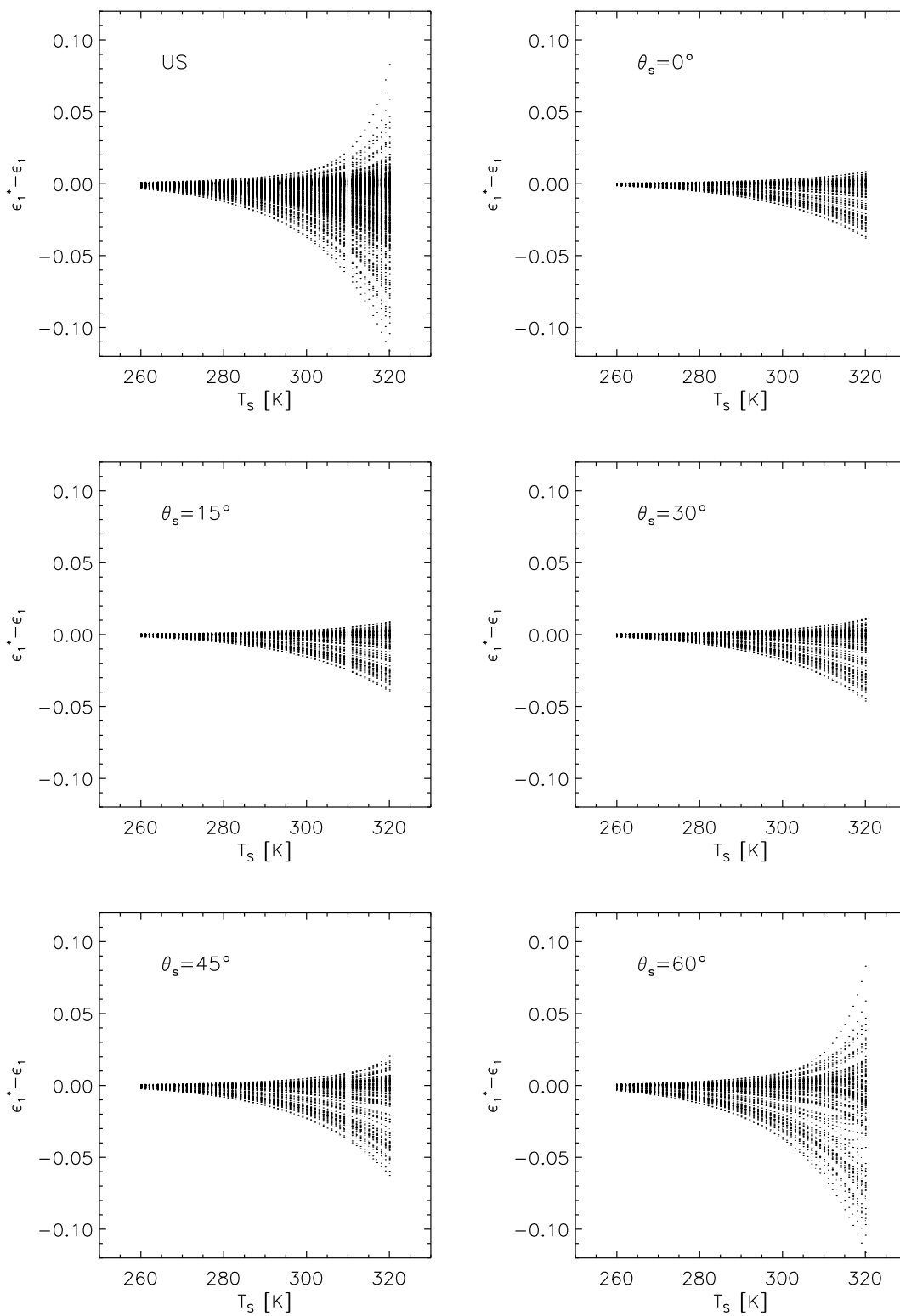


Figure C.7: MIR emissivity retrieval errors in relation to surface temperatures and solar zenith angles for the US-standard atmosphere

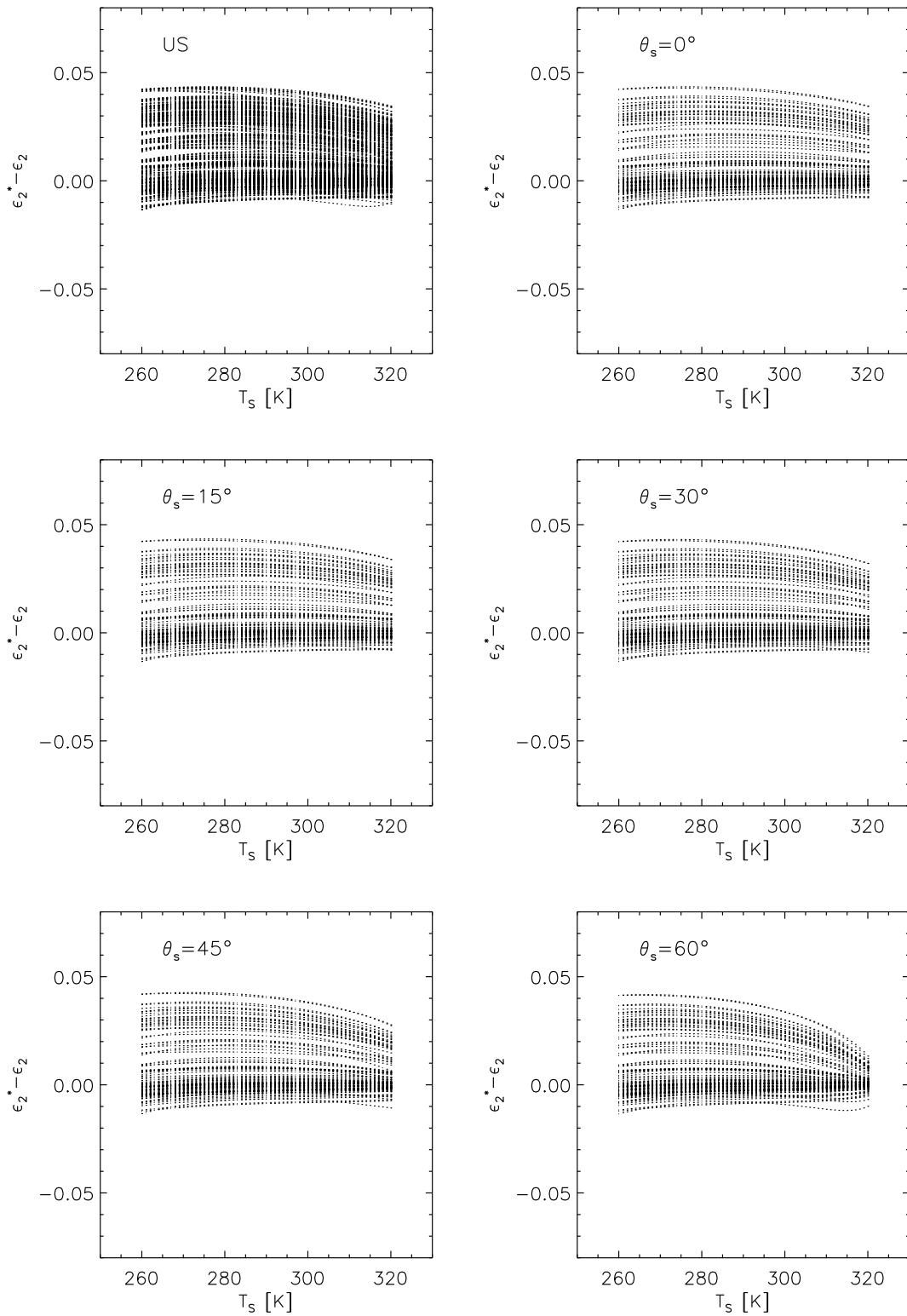


Figure C.8: TIR emissivity retrieval errors in relation to surface temperatures and solar zenith angles for the US-standard atmosphere

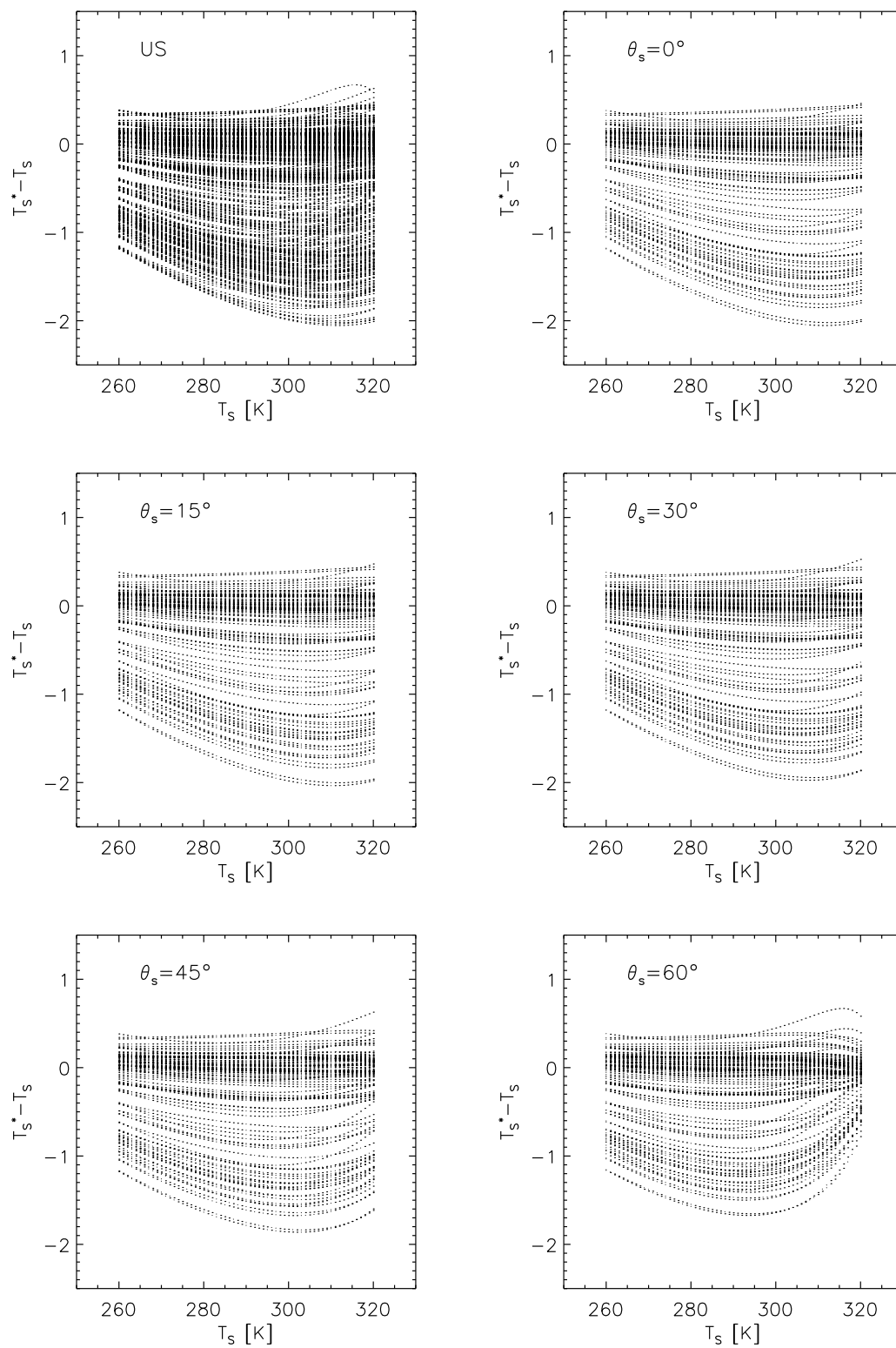


Figure C.9: Temperature retrieval errors in relation to surface temperatures and solar zenith angles for the US-standard atmosphere

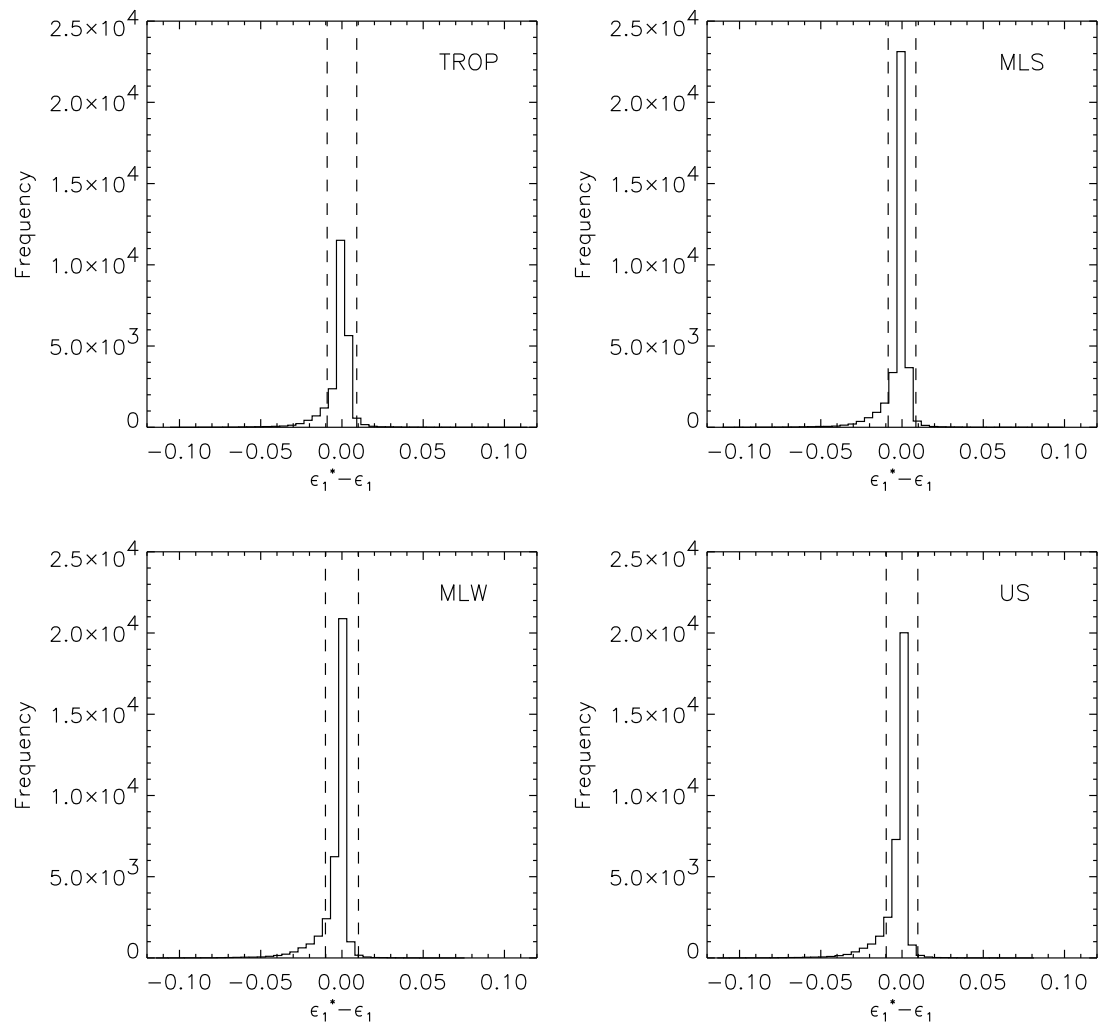


Figure C.10: Frequency distribution of errors on the retrieved MIR emissivity using sub-data sets according to standard atmospheres

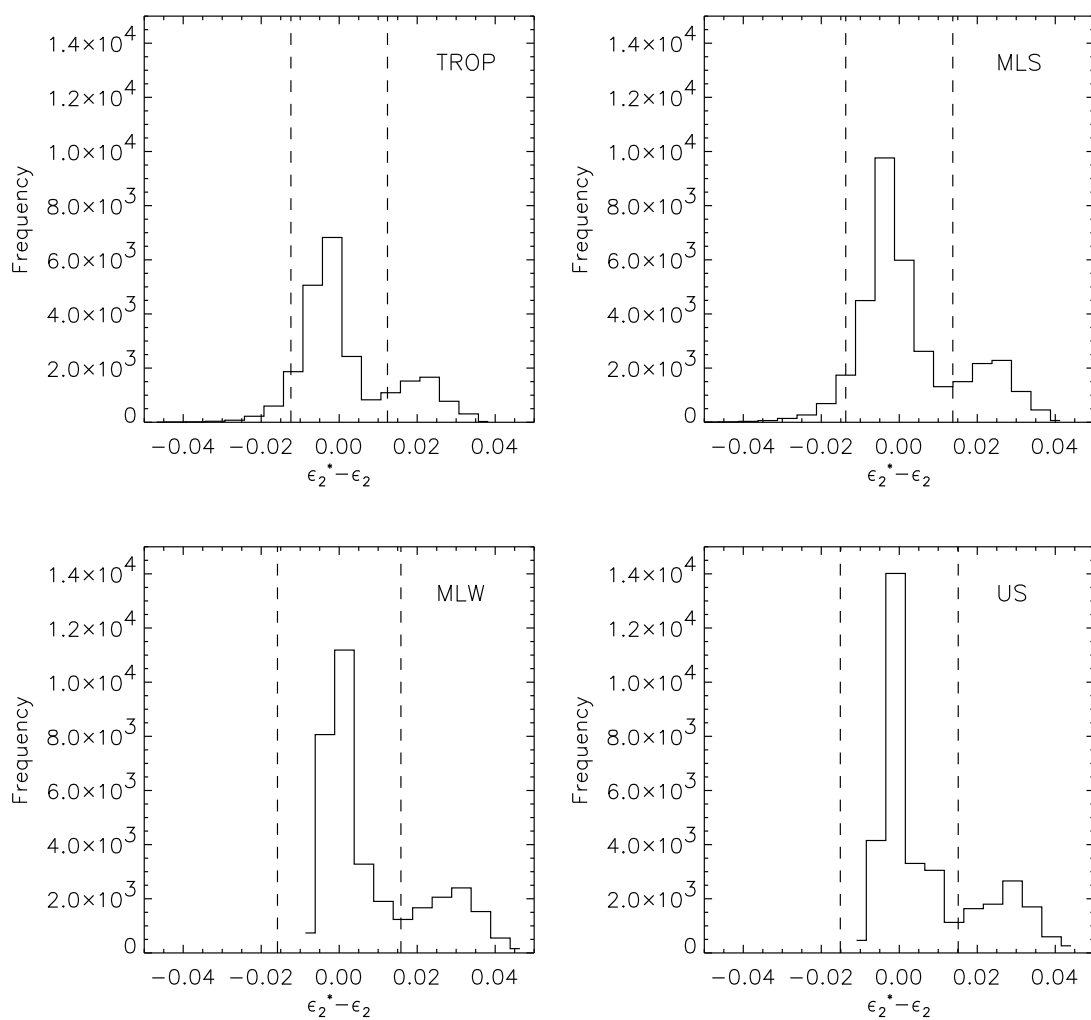


Figure C.11: Frequency distribution of errors on the retrieved TIR emissivity using sub-data sets according to standard atmospheres

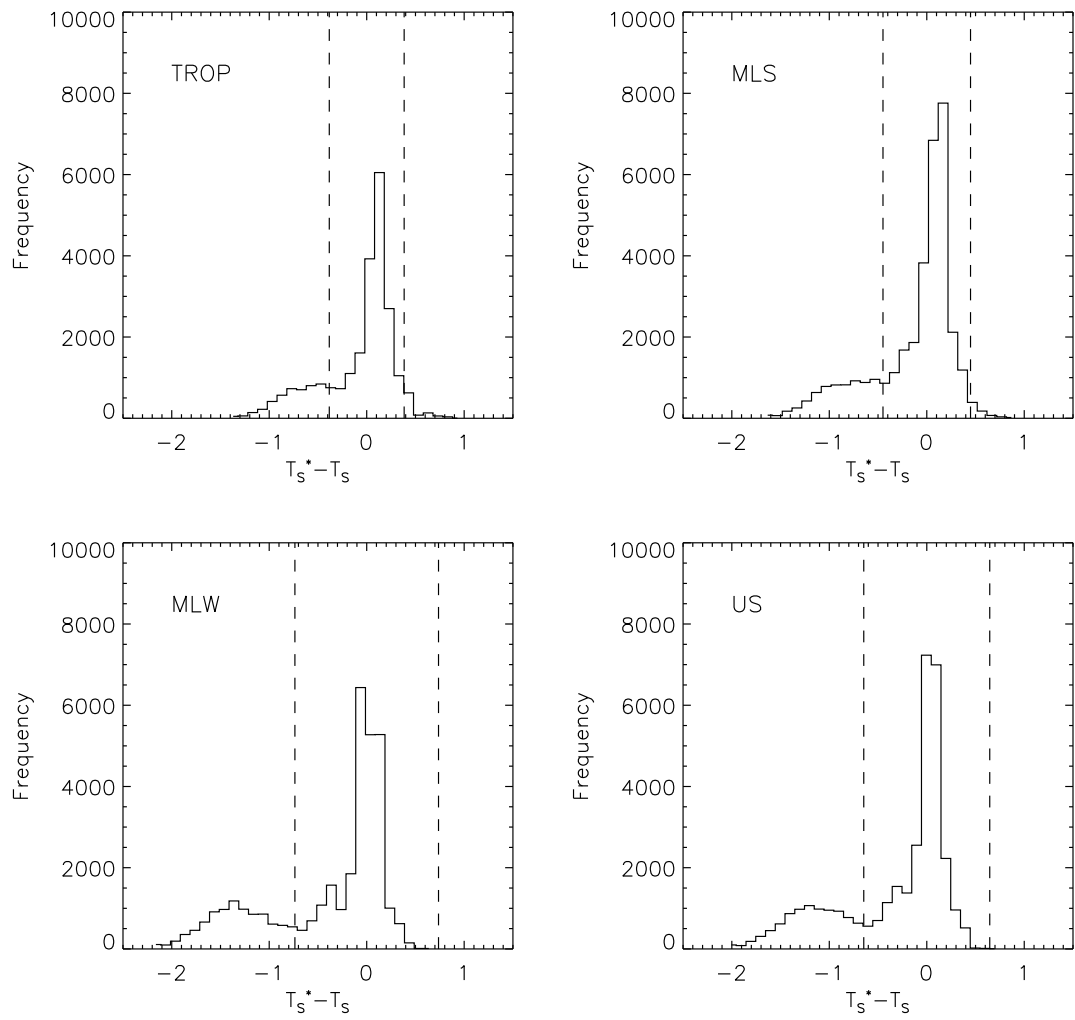


Figure C.12: Frequency distribution of errors on the retrieved surface temperature using sub-data sets according to standard atmospheres

References

- Abreu, L., Chetwynd, J., Anderson, G., & Kimball, L. (1995). *MODTRAN 3 Scientific Report. Draft Preprint*. Technical report, Geophysics Laboratory, Air Force Command, US Air Force, Hanscom AFB, MA, USA.
- Barton, I., Zavody, A., O'Brien, D., Cutten, D., Saunders, R., & Llewellyn-Jones, D. (1989). Theoretical algorithms for satellite-derived sea surface temperatures. *J. Geophys. Res.*, 94(3), 3365–3375.
- Becker, F. & Li, Z.-L. (1990a). Temperature-Independent Spectral Indices in thermal infrared bands. *Remote Sens. Environ.*, 32, 17–33.
- Becker, F. & Li, Z.-L. (1990b). Towards a local split window method over land surfaces. *Int. J. Remote Sensing*, 11(3), 369–393.
- Becker, F. & Li, Z.-L. (1995). Surface temperature and emissivity at various scales: definition, measurements and related problems. *Remote Sensing Reviews*, 12, 225–253.
- Berk, A., Bernstein, L., & Robertson, D. (1989). *MODTRAN: A Moderate Resolution Model for LOWTRAN 7*. Technical Report GL-TR-89-0122, Air Force Geophysics Laboratory.
- Brieß et al. (1997). *BIRD - Phase B Report, Mission Science & Technical Plan*. Technical report, German Aerospace Center (DLR - Deutsches Zentrum für Luft- und Raumfahrt), Institute of Space Sensor Technology and Planetary Exploration.
- Brieß et al. (1999). The DLR small satellite mission BIRD. In *Small satellites for Earth Observation*, Digest of the 2nd International Symposium of the International Academy of Astronautics (IAA), Berlin: Wissenschaft & Technik Verlag.
- Chedin, A., Scott, N., & Berroir, A. (1982). A single-channel, double viewing angle method for sea surface temperature determination from coincident METEOSAT and TIROS-N radiometric measurements. *J. Appl. Meteor.*, 9, 715–727.
- Coll, C., Caselles, V., Sobrino, J., & Valor, E. (1994). On the atmospheric dependence of the split-window equation for land surface temperature. *Int. J. Remote Sensing*, 15(1), 105–122.

- de Griend, A. V. & Owe, M. (1993). On the relationship between thermal emissivity and normalized difference vegetation index for natural surfaces. *Int. J. Remote Sensing*, 14(6), 1119–1131.
- Deschamps, P. & Phulpin, T. (1980). Atmospheric correction of infrared measurements of sea surface temperature using at 3.7, 11, and 12 μm . *Boundary-Layer Meteorology*, 18, 131–143.
- Elliott, W. & Gaffen, D. (1991). On the utility of radiosonde humidity archive for climate studies. *Bulletin American Meteorological Society*.
- Feigelson, E. (1984). *Radiation in a Cloudy Atmosphere*. Dordrecht, Holland: D. Reidel Publishing Company.
- Francois, C. & Ottlé, C. (1996). Atmospheric corrections in the thermal infrared: Global and water vapor dependent split-window algorithms - Applications to ATSR and AVHRR data. *IEEE Trans. Geosci. Remote Sensing*, 34(2), pp. 457.
- Gaffen, D., Elliott, W., & Robock, A. (1992). Relationship between tropospheric water vapor and surface temperature as observed by radiosondes. *Geophysical Research Letters*.
- Goita, K. & Royer, A. (1997). Surface temperature and emissivity separability over land surface from combined TIR and SWIR AVHRR. *IEEE Trans. Geosci. Remote Sensing*, 35(3), 718–733.
- Kerr, Y., Lagouarde, J., & Imbernon, J. (1992). Accurate land surface temperature retrieval from AVHRR data with use of an improved split window algorithm. *Remote Sens. Environ.*, 41, 197–209.
- Labeled, J., Li, Z.-L., & Stoll, M. (1993). Land surface temperature retrieval from ATSR over the NIAMEY (Niger) area. In *Proceedings Second ERS-1 Symposium - Space at the Service of our Environment*, Esa Sp-361 (January 1994) (pp. 389). Hamburg, Germany.
- Lenoble, J. (1993). *Atmospheric Radiative Transport*. Hampton, Virginia USA: A. Deepak.
- Li, Z.-L. & Becker, F. (1993). Feasibility of land surface temperature and emissivity determination from AVHRR data. *Remote Sens. Environ.*, 43, 67–85.
- Lion, K. (1980). *An Introduction to Atmospheric Radiation*. Academic Press.
- Lippert, K. (1995). Bestimmung von Landoberflächentemperaturen aus Flugzeug- und Satellitendaten. Diplomarbeit, Humboldt-Universität zu Berlin, Institut für Physik - Meteorologie.

- Lippert, K. (2000). Temperature Retrieval Approaches for Upcoming BIRD Data. internal report (on request), German Aerospace Center (DLR - Deutsches Zentrum für Luft- und Raumfahrt), Institute of Space Sensor Technology and Planetary Exploration, Berlin, Germany.
- Lippert, K., Borel, C., & Gerstl, S. (1996). MISR TOA albedo retrieval for clear sky scenes. interim report (on request), Los Alamos National Laboratory, Los Alamos, New Mexico, USA.
- McMillin, L. (1975). Estimation of sea surface temperature from two infrared window measurements with different absorption. *J. Geophys. Res.*, 80, 5113–5117.
- McMillin, L. & Crosby, D. (1984). Theory and validation of the multiple window sea surface temperature technique. *J. Geophys. Res.*, C9(89), 3655–3661.
- Norman, J. & Becker, F. (1995). Terminology in thermal infrared remote sensing of natural surface. *Remote Sensing Reviews*, 12, 159–173.
- Ottlé, C. & Stoll, M. (1993). Effect of atmospheric absorption and surface emissivity on the determination of land surface temperature from infrared satellite data. *Int. J. Remote Sensing*, 14(10), 19–34.
- Ottlé, C. & Vidal-Madjar, D. (1992). Estimation of land surface temperature with NOAA9 data. *Remote Sens. Environ.*, 40, 27–41.
- Prata, A. (1993). Land surface temperature derived from the Advanced Very High Resolution Radiometer and the Along-Track Scanning Radiometer 1. Theory. *J. Geophys. Res.*, 98(D9), 16689–16702.
- Prata, A. (1994a). Land surface temperature derived from the Advanced Very High Resolution Radiometer and the Along-Track Scanning Radiometer, 2. Experimental results and validation of AVHRR algorithm. *J. Geophys. Res.*, 99(D6), pp. 13025.
- Prata, A. (1994b). Land surface temperature determination from satellites. *Adv. Space Res.*, 14(3), 15–26.
- Prata, A., Caselles, V., & Ottlé, C. (1995). Thermal remote sensing of land surface temperature from satellites: Current status and future prospects. *Remote Sensing Reviews*, 12(3/4), pp. 175.
- Prata, A., Cechet, R., Barton, I., & Llewellyn-Jones, D. (1990). The Along Track Scanning Radiometer for ERS-1-scan geometry and data simulation. *IEEE Trans. Geosci. Remote Sensing*, 28(1), 3–13.
- Price, J. (1983). Estimating surface temperatures from satellite thermal infrared data: A simple formulation for the atmospheric effect. *Remote Sens. Environ.*, 13, 353–361.

- Price, J. (1984). Land surface temperature measurements from the split window channels of the NOAA 7 Advanced Very High Resolution Radiometer. *J. Geophys. Res.*, 89(D5), 7231–7237.
- RSI (1999). IDL - *Interactive Data Language*. Research Systems, Inc., Boulder, USA. <http://www.rsinc.com>.
- Salisbury, J. & D’Aria, D. (1992a). Emissivity of terrestrial material in the 8 – 14 μm atmospheric window. *Remote Sens. Environ.*, 42, 83–106.
- Salisbury, J. & D’Aria, D. (1992b). Infrared (8 – 14 μm) remote sensing of soil particle size. *Remote Sens. Environ.*, 42, 157–165.
- Salisbury, J. & D’Aria, D. (1994). Emissivity of terrestrial material in the 3 – 5 μm atmospheric window. *Remote Sens. Environ.*, 47, 345–361.
- Shettle, E. (2000). Personal communication.
- Skrbek, W. (1999). Personal communication.
- Sobrino, J., Coll, C., & Caselles, V. (1991). Atmospheric correction for land surface temperature using NOAA-11 AVHRR channels 4 and 5. *Remote Sens. Environ.*, 38, 19–34.
- Sobrino, J., Li, Z.-L., & Becker, F. (1996). Multi-channel and multi-angle algorithms for estimating sea and land surface temperature with ATSR data. *Int. J. Remote Sensing*, 17(11), pp. 2089.
- Sobrino, J., Li, Z.-L., Stoll, M., & Becker, F. (1994). Improvements in the split-window technique for land surface temperature determination. *IEEE Trans. Geosci. Remote Sensing*, 32(2), 243–253.
- Sutherland, R. & Bartholic, J. (1977). Significance of vegetation in interpreting thermal radiation from terrestrial surface. *J. Appl. Meteor.*, 16(8), 759–763.
- Ulivieri, C., Castronuovo, M., Francioni, R., & Cardillo, A. (1994). A split window algorithm for estimating land surface temperature from satellites. *Adv. Space Res. D*, 14(3), 59–65.
- Vass, P. & Battrick, B. (1992). ERS-1 SYSTEM. Technical Report ESA SP-1146, European Space Agency.
- Villeneuve, P. V. (1996). A Numerical Study of the Sensitivity of Cloudy-Scene Bidirectional Reflectivity Distribution Functions to Variations in Cloud Parameters. PhD thesis, Virginia Polytechnic Institute and State University, USA.
- Walter et al. (1999). BIRD - a microsatellite for hot spot detection. In *The 13th Annual AIAA, Conference on Small Satellites* Logan, Utah, USA: Utah State University.

-
- Wan, Z. & Dozier, J. (1989). Land surface temperature measurements from space: physical principles and inverse modeling. *IEEE Trans. Geosci. Remote Sensing*, 27(3), 268–278.
- Wan, Z. & Li, A.-L. (1997). A physics-based algorithm for retrieving land surface emissivity and temperature from EOS/MODIS data. *IEEE Trans. Geosci. Remote Sensing*, 35(4), 980–996.
- Wan, Z. & Snyder, W. (1999). MODIS: Land Surface Temperature - Algorithm Theoretical Basic Document. <http://eosps0.gsfc.nasa.gov/atbd/modistables.html>. ATBD-MOD-11.
- Zhukov, B., Oertel, D., Jahn, H., & Lorenz, E. (1997). Modelling of Detection and Analysis of High-Temperature Events (HTE) for the Bi-spectral InfraRed detection (BIRD) Mission: Airborne Remote Sensing of Artificial Fires, Development of Algorithm and of Requirements. Technical report, German Aerospace Center (DLR). internal report.

Symbols

Variable	Unit	Description
i		index for BIRD channels: 1-MIR, 2-TIR (channel-integrated)
j		index for the subset data set used for the “Regression” - Approach
a_i		fitting coefficients of the bi-spectral regression (“Regression” - Approach)
b, c		fitting coefficients used within “Regression” - Approach
α_i, n_i		fitting coefficients used within “TISIE” - Approach
ref		index for the reference model
$pert$		index for the perturbed model
aer, A, AV		aerosol amount defined as used in MODTRAN = total vertical aerosol optical depth at 550 nm (nadir view)
f_{r_i}		spectral response function for channel i
$B_i(T)$	$[W/(m^2 sr \mu m)]$ $[W/(m^2 sr cm^{-1})]$	channel-integrated blackbody radiance according to a temperature T
$B_i(T_{B,i}^{grd})$		channel-integrated blackbody radiance according to the at-ground brightness temperature $T_{B,i}^{grd}$
$B_i(T_i)$		channel-integrated blackbody radiance according to the at-sensor (TOA) brightness temperature T_i
$B_i(T_S)$		channel-integrated blackbody radiance according to the surface temperature T_S
$B_i^*(T_S)$		approximated channel-integrated blackbody radiance according to the surface temperature T_S
$B_i^{-1}(x)$		channel-integrated inverse blackbody radiance according to the expression x
E_i^{sun}	$[W/(m^2 \mu m)]$	channel-integrated solar irradiance
I		coefficient (intercept) of TISIE - regression

$L_i^{atm\downarrow}$	$[W/(m^2 sr \mu m)]$ $[W/(m^2 sr cm^{-1})]$	channel-integrated hemispheric average downwelling atmospheric radiance (solar dif- fuse and thermal)
$L_i^{atm\uparrow}$		channel-integrated directional upwelling at- mospheric solar and thermal radiance
$L_i^{grd}(T_{B,i}^{grd})$		channel-integrated ground radiance accord- ing to the at-ground brightness temperature $T_{B,i}^{grd}$
$L_{i,n}^{grd}$		channel-integrated ground radiance for nighttime conditions
L_i^{toa}		channel-integrated top-of-atmosphere radi- ance
L_{S_i}		channel-integrated emitted radiance of the surface
N_j		number of considered coupled atmospheric and surface models within subset j
R		correlation coefficient for <i>TISIE</i> - regression
S		coefficient (slope) of <i>TISIE</i> - regression
T^{ATM}	$[K]$	atmospheric profile temperature
T_{bound}^{ATM}		atmospheric boundary temperature
$T_{B,i}^S$		brightness temperature according the surface emission for channel i
$T_{B,i}^{grd}$		at-ground brightness temperature for chan- nel i
T_i		TOA brightness temperature for channel i
T_S		surface temperature
T_S^*		estimated surface temperature
T_S^{**}		estimated surface temperature before apply- ing emissivity corrections ("Regression" - Approach)
T_0^{**}		estimated "offset"-temperature (2nd step of emissivity correction within the "Regres- sion" - Approach)
T_S^{ATM}		surface temperature retrieved with a certain standard atmosphere <i>ATM</i>
T_S^{ref}		surface temperature retrieved with the refer- ence model
T_S^{pert}		surface temperature retrieved with a per- turbed model
<i>TISIE</i>		ratio of channel-integrated emissivity
<i>TISIB</i>		ratio of channel-integrated blackbody radi- ances (e.g. nighttime conditions)
<i>TISIL</i>		ratio of channel-integrated ground radiances (e.g. daytime conditions)

W	$[g/cm^2]$	atmospheric water vapor content
W^{ATM}		atmospheric water vapor content for a certain standard atmosphere ATM
ΔT_{bound}^{ATM}	$[K]$	certain temperature amount adding to the boundary temperature
$\Delta_j^{1.0} T_S$		surface temperature retrieval error (rms) for the subset j ("Regression" - Approach)
$\Delta_j^{1.0} T_{S_{max}}$		surface temperature retrieval error (maximum) ("Regression" - Approach)
$\Delta_j^{1.0} T_S^{**}$		surface temperature retrieval error (rms) for the subset j before applying emissivity corrections ("Regression" - Approach)
$\Delta_j^{1.0} T_{S_{max}}^{**}$		surface temperature retrieval error (maximum) before applying emissivity corrections ("Regression" - Approach)
$(\Delta Q)_{rms}$		root mean square (rms) retrieval error with $Q = \varepsilon_i, T_S$ ("TISIE" - Approach)
$(\Delta Q)_{max}$		maximum retrieval error with $Q = \varepsilon_i, T_S$ ("TISIE" - Approach)
ΔT_S^{final}		final maximum temperature retrieval error
ΔT_S^{sensor}		maximum temperature retrieval error due to sensor noise
ΔT_S^{AP}		maximum temperature retrieval error due to uncertainties of a priori information
ε_i		channel-integrated emissivity for channel i
ε_i^*		estimated channel-integrated emissivity for channel i
ε_λ		spectral emissivity according to wavelength λ
ε_ν		spectral emissivity according to wavenumber ν
$\Delta \varepsilon_i^{final}$		final maximum emissivity retrieval error in channel i
$\Delta \varepsilon_i^{sensor}$		maximum emissivity retrieval error due to sensor noise in channel i
$\Delta \varepsilon_i^{AP}$		maximum emissivity retrieval error due to uncertainties of a priori information in channel i
λ	$[\mu m]$	wavelength
ν	$[cm^{-1}]$	wavenumber
ϱ_{b_i}		channel-integrated bi-directional reflectivity
ϱ_{h_i}		channel-integrated directional hemispheric reflectivity

θ_s	$[\circ]$	sun zenith angle
θ_v		observer view angle
ϕ_s		solar azimuth angle
ϕ_v		observer azimuth angle
ϕ		azimuth angle relative to the solar azimuth angle
τ_i		channel-integrated atmospheric transmission or transmittance
$\tilde{\tau}_i$		channel-integrated effective atmospheric transmittance
τ_i^{sun}		channel-integrated atmospheric transmission in solar incidence direction

Abbreviations

<i>AC</i>	AP-index: Atmosphere-Cold
<i>AW</i>	AP-index: Atmosphere-Warm
<i>ATM</i>	Atmospheric standard model
<i>ATSR</i>	Along Track Scanning Radiometer
<i>AVHRR</i>	Advanced Very High Resolution Radiometer
<i>BIRD</i>	Bi-spectral InfraRed Detection
<i>DLR</i>	Deutsches Zentrum für Luft- und Raumfahrt
<i>ENSPS</i>	École Nationale Supérieure de Physique de Strasbourg
<i>ERS</i>	European Remote Sensing Satellite
<i>ESA</i>	European Space Agency
<i>FOV</i>	Field Of View
<i>FWHM</i>	Full Width at Half Maximum
<i>GRTR</i>	Groupe de Recherche en Télédétection et Radiométrie
<i>IFOV</i>	Instantaneous Field Of View
<i>LSIT</i>	Laboratoire des Sciences de l'Image, de l'Informatique et de la Télédétection
<i>LST</i>	Land Surface Temperature
<i>max</i>	MAXimum
<i>MU</i>	MODTRAN unit for aerosol amount = total vertical aerosol optical depth at 550nm since nadir view (Shettle, 2000)
<i>MIR</i>	Mid InfraRed spectral range
<i>MIRROR</i>	Michelson Interferometer with ROTating Retroreflector
<i>MISR</i>	Multi-angle Imaging Spectro-Radiometer (NASA/EOS)
<i>MLS</i>	Mid Latitude Summer atmosphere
<i>MLW</i>	Mid Latitude Winter atmosphere
<i>MODTRAN</i>	MODERate resolution lowTRAN code
<i>MRT</i>	MODTRAN Run Temperature
N_A	number of considered atmospheric models according to aerosols
N_C	number of considered atmospheric models according to cirrus clouds
N_ε	number of considered surface models according to emissivity
N_T	number of considered surface models according to temperature
N_{VA}	number of considered atmospheric models according to volcanic aerosols

N_W	number of considered atmospheric models according to water vapor content
NDVI	Normalized Difference Vegetation Index
NIR	Near InfraRed spectral range
AP	A Priori information
<i>rms</i>	Root Mean Square
RT	Radiative Transfer
RTM	Radiative Transfer Model
SST	Sea Surface Temperature
<i>SC</i>	AP-index: Surface-Cold
<i>SW</i>	AP-index: Surface-Warm
TISI, <i>TISI</i>	Temperature Independent Spectral Index for Radiances
TISIE, <i>TISIE</i>	Temperature Independent Spectral Index for Emissivity
TIR	Thermal InfraRed spectral range
<i>TOL</i>	TOLerance
TOA	Top Of Atmosphere
TROP	TROPical atmosphere
ULP	Université Louis Pasteur Strasbourg
US	US-standard atmosphere
VIS	VISible spectral range
WAOSS	Wide Angle Optoelectronic Stereo Scanner

Curriculum Vitae

Kerstin Lippert

born in Neustrelitz on September, 24 1971

email: kerstin.lippert@sap.com

Education and Professional Experience

since 01/2000	software developer at SAP SI in Dresden
12/1996 - 12/1999	PhD student at the Institute of Space Sensor Technology and Planetary Exploration at the German Aerospace Center (DLR - Deutsches Zentrum für Luft- und Raumfahrt) in Berlin-Adlershof: <i>Temperature Retrieval Using BIRD Data</i>
11/1998 - 03/1999	research scholar at Laboratoire des Sciences de l'Image, de l'Informatique et de la Télédétection (LSIT), Université Louis Pasteur Strasbourg (France): <i>Temperature Retrieval Using BIRD Data</i>
01/1996 - 11/1996	research scholar at Los Alamos National Laboratory, New Mexico, USA: <i>Top-of-Atmosphere Albedo Retrieval Using MISR (Multi-angle Imaging Spectro-Radiometer; NASA/EOS) Data</i>
09/1990 - 12/1995	study of meteorology at Humboldt-Universität Berlin, degree: "Diplom-Meteorologin" (M.S. in meteorology)
09/1978 - 08/1990	school in Neustrelitz, degree: "Abitur" (matriculations standard)

Professional Training

05/1995	summer school “Remote Sensing of Processes Governing Energy and Water Cycles in the Climate System”
03/1994 - 04/1994	synoptic training at the Meteorological Observatory in Potsdam (Germany)
02/1994 - 03/1994	research training at the department “Utilization of Sensor Data” at the Institute of Space Sensor Technology (DLR Berlin, Germany)
08/1993 - 09/1993	research training at the department “Meteorological Remote Sensing” at the Institute of Atmospheric Physics (DLR Oberpfaffenhofen, Germany)
09/1991	synoptic training at the Meteorological Observatory in Schleswig (Germany)

Conferences and Publications

Lippert, K., Li, Z.-L., Labed, J., Schönermark, M., & Stoll, M. (1999). Temperature Retrieval for Earth’s Surfaces using BIRD (Bi-spectral InfraRed Detection). IGARSS’99, Hamburg. IEEE IGARSS Proceedings 1999.

Lippert, K., & Zhukov, B. (1998). Bestimmung von Oberflächentemperaturen mittels BIRD-Daten. Deutsche Meteorologen-Tagung, Leipzig. Annalen der Meteorologie des Deutschen Wetterdienstes.

Lippert, K., Borel, C., & Gerstl, S. (1996). MISR (Multi-angle Imaging Spectro-Radiometer; NASA/EOS) TOA-Albedo Retrieval for Clear Sky Scenes. Internal Report (on request). Los Alamos National Laboratory, Los Alamos, New Mexico, USA.

Lippert, K. (1995). Bestimmung von Landoberflächentemperaturen aus Flugzeug- und Satellitendaten. Diplomarbeit, Humboldt-Universität zu Berlin, Institut für Physik - Meteorologie.

Acknowledgements

This thesis is the result of the successful cooperation of the group “Terrestrische Ökosysteme” at the Institute of Space Sensor Technology and Planetary Exploration at the German Aerospace Center (DLR - Deutsches Zentrum für Luft- und Raumfahrt) in Berlin-Adlershof, Germany, and of the group “Groupe de Recherche en Télédétection et Radiométrie” (GRTR) at Laboratoire des Sciences de l’Image, de l’Informatique et de la Télédétection/École Nationale Supérieure de Physique de Strasbourg (LSIIT/ENSPPS), Université Louis Pasteur Strasbourg (ULP), France. I would like to acknowledge:

- Dr. Maria v. Schönermark (DLR), Prof. Marc-Philippe Stoll (ULP), Prof. Hans Peter Röser (DLR), and Prof. Herbert Jahn (DLR) for the interesting subject of the thesis, the initiation of the cooperation, and the support of my five month stay at LSIIT/ENSPPS.
- Hans-Joachim Maschke (Technische Universität Berlin) and Prof. Marc-Philippe Stoll (ULP) for handling the administrative issues concerning the “cotutelle” at the two universities.
- all my coworkers at DLR who have always helped me on solving various problems I have encountered, especially Rosemarie Bischoff, Dr. Marco Radke, and Peter Uhlig.
- my coworkers at LSIIT/ENSPPS for giving me a warm welcome at Strasbourg and for many fruitful discussions, especially Dr. Jelila Labed-Nachbrand, Dr. Zhao-Liang Li, and Dr. François Petitcolin for being a great office-mate.
- everybody who contributed to the improvement of this work by the critical review of the manuscript.
- my fellow PhD-students at DLR Dr. Anko Börner, Dr. Rainer Wilhelm, and Lorenz Wiest for being wonderful friends and coworkers during my last three years in Berlin.